



**UCGE Reports  
Number 20240**

Department of Geomatics Engineering

**Automated Road Network Extraction from High  
Spatial Resolution Multi-Spectral Imagery**

(URL: <http://www.geomatics.ucalgary.ca/research/publications/GradTheses.html>)

by

**Qiaoping Zhang**

**April 2006**



UNIVERSITY OF CALGARY

Automated Road Network Extraction from High Spatial Resolution Multi-Spectral

Imagery

by

Qiaoping Zhang

A THESIS

SUBMITTED TO THE FACULTY OF GRADUATE STUDIES

IN PARTIAL FULFILMENT OF THE REQUIREMENTS FOR THE

DEGREE OF DOCTOR OF PHILOSOPHY

DEPARTMENT OF GEOMATICS ENGINEERING

CALGARY, ALBERTA

APRIL, 2006

© Qiaoping Zhang 2006

## Abstract

For the last three decades, the Geomatics Engineering and Computer Science communities have considered automated road network extraction from remotely-sensed imagery to be a challenging and important research topic. The main objective of this research is to investigate the theory and methodology of automated feature extraction for image-based road database creation, refinement or updating, and to develop a series of algorithms for road network extraction from high resolution multi-spectral imagery.

The proposed framework for road network extraction from multi-spectral imagery begins with an image segmentation using the  $k$ -means algorithm. This step mainly concerns the exploitation of the spectral information for feature extraction. The road cluster is automatically identified using a fuzzy classifier based on a set of predefined road surface membership functions. These membership functions are established based on the general spectral signature of road pavement materials and the corresponding normalized digital numbers on each multi-spectral band. Shape descriptors of the Angular Texture Signature are defined and used to reduce the misclassifications between roads and other spectrally similar objects (e.g., crop fields, parking lots, and buildings).

An iterative and localized Radon transform is developed for the extraction of road centerlines from the classified images. The purpose of the transform is to accurately and completely detect the road centerlines. It is able to find short, long, and even curvilinear lines. The input image is partitioned into a set of subset images called road component images. An iterative Radon transform is locally applied to each road component image. At each iteration, road centerline segments are detected based on an accurate estimation of the line parameters and line widths. Three localization approaches are implemented and compared using qualitative and quantitative methods. Finally, the road centerline segments are grouped into a road network. The extracted

road network is evaluated against a reference dataset using a line segment matching algorithm. The entire process is unsupervised and fully automated.

Based on extensive experimentation on a variety of remotely-sensed multi-spectral images, the proposed methodology achieves a moderate success in automating road network extraction from high spatial resolution multi-spectral imagery.

## **Acknowledgements**

I am deeply obliged to my supervisor, Dr. Isabelle Couloigner, for her constant support and guidance throughout the course of my research and thesis preparation. I would like to thank my co-supervisor, Dr. Ayman Habib, for his valuable suggestions, guidance and encouragement.

I would also like to acknowledge Dr. Wael Badawy, Dr. Bo Huang, Dr. John Yackel, and Dr. Costas Armenakis for their stimulating suggestions on the thesis topic.

My colleagues, Ms. Wenya Chiu, Ms. Valarmathy Meenakshisundaram, Mr. Santosh Phalke, and Mr. Matthew Reid supported me in my research work. I want to thank them for all their help, discussions, and valuable insights.

I am extremely grateful for my family. Special thanks go to my wife, Ms. Xiaolin Fang, for her patience, understanding, consideration and love, which enabled me to complete this thesis.

I acknowledge and appreciate the financial support I received from the NCE GEOIDE research program “Automating photogrammetric processing and data fusion of very high resolution satellite imagery with LIDAR, iFSAR and maps for fast, low-cost and precise 3D urban mapping” (AutoMap). This research is also partially supported by the Graduate Faculty Council Scholarship (2004, 2005), University Technologies International Fellowship (2004), Graduate Research Scholarship Award (2004, 2005), Canadian Natural Resources Limited Scholarship (2004), and J. B. Hyne Graduate Scholarship (2004). All of which are greatly appreciated.

# Table of Contents

Abstract .....	iii
Acknowledgements.....	v
Table of Contents .....	vi
List of Tables .....	ix
List of Figures .....	xi
List of Abbreviations .....	xviii
CHAPTER 1 INTRODUCTION .....	1
1.1    Background .....	1
1.2    Problem Statement .....	2
1.2.1    Road network modeling in remotely-sensed imagery .....	2
1.2.2    Image classification for road network extraction.....	4
1.2.3    Road centerline extraction from classified imagery .....	8
1.2.4    Road network formation .....	10
1.2.5    Quality assessment of road network extraction .....	10
1.3    Research Objectives.....	12
1.4    Research Contributions.....	12
1.4.1    Proposed road network model .....	12
1.4.2    Proposed methodology.....	14
1.5    Thesis Outline .....	15
CHAPTER 2 IMAGE CLASSIFICATION.....	17
2.1    Introduction.....	17
2.2    Image Segmentation of MSI.....	18
2.3    Road Cluster Identification .....	20
2.4    Summary .....	24
CHAPTER 3 ROAD CLASS REFINEMENT .....	25
3.1    Basic Angular Texture Signature.....	25
3.2    Shape Descriptors of Angular Texture Signature .....	28

3.3	Road Class Refinement Using the Angular Texture Signature .....	32
3.4	Summary .....	37
CHAPTER 4 ROAD CENTERLINE EXTRACTION .....		38
4.1	Introduction .....	38
4.2	The Basic Radon Transform .....	41
4.3	Line Parameter Estimation in the Radon Transform .....	43
4.3.1	Peak selection .....	43
4.3.2	Line width estimation in the Radon transform .....	51
4.3.3	Endpoint determination .....	54
4.3.4	Experiments .....	54
4.4	Iteration of the Radon Transform .....	62
4.5	Localization of the Radon Transform .....	64
4.5.1	The gliding-box approach .....	66
4.5.2	The connected component analysis approach .....	68
4.5.3	The spatial clustering approach .....	71
4.5.4	Comparison between different localization approaches .....	74
4.6	Summary .....	76
CHAPTER 5 ROAD NETWORK FORMATION .....		77
5.1	Endpoint Fusion .....	77
5.2	Gap Bridging .....	78
5.3	Creation of Road Intersections .....	79
5.4	Topological Structure Building .....	80
5.5	Road Network Cleaning .....	84
5.6	Summary .....	87
CHAPTER 6 QUALITY ASSESSMENT .....		89
6.1	Introduction .....	89
6.2	Quality Measures for Road Extraction .....	90
6.2.1	Completeness .....	92
6.2.2	Correctness .....	92
6.2.3	RMSE .....	92

6.3	Feature Matching for Quality Assessment.....	93
6.3.1	Matching primitives .....	93
6.3.2	Line segment distance measure .....	95
6.3.3	Matching Line Segments .....	96
6.3.4	Implementation .....	99
6.4	Assessing the Extracted Road Networks – AutoMap Test Data.....	100
6.4.1	Reference Data.....	101
6.4.2	Ikonos MS Images .....	101
6.4.3	Quickbird MS Images .....	104
6.5	Assessing the Extracted Road Networks – EuroSDR Test Data .....	107
6.5.1	Aerial Images .....	108
6.5.2	Leica ADS40 Images .....	113
6.5.3	Ikonos Images .....	117
6.6	Comparing the Two Evaluation Approaches .....	121
6.7	Summary .....	122
CHAPTER 7 CONCLUSIONS AND RESEARCH OUTLOOK .....		123
7.1	Conclusions.....	123
7.1.1	Image classification and road class refinement .....	123
7.1.2	Road centerline extraction from classified imagery .....	124
7.1.3	Road network formation .....	125
7.1.4	Quality assessment of road extraction .....	125
7.1.5	About computational load.....	126
7.1.6	About determination of parameters and thresholds .....	127
7.2	Outlook .....	127
REFERENCES .....		130



## List of Tables

Table 2.1 The mean and standard deviation of the original DN for the images in Figure 2.1 and Figure 2.2. Images are 11-bit coded.....	20
Table 2.2 The parameters used in the Gaussian membership functions for automatic road cluster identification.....	21
Table 2.3 Cluster means and the computed road membership values for the image in Figure 2.1 (indicated in red).....	22
Table 2.4 Cluster means and the computed road membership values for the image in Figure 2.2 (indicated in red).....	22
Table 3.1 The parameters used in the Gaussian membership functions for the road class refinement .....	32
Table 3.2 Evaluation of road class refinement.....	36
Table 4.1 Line width estimation (in pixels).....	53
Table 4.2 Line width estimation for the first synthetic image (in pixels).....	55
Table 4.3 Line width estimation for the second synthetic image (in pixels).....	56
Table 4.4 Positional accuracy assessment (in pixels).....	57
Table 4.5 Line width estimation for the first synthetic image with added noise (in pixels).....	59
Table 4.6 Line width estimation for the second synthetic image with added noise (in pixels).....	59
Table 4.7 Positional accuracy assessment with added noise (in pixels).....	60
Table 4.8 Comparison of different localization approaches .....	74
Table 4.9 Quality assessment of the extracted road networks using different localization approaches .....	75
Table 5.1 Road polyline attributes.....	81
Table 5.2 Road node attributes. ....	81
Table 5.3 Road vertex attributes. ....	82
Table 6.1 Quality assessment of the extracted road networks .....	102

Table 6.2 Quality assessment of the extracted road networks .....	105
Table 6.3 Quality assessment of the extracted road networks .....	109
Table 6.4 Quality assessment of the extracted road networks .....	114
Table 6.5 Quality assessment of the extracted road networks .....	117
Table 7.1 Average computational time (seconds).....	126
Table 7.2 Parameters and thresholds .....	128

## List of Figures

Figure 1.1 Proposed framework for road network extraction from MSI.....	15
Figure 2.1 A typical output of the <i>k</i> -means algorithm from Ikonos MS imagery: (a) original true color composite ortho-image; (b) segmented image with the identified road cluster shown in red.....	19
Figure 2.2 A typical output of the <i>k</i> -means algorithm from a Quickbird MS image: (a) original true color composite ortho-image; (b) segmented image with the identified road cluster shown in red.....	19
Figure 2.3 A plot of the Gaussian membership function.....	21
Figure 2.4 Road class identification from another Ikonos MS test image: (a) original true color composite ortho-image; (b) segmented image with the road cluster shown in red.....	23
Figure 2.5 Road class identification from another Quickbird MS test image: (a) original true color composite ortho-image; (b) segmented image with the identified road cluster shown in red.....	24
Figure 3.1 Texture is computed over (a) the set of rectangular regions about a pixel and (b) the graph of the Angular Texture Signature for a single pixel. The image used is a subset of an Ikonos MS-red image. For illustration purposes, the size of the rectangular regions is set to 5 by 20 pixels. (After [Gibson, 2003]).....	26
Figure 3.2 ATS –degree (a) and direction (b) for the road cluster presented in Figure 2.1. In (b) the direction indices are the same as in Figure 3.1 (a).....	27
Figure 3.3 Angular texture signature for (a) a pixel on a road; (b) a pixel in the corner of a parking lot; (c) a pixel within a T-road junction; and (d) a pixel in a parking lot.....	29
Figure 3.4 ATS-Mean (a) and ATS-Compactness (b) for the road cluster presented in Figure 2.1 .....	30
Figure 3.5 ATS-Eccentricity for the road cluster presented in Figure 2.1.....	31
Figure 3.6 ATS-direction for the road cluster presented in Figure 2.1. The direction indices are the same as in Figure 3.1(a) .....	32

Figure 3.7 Road membership (a) for the road cluster presented in Figure 2.1; (b) the output after thresholding (a) at 0.1. In (b) white: non-road pixels, red: road pixels, and blue: parking lots/buildings pixels. ....33

Figure 3.8 Road membership (a) for the road cluster presented in Figure 2.4; (b) the output after thresholding (a) at 0.1. In (b) white: non-road pixels, red: road pixels, and blue: parking lots/buildings pixels. ....34

Figure 3.9 Road membership (a) of the Quickbird MS ortho-image presented in Figure 2.2; (b) the output after thresholding (a) at 0.1. In (b) white: non-road pixels, red: road pixels, blue: parking lots/buildings pixels.....35

Figure 3.10 Road membership (a) of the Quickbird MS ortho-image presented in Figure 2.5; (b) the output after thresholding (a) at 0.4. In (b) white: non-road pixels, red: road pixels, blue: parking lots/buildings pixels.....35

Figure 4.1 A flowchart of the iterative and localized Radon transform for road network extraction from classified imagery.....41

Figure 4.2 Geometry of the Radon Transform (After [MathWorks, 2005]).....42

Figure 4.3 Accurate line parameter estimation in the Radon transform using the profile analysis technique: (a) the input image and the reconstructed line (dashed) based on the original radon peak; (b) the Radon transform; (c) a profile along the  $\rho$  axis shown as a white dashed line in (b) and an illustration of the estimation of the  $\rho$  value; (d) the reconstructed line using the refined radon peak. ....44

Figure 4.4 Examples of accurate line parameter estimation in the Radon transform: (a) and (c) show the reconstructed line (dashed) using the original radon peak; (b) and (d) show the reconstructed line (dashed) using the refined radon peak. ....46

Figure 4.5 Accurate line parameter estimation in the Radon transform using a mean filter: (a) the input image and the reconstructed centerline (dashed) based on the original radon peak; (b) the reconstructed line (dashed) using the refined line parameters based on the radon peak found by a mean filter; (c) the Radon transform; (d) zoomed in version of (c).  $R_0$  - the original radon peak;  $R_1$  - the radon peak found by the mean filter, the black dashed line shows the window used. ....48

Figure 4.6 Example of  $\theta$ -boundary problem of the Radon transform: (a) input image with the reconstructed line (dashed) based on the original radon peak; (b) the Radon transform; (c) the new reconstructed line (dashed) using the refined line parameters; (d) the expanded Radon transform with  $\theta$  as  $[-5^\circ, 185^\circ]$ . .....49

Figure 4.7 Peak selection problem in the Radon transform: (a) input image with a wide line, the red dotted line is the detected centerline using the single radon peak, the red solid line is the detected centerline using the refined radon peak; (b) the Radon transform of (a), where  $R_0$  is the single radon peak,  $R_1$  is the refined radon peak. The blue line depicts the radon peak region. ....50

Figure 4.8 Line width estimation in the Radon transform:  $\rho'_1$  and  $\rho'_2$  are two points located along the profile in the  $\rho$  direction at the refined radon peak ( $R_1$ ) shown in Figure 4.6 (b). They are determined by the half peak radon value. ....52

Figure 4.9 Calculation of line width .....53

Figure 4.10 Endpoints determination.....54

Figure 4.11 Centerline detection using the Radon transform from the first synthetic image: (a) the reconstructed lines (red) based on the original radon peaks; (b) the improved results.....55

Figure 4.12 Centerline detection of thick lines using the Radon transform from the second synthetic image: (a) the reconstructed lines (red) based on the original radon peaks; (b) the improved results. ....56

Figure 4.13 Centerline detection using the improved Radon transform for synthetic image one with added noise density of: (a) 0.02; (b) 0.05.....58

Figure 4.14 Centerline detection using the improved Radon transform for synthetic image two with added noise density of: (a) 0.02; (b) 0.05.....58

Figure 4.15 Detected road centerlines (red) overlaid on the road pixels (a) and the Ikonos MS true composite image (b). The estimated line widths for lines 1-3 are 2.4, 2.3 and 2.2 pixels respectively. ....61

Figure 4.16 Detected road centerlines (red) overlaid on the road pixels (a) and the Ikonos MS true composite image (b). The estimated line widths for lines 1-3 are 3.3, 3.9 and 2.0 pixels respectively. ....61

Figure 4.17 Centerline detection using the iterative Radon transform: (a) input image with five lines with different lengths, the red lines are the detected centerlines using the developed iterative Radon transform; (b) the Radon transform of (a); (c) the Radon transform of (a) with the longest line being removed (iteration 2); and (d) the Radon transform of (a) with the longest three lines being removed (iteration 4).....63

Figure 4.18 Local Radon transform vs. global Radon transform: (a) the input image with a single line and the detected centerline (red); (b) the Radon transform of (a); (c) the input image with six lines and the detected centerline (red) of the lower-left line; (d) the Radon transform of (c); (e) the peak region in (d) which corresponds to the lower-left line in (c).  $R_0$  is the peak element we are able to find while the  $R_1$  is the true location. ....65

Figure 4.19 Road centerline extraction from classified imagery using iterative and localized Radon transform based on gliding-box approach. (a) Ikonos test image; (b) Quickbird test image. Dashed blue lines indicate the gliding boxes and the red lines are the extracted road centerlines. ....67

Figure 4.20 Road centerline extraction from the classified Ikonos test image using an iterative and localized Radon transform based on a region growing approach. (a) road component images (differentiated by color) found by the region growing algorithm; (b) extracted road centerlines (red). ....69

Figure 4.21 Road centerline extraction from the classified Quickbird test image using an iterative and localized Radon transform based on a region growing approach. (a) road component images (differentiated by color) found by the region growing algorithm; (b) extracted road centerlines (red). ....70

Figure 4.22 Road centerline extraction from the classified Ikonos test image using an iterative and localized Radon transform based on the CLATIN spatial clustering approach. (a) output of the CLATIN algorithm: black pixels – road pixels, red points – final medoids, red lines – Voronoi tessellation of the final medoids; (b) extracted road centerlines (red).....72

Figure 4.23 Road centerline extraction from the classified Quickbird test image using an iterative and localized Radon transform based on the CLATIN spatial clustering approach. (a) output of the CLATIN algorithm: black pixels – road pixels, red points – final medoids, red lines – Voronoi tessellation of the final medoids; (b) extracted road centerlines (red). .....	73
Figure 5.1 Endpoint fusion .....	78
Figure 5.2 Gaps bridging .....	78
Figure 5.3 Road intersections creation.....	79
Figure 5.4 Road segments grouping: red points - fused small gaps, red lines - bridged big gaps, red crosses - created road nodes. ....	80
Figure 5.5 Road network formation based on the extracted road centerline segments from the Ikonos MS test image presented in Figure 2.1. ....	84
Figure 5.6 Road network formation based on the extracted road centerline segments from the Quickbird MS test image presented in Figure 2.2.....	85
Figure 5.7 Road network formation: (a) the extracted road centerline segments from the Ikonos MS test image presented in Figure 2.4; (b) the final road network.....	86
Figure 5.8 Road network formation: (a) the extracted road centerline segments from the Quickbird MS test image presented in Figure 2.5; (b) the final road network. ....	87
Figure 6.1 Evaluation of automated road extraction: (a) the RGB composite of the source image overlaid with the reference roads (red lines); (b) the extracted roads (red lines) .....	91
Figure 6.2 Matching line segments .....	96
Figure 6.3. Matching line segments (special case) .....	97
Figure 6.4 Evaluation results for the extracted road network in Figure 6.1 (b): Green – correct extraction, red – missed roads, blue – false extraction .....	100
Figure 6.5 Evaluation results for the image Ikonos MS 1: Green – correct extraction, red – missed roads, blue – false extraction .....	102
Figure 6.6 Evaluation results for the image Ikonos MS 2: Green – correct extraction, red – missed roads, blue – false extraction .....	103

Figure 6.7 Evaluation results for the image Ikonos MS 3: Green – correct extraction, red – missed roads, blue – false extraction .....	104
Figure 6.8 Evaluation results for the image Quickbird MS 1: Green – correct extraction, red – missed roads, blue – false extraction .....	105
Figure 6.9 Evaluation results for the image Quickbird MS 2: Green – correct extraction, red – missed roads, blue – false extraction .....	106
Figure 6.10 Evaluation results for the image aerial1: Green – correct extraction, red – missed roads, blue – false extraction ([Mayer <i>et al.</i> , 2005]). Image copyright: Swiss Federal Office of Topography, Bern, Switzerland .....	110
Figure 6.11 Evaluation results for the image aerial2: Green – correct extraction, red – missed roads, blue – false extraction ([Mayer <i>et al.</i> , 2005]). Image copyright: Swiss Federal Office of Topography, Bern, Switzerland .....	111
Figure 6.12 Evaluation results for the image aerial3: Green – correct extraction, red – missed roads, blue – false extraction ([Mayer <i>et al.</i> 2005]). Image copyright: Swiss Federal Office of Topography, Bern, Switzerland .....	112
Figure 6.13 Evaluation results for the image ADS40_1: Green – correct extraction, red – missed roads, blue – false extraction ([Mayer <i>et al.</i> , 2005]). Image copyright Leica Geosystems, Heerbrugg, Switzerland .....	115
Figure 6.14 Evaluation results for the image ADS40_2: Green – correct extraction, red – missed roads, blue – false extraction ([Mayer <i>et al.</i> , 2005]). Image copyright Leica Geosystems, Heerbrugg, Switzerland .....	116
Figure 6.15 Evaluation results for the image Ikonos1_sub1: Green – correct extraction, red – missed roads, blue – false extraction ([Mayer <i>et al.</i> , 2005]). Image copyright Bundeswehr Geoinformation Office (AGeoBw), Euskirchen, Germany .....	118
Figure 6.16 Evaluation results for the image Ikonos3_sub1: Green – correct extraction, red – missed roads, blue – false extraction ([Mayer <i>et al.</i> , 2005]). Image copyright Bundeswehr Geoinformation Office (AGeoBw), Euskirchen, Germany .....	119



Figure 6.17 Evaluation results for the image Ikonos3\_sub2: Green – correct extraction, red – missed roads, blue – false extraction ([Mayer et al. 2005]). Image copyright Bundeswehr Geoinformation Office (AGeoBw), Euskirchen, Germany .....121

## List of Abbreviations

<b>Abbreviation</b>	<b>Full Term</b>
ACE	Anti-parallel-edge Centerline Extraction
ASCII	American Standard Code for Information Interchange
ATS	Angular Texture Signature
AVIRIS	Airborne Visible/Infrared Imaging Spectrometer
CCA	Connected Component Analysis
CCD	Charge Coupled Device
CGI	Common Gateway Interface
CLATIN	Clustering Large Applications with Triangular Irregular Networks
DN	Digital Number
DSM/DTM	Digital Surface/Terrain Model
EuroSDR	European Spatial Data Research
GIS	Geographical Information System
GPS	Global Positioning System
HYDICE	HYper-spectral Digital Imagery Collection Experiment
ISODATA	Iterative Self-Organizing Data Analysis Technique
LIDAR	Light Detection And Ranging
MRA	Multi-Resolution Analysis
MSI	Multi-Spectral Imagery
NIR	Near InfraRed
NRNC	National Road Network, Canada
RMSE	Root Mean Square Error
SAR	Synthetic Aperture Radar
SORM	Self-Organized Road Map
SSRC	Self-Supervised Road Classification
SVM	Support Vector Machine

# CHAPTER 1

## INTRODUCTION

### 1.1 Background

Roads are a very important topographic object class and it is of paramount interest to minimize the updating cycles [Bentabet *et al.*, 2003]. For many Geographical Information System (GIS) applications (e.g. urban planning, vehicle navigation, traffic management, emergency handling, etc), it is also very important to keep the road network database current. For many years, photogrammetric and remote sensing imagery was considered as the primary data source for topographic mapping [Heipke *et al.*, 2004]. However, the traditional process of manually updating a road database is very tedious and time-consuming. Automated road network extraction from remotely-sensed imagery can be used to make the process of building and updating a road network database easier and more efficient.

According to Baltsavias (2004) and other literature [Klang, 1998; Fillin and Doytsher, 2000; Auclair-Fortier *et al.* 2001], image-based road network database updating may include the following four processes: (1) Extraction of new roads; (2) Elimination of roads which no longer exist; (3) Updating of roads which have changed; and (4) Improvement and refinement of existing non-changed roads, which can include an increased degree of detail, better geometric accuracy, increased attributes and possibly the third dimension [Heipke *et al.*, 2004].

The realization of the above four processes requires an efficient, robust and accurate extraction of a new version of the road network from remotely-sensed imagery. This is the main motivation of this research.

During the last three decades, substantial work has been completed for automated road extraction from remotely-sensed imagery in the photogrammetric and computer vision communities. Accordingly, many different strategies or algorithms are proposed in the existing literature [Auclair-Fortier *et al.*, 2000; Mena, 2003; Baltsavias, 2004;

Quackenbush, 2004]. However, little research has been conducted on road network extraction from multi-spectral imagery (MSI) [Doucette *et al*, 2001; 2004]. This situation is now changing due to the increasing availability of MSI with high spatial resolutions. MSI has a great advantage over panchromatic or other grey-level imagery in that it enhances the capability to discriminate road surface materials from most other types of landscape materials. For example, the multi-spectral data usually includes a NIR band that is a powerful discriminator of vegetation and man-made surfaces. This could be very helpful in a road identification step. With the emergence of advanced data fusion technologies, it is now even possible to extract road networks from Pan-sharpened MSI in urban areas (e.g., [Zhang and Wang, 2004]). However, many issues need to be further researched in extracting road networks from MSI, especially from high resolution MSI.

## **1.2 Problem Statement**

### **1.2.1 Road network modeling in remotely-sensed imagery**

The difficulties in automated road network extraction from remotely-sensed imagery lie in the fact that the image characteristics of road feature vary according to sensor type, spectral and spatial resolution, ground characteristics, etc. Even in the same image, different parts of the road network often appear differently. In urban residential areas, with high resolution remotely-sensed images, the situation is even worse [Wang and Zhang, 2000]. A high resolution image enables a more accurate localization of the road sides as well as its extraction as a surface element. However, it generates a higher complexity of the image and an increase in the number of artifacts (vehicles, trees along the road, occlusions) [Péteri *et al*, 2003]. Finally, in the real world, a road network is too complex to be well modeled mathematically.

As Xiong (2001) stated, “the studies of road image characteristics, their changes with respect to geographic background, image types, image resolutions, development of mathematical models to represent these characteristics, are critical in order to make substantive progress in this area.” The author further pointed out that a road

recognition algorithm can consider a limited set of characteristics and when these characteristics change beyond a certain limit, the algorithm may fail. Similar remarks have been made by Auclair-Fortier *et al* (2000): “in order to appropriately detect roads, understanding how a road’s physical characteristics influence its visual characteristics is primordial.” These visual characteristics are used to identify roads in a given image.

The general physical characteristics of a road in a remotely-sensed image have been presented by Bajcsy and Tavakoli (1976) and revisited by Auclair-Fortier *et al.* (2000). These characteristics include: (1) spectral properties (e.g. surface characteristics); (2) geometric properties (e.g. width, curvature); (3) topological properties (e.g. links, networking); and (4) contextual properties (e.g. the type of road).

A similar but more programmable road model was presented by Gruen and Li (1995, 1997). The properties in their generic road model included: (1) good contrast to adjacent areas; (2) homogeneity in grey values along a road; (3) smooth and without small wiggles; (4) continuous and narrow; (5) having an upper bound in the local curvature; and (6) without significant change in the width.

Limitations to the existing road models are:

- 1) Most of these properties are derived based on the assumption that the image is noise-free. In a real image, however, particularly in urban areas, roads are subject to many noisy artifacts (vehicles, trees along the road, occlusions) and are not necessarily satisfying the above conditions. A good road model must take noise into consideration.
- 2) Most of the existing road models only work at a single scale level. Multi-scale modeling is more suitable for a road network because of the multi-scale nature of the road network and the remotely sensed imagery.
- 3) Until recently, very few road models have been presented for multi-spectral imagery although high spatial resolution multi-spectral imagery is becoming more popular and available.

- 4) Road junctions play little or no role in the existing road models. This often leads to erroneous road network topology and to difficulties in road change detection and updating.

In this research, we are interested in developing a road network model which best describes the image characteristics of a road in high resolution multi-spectral imagery.

### **1.2.2 Image classification for road network extraction**

The task of road extraction addresses two issues: (1) identification and (2) delineation [Doucette *et al*, 2001]. A semi-automated algorithm relies on user-provided cues (e.g. seed points or initial directions) to identify the approximate location of a road. By contrast, fully automated methods attempt to integrate aspects of identification and delineation to achieve true operational autonomy. Most of the existing road extraction methods for MSI rely on an automated and reliable classification of road surfaces (e.g., [Doucette *et al*, 1999, 2001; Amini, *et al*, 2002, Song and Civco, 2004]). Unfortunately, the classification accuracy of roads is far from satisfactory whether a supervised classification method or an unsupervised method is used. The main difficulty lies in the high misclassification between roads and other spectrally similar objects, such as parking lots, buildings, crop fields, etc.

Quackenbush (2004) pointed out that a number of articles specifically take advantage of the multi-spectral nature of sensors such as Landsat TM, SPOT and Ikonos to extract road information. However, in most cases, even with hyper-spectral datasets, the spectral information alone was not sufficient to define roads and the classification was one component of a multistage process. Gardner *et al*. (2001) found that classification of roads using Airborne Visible/Infrared Imaging Spectrometer (AVIRIS) imagery was challenging due to the similarities of construction materials in roads and roofs. They found that following the classification with a spatial pattern recognition technique using a Q-tree filter improved the final result.

The primary concern in urban areas is the misclassification between roads and parking lots. Road and parking lot surfaces often use the same construction materials and thus

have similar spectral signatures, which make it very difficult to automatically separate them in a remotely-sensed image. Introducing other information, such as height data from LIght Detection And Ranging (LIDAR) and clues from detected vehicles, does not measurably improve the situation since roads and parking lots are usually at the same level and both will usually be occupied by vehicles. Research on the classification of roads and parking lots is quite recent, partly due to the fact that road network extraction in urban areas only becomes feasible with the availability of high resolution remotely-sensed imagery.

In [Hu *et al.*, 2004a], the vehicle clue is used to verify a parking area in combination with a morphologic operation, which is applied to the classified aerial image to detect big open areas. The vehicles are extracted by a pixel based classification method. It is assumed that a region with a nearly square shape and large area has a high possibility of being a parking lot. The output from this step is used to improve the detected road segments using a Hough transform. Although the test results from 0.5m resolution color ortho-imagery with LIDAR data are quite good, there is no information available on using the morphologic operation to identify the large open areas. On the other hand, their research confirms our belief that although introducing LIDAR data is useful in building extraction, it is not very useful in road network extraction because it does not improve our ability to separate parking lots from roads.

Based on image classification results from pan-sharpened imagery, Zhang and Wang (2004) apply a segment filtering algorithm to deal with large parking lots and buildings which are misclassified as road networks. Basically, a directional texture detector is developed to distinguish different types of objects according to their textures in different directions. The directional texture detector measures the pixel grey value variance along the central lines in each of four directions (N, S, E and W) of an operation window. If all of the variances in the four directions are smaller than a certain value, it can be concluded that the object within this window is homogeneous and can be considered as a non-road object. The object can then be removed. The work demonstrates that it is possible to extract urban objects from pan-sharpened

imagery. However, the separation of parking lots and buildings from road networks is not satisfactory. Many artifacts are introduced by the directional texture detector. Similarly in [Wang *et al.*, 2005], directional texture information was used to eliminate non-road objects on classified imagery in combination with edge information from the panchromatic image and shape/size information of the connected components. .

The directional texture measure is also known as the Angular Texture Signature (ATS). It was used by Haverkamp (2002) and Gibson (2003) for finding road networks in Ikonos Panchromatic imagery. The texture measure that they used as a road detector had two components: the degree of the pixel (i.e. the number of the strong local minima in the angular texture signature) and the direction of the minimum.

Song and Civco (2004) used two shape measures, namely smoothness and compactness, to further reduce the misclassification between roads and other spectrally similar objects from a support vector machine (SVM) classifier. The two shape measures were derived by the commercial software eCognition©. Experiments on Ikonos MS imagery showed that the SVM classifier has a slightly better performance than the traditional maximum likelihood classifier in terms of overall classification accuracy. By combining the spectral information and shape measures they were able to remove most of the false-road objects in the road group.

Doucette *et al.* (1999) performed a principal component analysis on HYper-spectral Digital Imagery Collection Experiment (HYDICE) imagery and then used a maximum likelihood classification to generate a classified layer. This classified layer was combined with coarse GIS data in a neural network in order to extract linear features. The GIS data provided approximate location information for the extraction which speeded up convergence while minimizing user input. A Self-Organized Road Map (SORM) was developed by Doucette *et al.* (2001) for extracting road networks from classified imagery. Doucette *et al.* (2004) present a novel methodology for fully automated road centerline extraction that exploits the spectral content from high resolution multi-spectral images. Preliminary detection of candidate road centerline components is performed with Anti-parallel-edge Centerline Extraction (ACE). This is



followed by constructing road vector topology using a fuzzy grouping model that links nodes from a self-organized map of the ACE components. Following topology construction, a Self-Supervised Road Classification (SSRC) feedback loop is implemented to automate the process of training sample selection and refinement for a road class, as well as deriving practical spectral definitions for non-road classes. SSRC demonstrates a potential to provide dramatic improvement in road extraction results by exploiting the spectral content. Road centerline extraction results are presented for three 1m color infrared suburban scenes which show significant improvement following SSRC.

The Ikonos MS image is first classified into road and non-road classes in [Gao and Wu, 2004]. The road class is refined by removing noisy pixels, such as the building pixels, using a spatial filter based on the assumption that all of the small size components are not actual road pixels. The road segments are then joined and thinned to form a road network.

In [Tarku *et al.*, 2004], the coarse road class is obtained by thresholding the original panchromatic image. Refinement is achieved by removing the false road pixels based on a connected component analysis. Small components, dense components, and irregular components are less likely to be road-based components. They are identified and removed from the road class.

In their knowledge-based 3D road extraction [Zhang, 2004], the ISODATA algorithm was used to classify the input color images into five classes: road regions, vegetation, shadow areas, dark roofs and red roofs. The three bands used for the image classification were 1) the first component of the principal component transformed image; 2) a greenness band calculated with R and G bands in RGB space as  $(G-R)/(G+R)$ ; and 3) S band of HSI color space. The 3D roads were detected by combining the multi-source clues: the information derived from the classified road regions, the 3D straight edges detected from the input stereo images, the Digital Surface Models (DSM) and Digital Terrain Models (DTM), and the knowledge base

built from a GIS database. The research was mainly focusing on extracting roads in rural areas.

In summary, the image classification for road network extraction is still problematic. In urban residential areas, with high resolution remotely-sensed images, the situation is worse [Wang and Zhang, 2000]. Due to the inability of the discriminatory of spectral information, there is a trend to incorporate the spatial information in image classification or to refine the spectral road class by integrating the spatial information. In this research, we propose a new approach to effectively identify the parking lots/buildings and other spectrally similar objects from the road cluster resulting from a spectral clustering. This approach is based on newly developed shape descriptors of the Angular Texture Signature in combination with a fuzzy classifier.

### **1.2.3 Road centerline extraction from classified imagery**

There are a number of road network extraction algorithms that can be applied to high resolution classified imagery. Doucette *et al.* (1999; 2001) presented a self-organizing road map (SORM) approach to road centerline delineation from classified high-resolution MSI. The SORM is essentially a spatial clustering technique adapted to identify and link elongated regions. This technique is independent from a conventional edge definition and can meaningfully exploit multi-spectral imagery. However, the positional accuracy of the extracted lines is low because they are created by linking the cluster centers, which are sensitive to noisy pixels (e.g. misclassified road pixels). Line-fitting techniques can also be applied but they are only suitable for finding a single line in an image. This is not the case in road network extraction. Mathematical morphology operations are also used to find the line skeletons in a binary image (e.g., Karathanassi *et al.*, 1999; Amini *et al.*, 2002). However, these methods have issues with spikes in the resulting skeletons, which are usually determined at a pixel level. The Hough transformation was used by Hu *et al.* (2004a) in their integrated processing of high resolution imagery and LIDAR data for the automatic extraction of a grid structured urban road network. To reduce the influence of multiple peaks in the transform space, the Hough transform was applied iteratively. For each step of the

transform, only one maximum response in the Hough space was detected. The extracted stripe pixels were then removed from the binary image.

The Radon transform has a number of advantages for linear feature detection including its ability to detect line width and its robustness to noise [Murphy, 1986]. It has been widely used in remote sensing for linear feature (e.g., ship wakes) detection from Synthetic Aperture Radar (SAR) images [Copeland *et al.*, 1995; Du and Yeo, 2004; Zilman *et al.*, 2004] and from LIDAR data [Manandhar and Shibasaki, 2002; Clode *et al.*, 2004]. However, the quality of the Radon transform-based linear feature detector needs to be improved for road network extraction from remotely sensed imagery. First, it fails to provide an indication of the line length or the end-point positions, and cannot be relied upon to detect linear features of short extent [Murphy, 1986]. Second, linear features that span the entire image but display some curvature may not produce suitable peaks or valleys in the transform domain [Copeland *et al.*, 1995]. Third, the localization of the peaks or valleys is very difficult in some cases, which complicates the accurate estimation of the line parameters. Finally, it does not accurately find the centerline of thick lines; their diagonals are found instead [Clode *et al.*, 2004].

The quality of the extracted road centerline from classified imagery usually determines the positional accuracy of the extracted road network. Therefore, it is important to develop a method that can accurately locate road centerlines based on the classified road pixels. Our literature review and preliminary experiments have shown that the Radon transform-based linear feature detector is a good choice because of its robustness to noisy pixels (i.e. misclassified pixels), its positional accuracy, and its capability to estimate line width. In this research, an advanced technique is proposed to accurately estimate the line parameters including the line width in the Radon domain. An iterative and localized Radon transform is then developed to extract road centerlines from the classified remotely sensed imagery.

### **1.2.4 Road network formation**

Road network formation enables the link between individual road segments to form meaningful road lines and it generates the topological structure of the network so that the data is ready for use within a GIS. It usually includes a set of processes such as bridging gaps between road segments, creating nodes for road intersections, and removing overshooting and undershooting.

Perceptual grouping (organization) is defined as an ability to explore a structuralized feature organization from sensory data. It allows us to form object hypotheses with minimal domain knowledge [Hu and Tao, 2002]. The Gestalt psychologists have found a set of important properties in perceptual organization: proximity, continuity, similarity, closure, and symmetry. These properties can be used as primary constraints for linking fragmented road segments. Perceptual grouping has been widely used in the computer vision community [Boyer and Sarkar, 1999]. It has four general operating levels: signal, primitive, structure and assembly. In [Crevier, 1999], a probabilistic method for extracting chains of collinear segments is presented. A similar approach is adopted in [Hu and Tao, 2002].

There are two main concerns in road network formation. The first is how to bridge the gaps caused by artifacts such as trees, shadows or occlusions from buildings. This affects the completeness of the extracted road network and the topological correctness of the network. The second is how to remove the false extraction during this step because, based on the connection analysis, many falsely extracted road centerlines can be identified and thus removed. This can improve the correctness of the extracted road network. The basic procedures of road network formation are studied with an emphasis on grouping the road centerline segments.

### **1.2.5 Quality assessment of road network extraction**

Quality assessment is an important and necessary step for automated road extraction from imagery. However, relatively little work has been carried out in this area [Hinz *et al.*, 2002; Wiedemann, 2003].

Couloigner and Ranchin (1998) proposed some criteria to quantitatively assess the extracted road network based on surface calculations, comparison of the direction and length differences, node distance between the extracted street lines and the manually extracted reference lines. Péteri and Ranchin (2002) presented an approach to guide the determination of a reference based on statistical measures from several image photo-interpretations. They concluded that it was important not to rely on a single image photo-interpretation for establishing the reference. In Wiedemann (2003), the evaluation of the extracted road data was carried out by comparing the automatically extracted road centerlines with reference data. The evaluation was processed in two steps: (1) matching the extracted road primitives to the reference network using a modified buffering method and (2) calculating quality measures such as Completeness, Correctness, Redundancy, or Root mean square difference. For road intersections, Wiedemann (2002, 2003) proposed the use of a matching-based measure to evaluate the extracted results. Péteri *et al.* (2004) provided an approach to define a reference based on a tolerance zone. They also used a set of quantitative criteria for both the planimetric accuracy evaluation and the spatial characterization of the extracted road network.

The main problem with the quality assessment of an extracted road network is the lack of positional accuracy measures for linear features. Hausdorff distance [Hangouet, 1995] and Buffering-based distance [Goodchild and Hunter, 1997; Walter and Fritsch, 1999] measures are computationally intensive.  $L_2$ -distance [Saalfeld, 1988; Saalfeld, 1993] and Linear Mapping-based measures [Fillin and Doysther, 1999; Fillin and Doysther, 2000] rely on the matching of vertices. When the matching fails, the calculated distance is distorted.

Another problem is that given two versions of a road network - the extracted one versus the reference one - how can we automatically find the conjugate road lines? This is usually done manually, which is very time consuming. Based on some similarity measures, including distance measures, we can automate the matching to some degree and save time in assessing the quality of the extracted road network.

In this research, a line segment matching strategy is designed to decide the matched portion of two conjugate line segments. Quality evaluation is then carried out based on the distance measure and the matching results.

### **1.3 Research Objectives**

The main objective of this research is to investigate the theory and methodology of automated feature extraction for image-based road database generation, refinement and updating. More specifically, the objective is to develop a series of algorithms for road network extraction from high resolution multi-spectral imagery.

### **1.4 Research Contributions**

#### **1.4.1 Proposed road network model**

A road network model is essential for a successful road network extraction. However, a generic road network model does not exist due to the complexity of the real road network and the variety of imaging sensors and conditions. We summarize the image characteristics of a road in high resolution multi-spectral imagery in the following sections. These characteristics also serve as the basic assumptions of this research.

##### **1.4.1.1 Spectral properties**

Depending on the pavement material (e.g. asphalt) used and their ages, in multi-spectral imagery (assuming we have red, green, blue, and NIR bands and under normal imaging conditions, i.e., no flooded or no snow-covered roads), roads usually have relatively high reflectivity in red, green and blue bands, while relatively lower reflectivity in NIR band. Due to the variety of sensing conditions and road conditions, the reflectivity values (or the digital numbers) cannot be compared directly. In this research, we use normalized digital numbers to segment the input image and then identify the road cluster(s).

In a single band, roads usually have good contrast with their adjacent areas and are homogenous in terms of digital numbers along the road. However, this is not true when:

- 1) the road surface has been partially repaired and thus it might have different pavement materials resulting in different reflectivity values within a small range;
- 2) the road surface is in shadow of trees or buildings;
- 3) the road surface is occluded by trees or buildings;
- 4) the road surface is occupied by vehicles;
- 5) the road surface has traffic markings on it; and
- 6) the road surface is covered by snow, etc.

Due to these highly complex phenomena, it is almost impossible to model all of the situations and incorporate them in a single road network extraction process. In this research, we assume that all of the situations will result in a misclassification in the image classification step and thus will be treated in the road centerline extraction and road network formation steps by using less noise-sensitive approaches.

#### **1.4.1.2 Spatial properties**

Spatially, a road extends continuously and narrowly along the road direction. In low-resolution images ( $> 4\text{m}$ ), roads may appear as lines. In high-resolution images, roads appear as elongated regions with parallel borders [Auclair-Fortier *et al.*, 2000]. This property can be used to separate roads from many other spectrally similar objects, such as parking lots, buildings, and crop fields as these non-road objects usually occupy a large and wide area.

#### **1.4.1.3 Geometric properties**

A road usually extends smoothly without small wiggles [Gruen and Li, 1997]. It usually has an upper bound in local curvature, which follows from the smooth traffic flow requirement [Gruen and Li, 1997]. It does not significantly change in width [Bajcsy and Tavakoli, 1976; Gruen and Li, 1997]. These geometric properties justify extracting road primitives locally and then linking them to form a road network.

#### **1.4.1.4 Topological properties**

Roads are built to link certain places together and neighboring roads are connected to form networks [Bajcsy and Tavakoli, 1976]. This property is usually used in the road network formation step, particularly when bridging the gaps.

#### **1.4.1.5 Contextual properties**

The type of road is one of the contextual properties which can be used in road network extraction. In the real world, the roads have different classes, such as highway, driveway, or streets. Knowing the types of roads under consideration can be helpful when determining the parameters to use, e.g. the width of a search window. This information can also be used to verify the extracted roads properties, e.g. the road width.

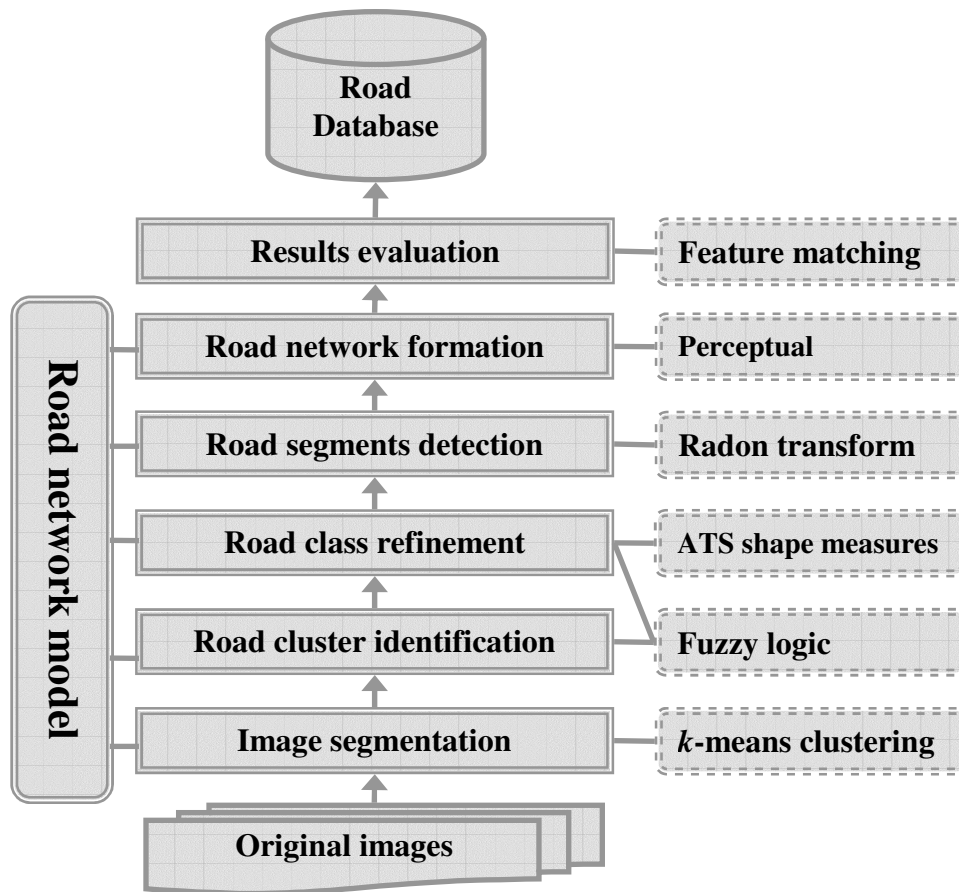
### **1.4.2 Proposed methodology**

In this research, a framework for road network extraction from multi-spectral imagery is proposed, which starts with an image segmentation using the *k*-means algorithm (Figure 1.1). This step mainly concerns the exploitation of the spectral information for feature extraction. The road cluster is then automatically identified using a fuzzy classifier based on a set of predefined membership functions for road surface recognition. These membership functions are established based on the general spectral signature of the road pavement materials and the corresponding normalized digital numbers on each multi-spectral band. A number of shape descriptors are defined for a refined Angular Texture Signature. These measures are used to reduce the misclassifications between the roads and parking lots/buildings.

An iterative and localized Radon transform is developed for the road centerline extraction from the classified images. It can find the road centerlines accurately and completely, and is able to find short, long, and even curvilinear lines. The input space is partitioned into a set of subset images called road component images. An iterative Radon transform is applied locally to each road component image. At each iteration, road centerline segments are detected based on an accurate estimation of the line parameters including line widths. The road centerline segments are then grouped into a



road network, which is assessed against a reference dataset. The entire process is unsupervised and fully automated.



**Figure 1.1** Proposed framework for road network extraction from MSI

## 1.5 Thesis Outline

Chapter 2 briefly discusses the issues on image segmentation of MSI. The traditional *k*-means clustering is used in this research because of its simplicity and efficiency. A fuzzy logic classifier is designed to automatically identify the road clusters.

Chapter 3 provides a novel approach to refine the road class resulting from the image segmentation step. First we introduce the basic angular texture signature and then define a set of shape descriptors for the refined angular texture signature. The descriptors are used to separate the road features from other spectrally similar ground features, such as parking lots, buildings, or certain crop fields.

Chapter 4 discusses the problem of road centerline extraction from the classified imagery. An iterative and localized Radon transform is proposed and used to accurately extract the road centerlines.

Chapter 5 deals with the road network formation issues. Perceptual grouping is used to link the road segments into a meaningful road network. This network is ready to be used in a GIS.

Chapter 6 addresses the quality assessment, which is an important and necessary step for an automated road network extraction system. A new line segment matching algorithm is developed for the purpose of evaluating the road extraction results.

Chapter 7 gives some concluding remarks followed by a brief look at future research of automated road network extraction from high resolution remotely sensed imagery.

## CHAPTER 2

# IMAGE CLASSIFICATION

### 2.1 Introduction

As was mentioned in the previous chapter, a multi-spectral image (MSI) provides more spectral information than a single band image. The goal is to exploit the spectral information in order to improve the road network extraction process. In general, we have two options: (1) to extract the roads from each band and then fuse them to form a single version of the road network; or (2) to classify the input multi-spectral image and then extract the roads from the classified imagery. The first option involves intermediate-level (also called feature-level) or even high-level (also called decision-level) data fusion [Pohl and Genderen, 1998]. It is more difficult to implement because the roads extracted from different bands are subject to different levels of inaccuracy and incompleteness. For that reason, the second option is applied in this research. One of the advantages of the second option is that new or more advanced image classification approaches can be easily encompassed in the road network extraction framework without significantly altering the process flowchart.

Image classification plays an important role in the automated road network extraction from remotely sensed imagery, especially from high resolution MSI. The choice of image classification methods is also important and will affect the entire process. A supervised classification method often achieves better overall results than an unsupervised classification method. However, a supervised classification requires setting up a training set, which usually relies on a heavy human intervention. A spatially-integrated (e.g. texture-based method) [Ruiz, *et al.*, 2004], object-based method [Benz, *et al.*, 2004]) has been shown to be superior to a purely spectral-based method. In this research, we use an unsupervised approach for coarse classification and then integrate the spatial information in the refinement step.

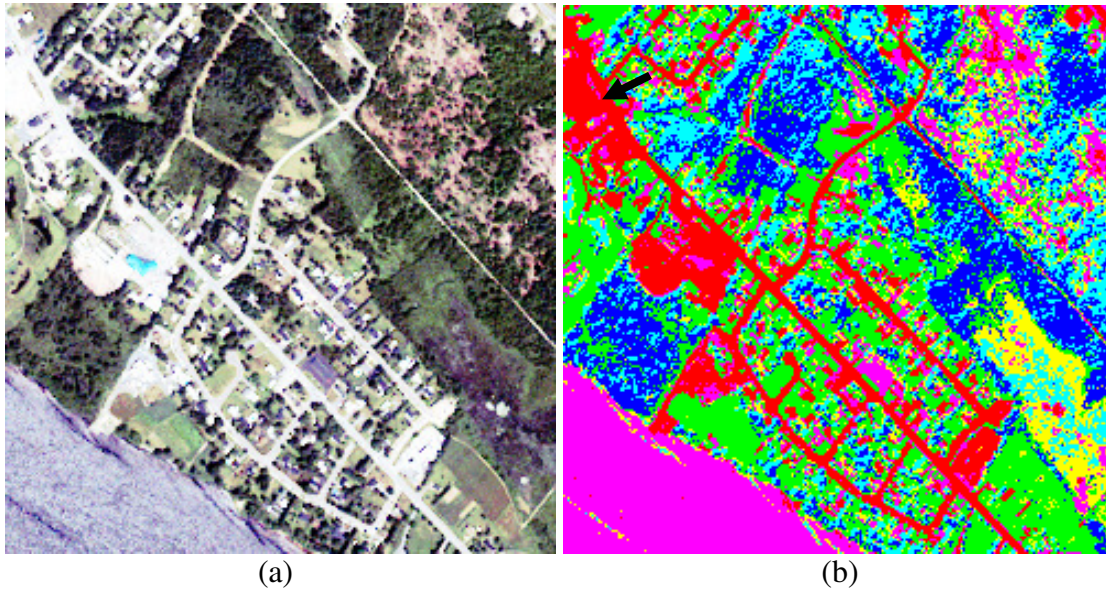
In this chapter, the simple  $k$ -means clustering algorithm is chosen for the image segmentation of MSI for the purpose of automated road network extraction. A fuzzy logic classifier is designed to automatically identify the road cluster from the clustering results. Some typical outputs from our experiments will be given and discussed.

## 2.2 Image Segmentation of MSI

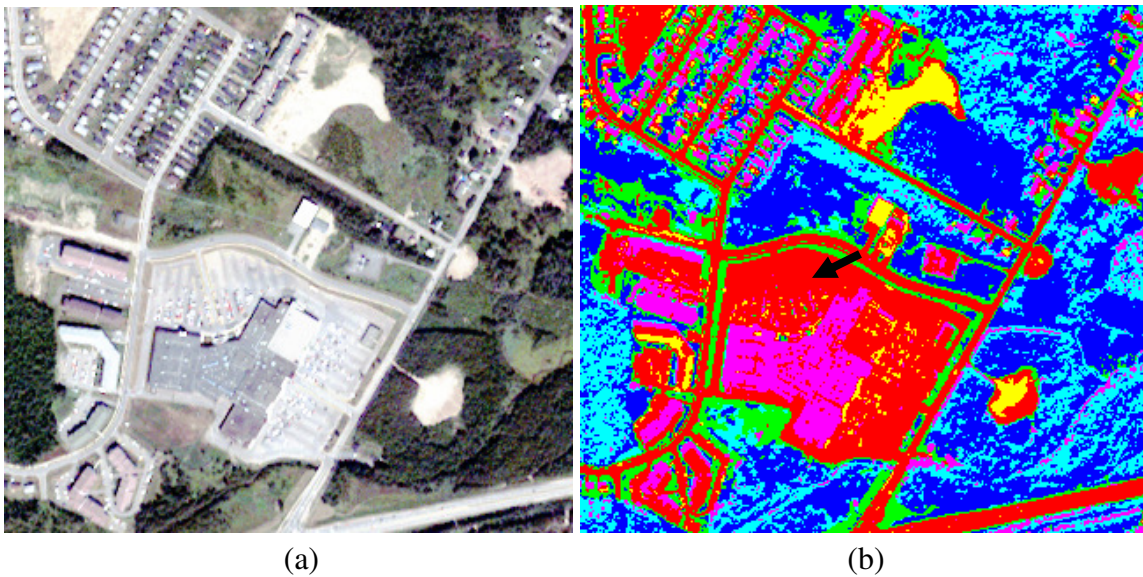
Image segmentation is the division of an image into meaningful structures, called regions or segments [Heijden, 1994]. The partitioning is meaningful, if and only if, a correspondence is known to exist between segments and portions of the object being “imaged”. There are many methods for image segmentation, ranging from edge-based approaches to region-based algorithms [Gonzalez and Woods, 2002]. However, most of the algorithms mainly apply to grey level imagery. For MSI, spectral clustering algorithms are often used. These include  $k$ -means, ISODATA, mean shift [Comaniciu and Meer, 2002] classifiers, etc. In our research, the  $k$ -means algorithm is applied because of its simplicity and efficiency. All bands of an input image are used in the spectral clustering. Although five to seven spectral clusters work well for most of the test images, six clusters have been selected for all the cases in this research.

Figure 2.1 depicts a typical output of the  $k$ -means algorithm from Ikonos MS imagery. We can see clearly that the algorithm is able to separate the road surfaces successfully from the other landscape types. However, there is a high misclassification between the roads and other spectrally similar objects (e.g. the upper-left corner of the image indicated by the black arrow).

Figure 2.2 depicts a typical output of the  $k$ -means algorithm from QuickBird MS imagery. As with the Ikonos MS imagery, we can see that the algorithm is able to separate the road surfaces successfully from the other landscape types. However, there is also a high misclassification between the roads and other spectrally similar objects (e.g. the parking lots in the centre portion of the image indicated by the black arrow).



**Figure 2.1** A typical output of the  $k$ -means algorithm from Ikonos MS imagery: (a) original true color composite ortho-image; (b) segmented image with the identified road cluster shown in red



**Figure 2.2** A typical output of the  $k$ -means algorithm from a Quickbird MS image: (a) original true color composite ortho-image; (b) segmented image with the identified road cluster shown in red.

## 2.3 Road Cluster Identification

To automate the process, we need to find a way to automatically identify the road cluster in the segmented image. Due to the discriminating capability of the multi-spectral imagery, the road cluster does have its own signature in the final means of each cluster.

Generally speaking, the road surface has relatively higher reflectance in the blue, green, and red bands, while it has a relatively lower reflectance in the near infrared band assuming normal imaging conditions. The problem is how to mathematically model these spectral signatures. Several methods have been tested in this research. It was found that the direct digital number (DN) of the final means is not reliable because its value will vary with different scenes. In this research, the mean-standard deviation normalization (Eq.2.1) is applied for each band and the normalized DNs are used in the spectral clustering.

$$DN_{1k} = \frac{DN_{0k} - mean_{0k}}{\sigma_{0k}} \quad (2.1)$$

where  $DN_{0k}$  and  $DN_{1k}$  are the original and normalized digital number respectively,  $mean_{0k}$  and  $\sigma_{0k}$  are the mean and standard deviation of the band  $k$ . The computed means and standard deviations for the images in Figure 2.1 and Figure 2.2 are shown in Table 2.1.

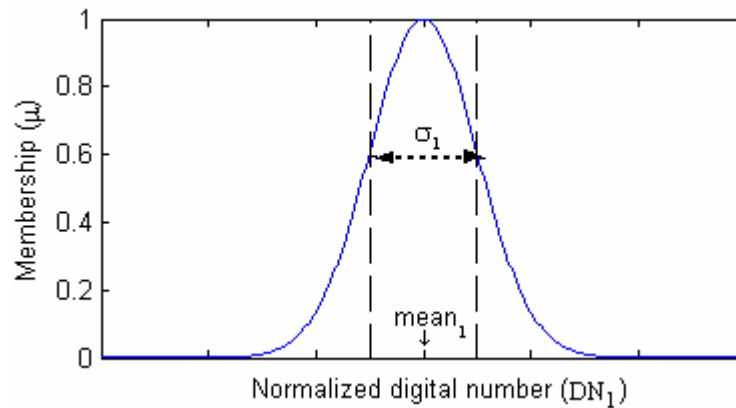
**Table 2.1** The mean and standard deviation of the original DN for the whole images in Figure 2.1 and Figure 2.2. Images are 11-bit coded.

Image	Band	Blue	Green	Red	NIR
Figure 2.1 (Ikonos)	Mean	590.97	766.13	694.00	798.32
	Std	317.86	327.59	342.14	529.32
Figure 2.2 (Quickbird)	Mean	175.19	236.46	142.70	462.58
	Std	49.42	88.61	83.96	166.09

The final means resulting from the clustering are used to automatically find the road clusters based on a fuzzy logic classifier. The Gaussian membership functions [Ross, 1995] are used for all four bands as these functions can easily express the concepts “relatively higher” or “relatively lower” (Eq.2.2 and Figure 2.3).

$$\mu(DN_{1k}) = \exp\left(-\frac{(DN_{1k} - mean_{1k})^2}{2\sigma_{1k}^2}\right) \quad (2.2)$$

where  $DN_{1k}$  is the normalized digital number of band  $k$  of the final road clusters (Table 2.3 and Table 2.4),  $mean_{1k}$  and  $\sigma_{1k}$  are the mean and standard deviation of the Gaussian membership functions defined for the road clusters (Table 2.2). The values in Table 2.2 are empirically selected. They might need to be changed for different imaging systems or different imaging conditions.






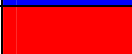


**Figure 2.3** A plot of the Gaussian membership function.

**Table 2.2** The parameters used in the Gaussian membership functions for automatic road cluster identification.







<b>Band</b>	<b>Blue</b>	<b>Green</b>	<b>Red</b>	<b>NIR</b>
<b>Mean</b>	1.50	1.50	1.50	-0.50
<b>Std</b>	0.25	0.25	0.25	0.25

The cluster which has the highest combined road membership is labeled as the road cluster. The combined road membership is determined by multiplying the road memberships from each band. For our two previous test images, the computed road membership values are shown in Table 2.3 and Table 2.4 (indicated in red in the table legends).

**Table 2.3 Cluster means and the computed road membership values for the image in Figure 2.1 (indicated in red).**

Cluster	Legend	Blue	Green	Red	NIR	Road Membership
1		-0.335	-0.285	-0.225	-0.503	<i>0.2500</i>
2		0.036	0.491	0.356	1.112	<i>0.0001</i>
3		-0.791	-0.671	-0.792	1.024	<i>0.0000</i>
4		1.885	1.761	1.857	-0.499	<i>0.5617</i>
5		-1.063	-1.337	-1.216	-0.498	<i>0.2500</i>
6		0.833	0.581	0.639	-1.089	<i>0.0236</i>

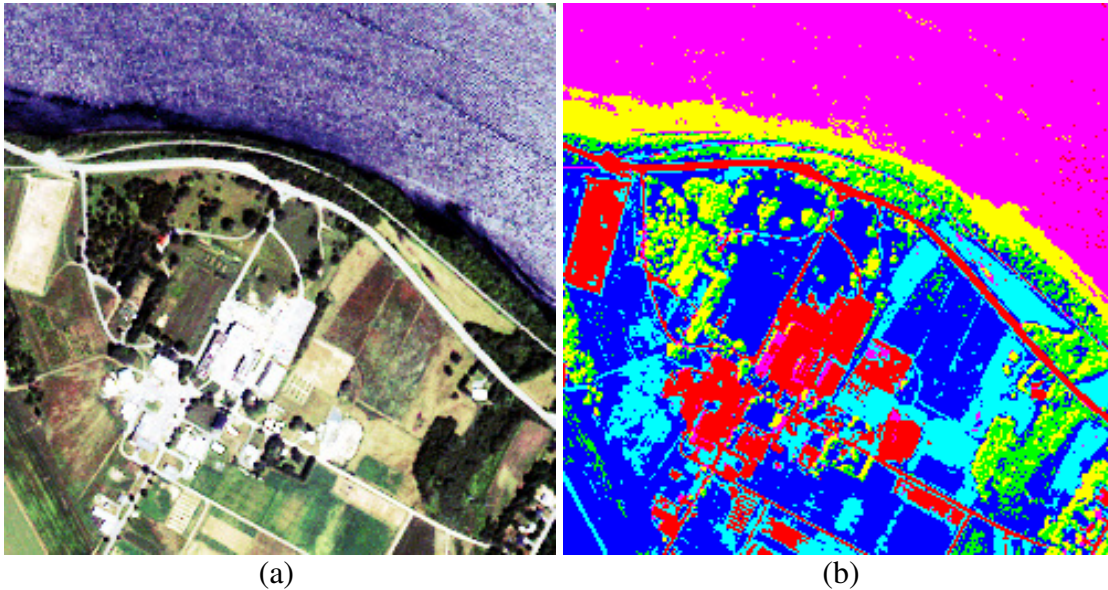
**Table 2.4 Cluster means and the computed road membership values for the image in Figure 2.2 (indicated in red).**

Cluster	Legend	Blue	Green	Red	NIR	Road Membership
1		0.185	0.293	0.375	0.162	<i>0.0075</i>
2		-0.704	-0.760	-0.740	-0.180	<i>0.1101</i>
3		-0.507	-0.411	-0.479	1.080	<i>0.0000</i>
4		3.234	3.379	3.317	0.303	<i>0.0014</i>
5		-0.168	-0.387	-0.324	-1.642	<i>0.0000</i>
6		1.434	1.391	1.400	-0.795	<i>0.8242</i>

A number of other Ikonos MS ortho-images with a 4m spatial resolution have also been tested. The identified road clusters are identical to those determined through

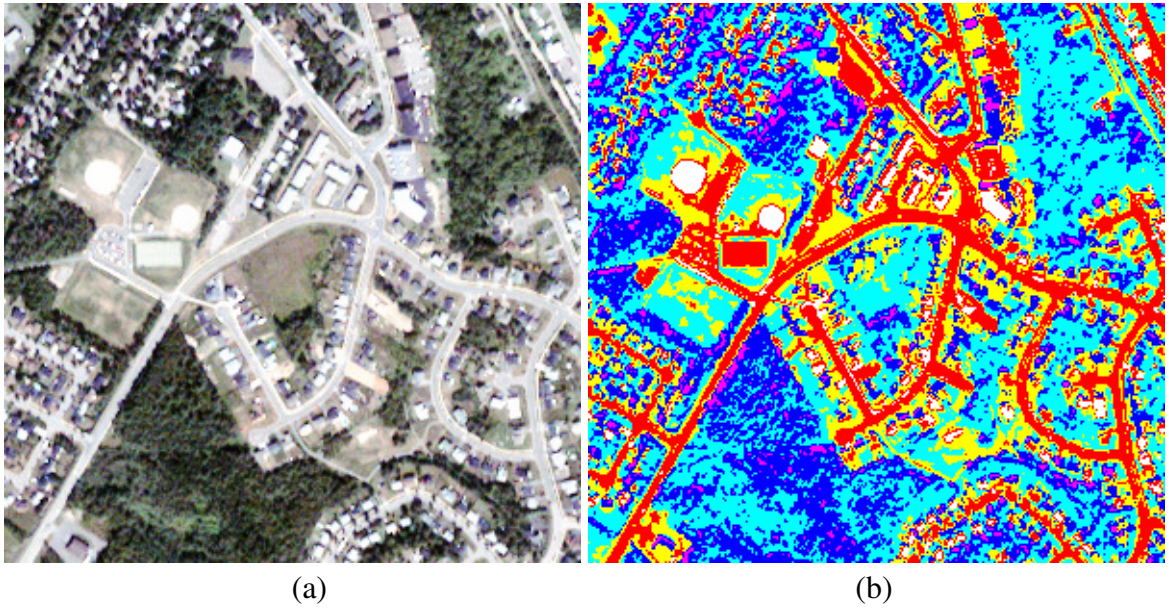


visual inspection and are quite robust. The tested images were captured in different years and covering different areas. Figure 2.4 illustrates the outputs from another Ikonos test image.



**Figure 2.4 Road class identification from another Ikonos MS test image: (a) original true color composite ortho-image; (b) segmented image with the road cluster shown in red.**

It is important to note that the proposed approach can be directly applied to Quickbird MS imagery with a 2.4m spatial resolution without any changes. The identified road cluster in Figure 2.2 (b) is the one shown in red. Figure 2.5 shows the results from another Quickbird test image.



**Figure 2.5 Road class identification from another Quickbird MS test image: (a) original true color composite ortho-image; (b) segmented image with the identified road cluster shown in red.**

## 2.4 Summary

To exploit the spectral information of MSI, the image classification-based approach is selected for road network extraction in favor of its adaptability. Any progress made by the research community in image classification can be easily integrated into the framework to improve the quality of the extracted road networks.

In this research, we propose a simple but efficient clustering algorithm to find the road surfaces on the image. The classification quality is typical of a spectral-based image classification. The road cluster is identified based on a fuzzy logic classifier and will be refined by integrating the texture information in the next chapter.

To achieve a better clustering quality, it is recommended that the number of clusters be optimized using the approaches presented in [Doucette *et al.*, 2001].

## CHAPTER 3

# ROAD CLASS REFINEMENT

As shown in the previous chapter, the classification process is able to locate the road cluster from other land coverage clusters on multi-spectral imagery. The major problem, however, is the high misclassification between the roads and other spectrally similar objects such as parking lots or buildings. The road cluster resulting from the classification is a mix of roads, parking lots, buildings and other spectrally similar objects. Further refinement is required to remove the non-road regions before the road centerline extraction and road network formation. Refinement of the road class is achieved using an advanced application of the Angular Texture Signature (ATS) [Gibson, 2003] and its newly derived shape descriptors. The justification of this approach lies in our observation that roads usually appear as elongate regions while spectrally similar objects are usually open areas.

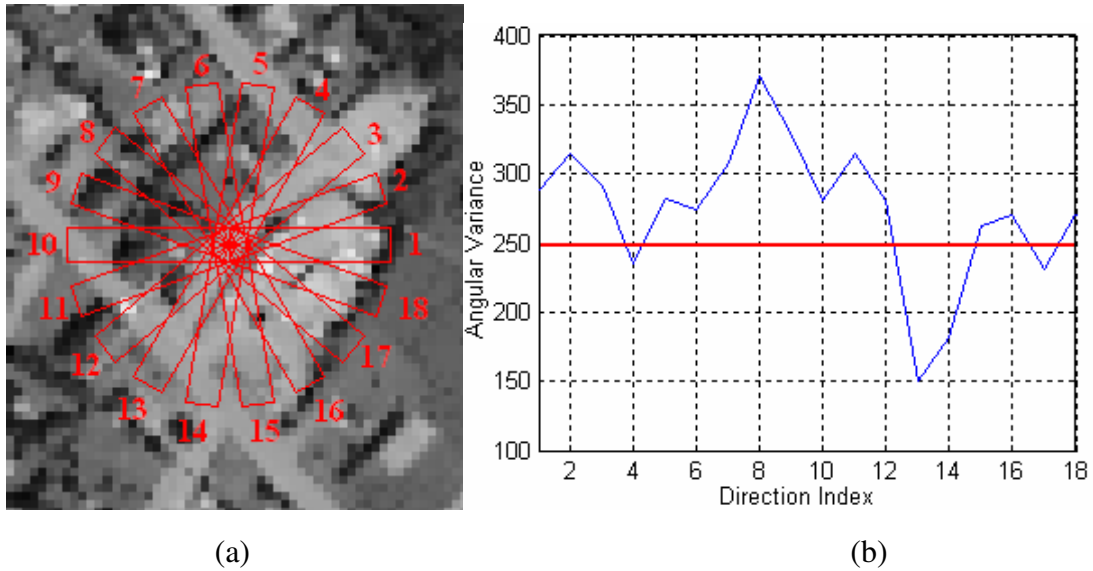
In this chapter, we will give a brief introduction to the basic ATS and define the new shape descriptors of the refined ATS. A classifier will be designed to separate the roads from other spectrally similar objects.

### 3.1 Basic Angular Texture Signature

The Angular Texture Signature (ATS) is a measure developed for road extraction from high resolution panchromatic imagery and is described in [Haverkamp, 2002; Gibson, 2003]. For each pixel  $p$  of a grey level image,  $T(\alpha, w, p)$  is defined as the variance from the mean for a rectangular set of pixels of width  $w$  around the point  $p$  whose principal axis lies at an angle  $\alpha$  from the horizontal. This measure is computed for a set of angles  $\alpha_0, \dots, \alpha_n$ . Figure 3.1(a) shows the templates for a single point. At point  $p$ , the ATS is defined as the set of values  $\{T(\alpha_0, w, p), T(\alpha_1, w, p), \dots, T(\alpha_n, w, p)\}$ .

The graph of an ATS for a single point  $p$  is shown in Figure 3.1 (b). The local minima on this graph correspond to the most likely directions of the road at  $p$  (e.g. direction 4 and 13 in Figure 3.1). For each pixel  $p$ , the number,  $k$ , and the location of the strongest

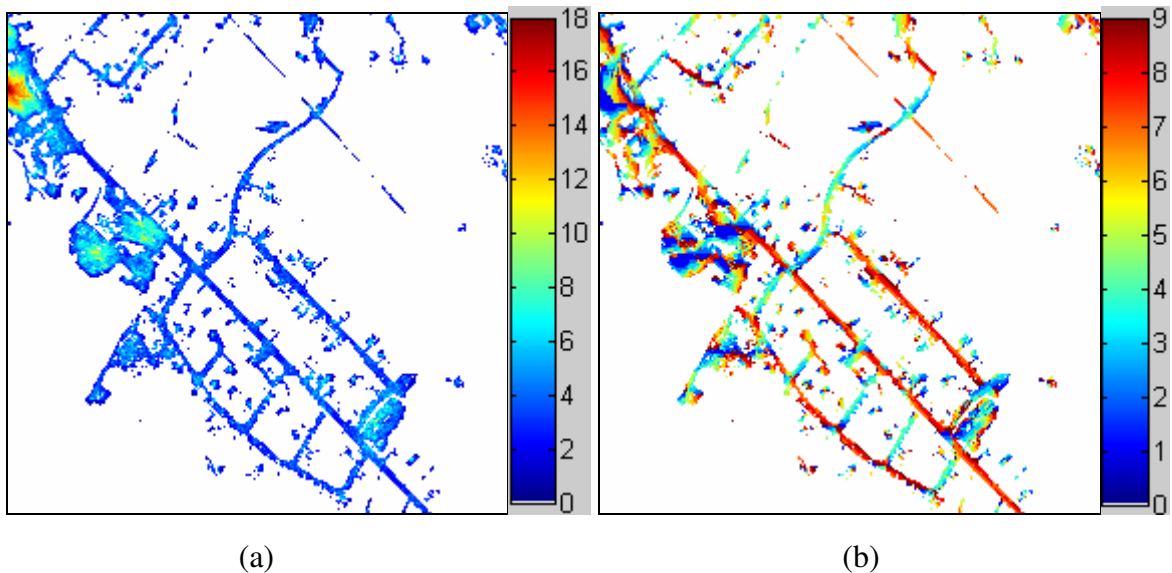
local minima are computed from the ATS. For example, the signature shown in Figure 3.1 (b) has four minima that are significant (i.e. less than 250 in this case). We refer to  $k$  (the number of minima) as the degree of the pixel. The texture measures that are commonly used in road detection are: the degree of the pixel and the direction of the minimum.



**Figure 3.1** Texture is computed over (a) the set of rectangular regions about a pixel and (b) the graph of the Angular Texture Signature for a single pixel. The image used is a subset of an Ikonos MS-red image. For illustration purposes, the size of the rectangular regions is set to 5 by 20 pixels. (After [Gibson, 2003])

To simplify the computations, we define the ATS based solely on the road pixels. The ATS is computed based on the binary image of our road cluster, i.e., where the road pixels are white (pixel value = 1) and the surrounding pixels are black (pixel value = 0). As we are only interested in the road pixels, instead of calculating the variance of the pixel values within the rectangular window, we calculate the mean value, which is equal to the number of road pixels divided by the total number of pixels within the rectangular window. This normalizes the ATS values to the range of [0, 1]. By using a binary image with road pixels given the value of 1, we define the number of maxima

as the ATS-degree of the pixel and the direction of the maximum as the ATS-direction. Figure 3.2 illustrates the ATS-degree and the ATS-direction for the road cluster presented in Figure 2.1. The number of directions computed is set to 18, which is the same value used by Gibson (2003). The size of the rectangular window is determined based on the typical road width in the scene. The width of the rectangular window should be less or equal to the typical road width and its length should be at least twice the width of the typical road. For our data, we use a 5 by 10 pixel window for Ikonos MS imagery and a 5 by 20 pixel window for Quickbird MS imagery.



**Figure 3.2** ATS –degree (a) and direction (b) for the road cluster presented in Figure 2.1. In (b) the direction indices are the same as in Figure 3.1 (a).

As can be seen from Figure 3.2(a), the ATS-degree gives a sense of the location of the parking lots or the other spectrally similar objects (e.g. red area in the upper-left corner). However, the ATS-degree and the ATS-direction are very sensitive to the neighboring pixels. The resulting images are very “noisy” and difficult to threshold. We developed some shape descriptors based on the refined ATS that are more suitable for identifying parking lots and other spectrally similar objects from the roads.

## 3.2 Shape Descriptors of Angular Texture Signature

When examining the ATS of each pixel, some interesting links between the shape of the ATS polygon and the corresponding pixel types are found. To form the ATS polygon, instead of being plotted for each direction along a horizontal line, the ATS values are plotted around the pixel under consideration with the corresponding directions and close the polygon by linking the last point to the first point. The resulting polygon is called the ATS polygon.

Figure 3.3 shows the calculated ATS for some interesting pixels with their corresponding ATS polygons shown in blue. The pixels under consideration are marked with a red cross. For illustration purposes, all of the ATS polygons are enlarged by a factor equal to the length of the rectangular window. In this example, the polygons are enlarged by 10 pixels.

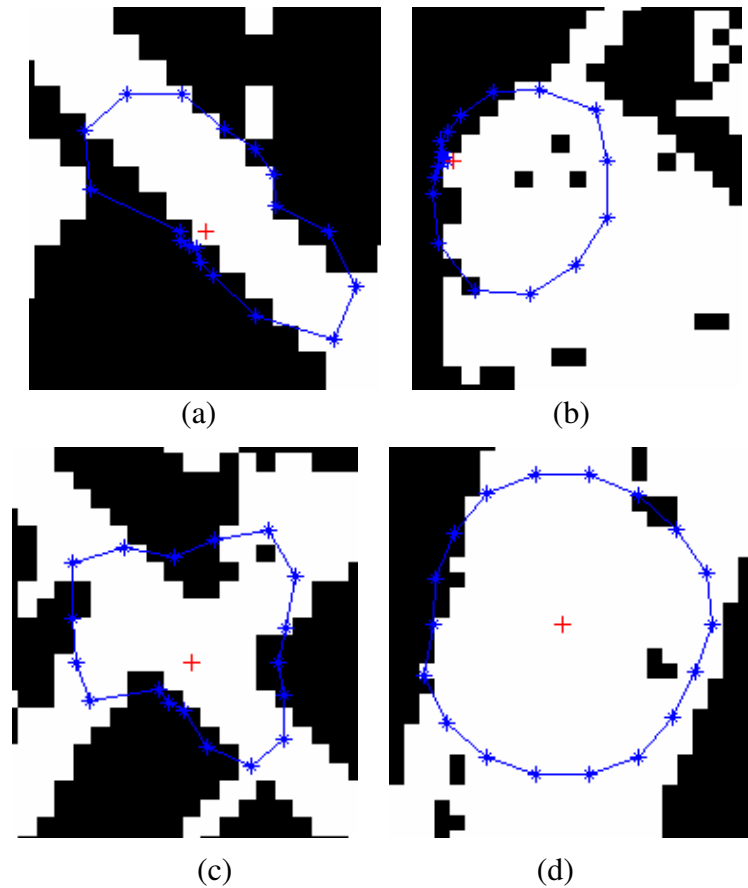
The proposed shape descriptors for the ATS are defined as:

### 1) Mean

The mean of the ATS is defined as the mean ATS value for all directions (Eq. 3.1). It is the average percentage of pixels belonging to the object of interest surrounding the pixel under consideration within the rectangular window. A pixel on a parking lot or building will have a larger ATS-mean than a road pixel. Figure 3.4 (a) confirms this assumption.

$$ATS_{mean} = \frac{1}{n} \sum_{i=1}^n ATS(i) \quad (3.1)$$

where  $n$  is the number of directions.



**Figure 3.3** Angular texture signature for (a) a pixel on a road; (b) a pixel in the corner of a parking lot; (c) a pixel within a T-road junction; and (d) a pixel in a parking lot.

## 2) Compactness

The compactness of the ATS is defined as the compactness of the ATS polygon using Eq. 3.2. It indicates whether the shape of the ATS polygon looks like a circle. A circle-like ATS polygon usually means that the pixel under consideration is on a parking lot or a building (Figure 3.3 (b) and (d)). In Figure 3.4 (b) the parking lots and buildings have very large compactness values.

$$ATS_{compactness} = \frac{4 \cdot \pi \cdot A}{P^2} \quad (3.2)$$

where  $A$  is the area and  $P$  is the perimeter of the ATS polygon.

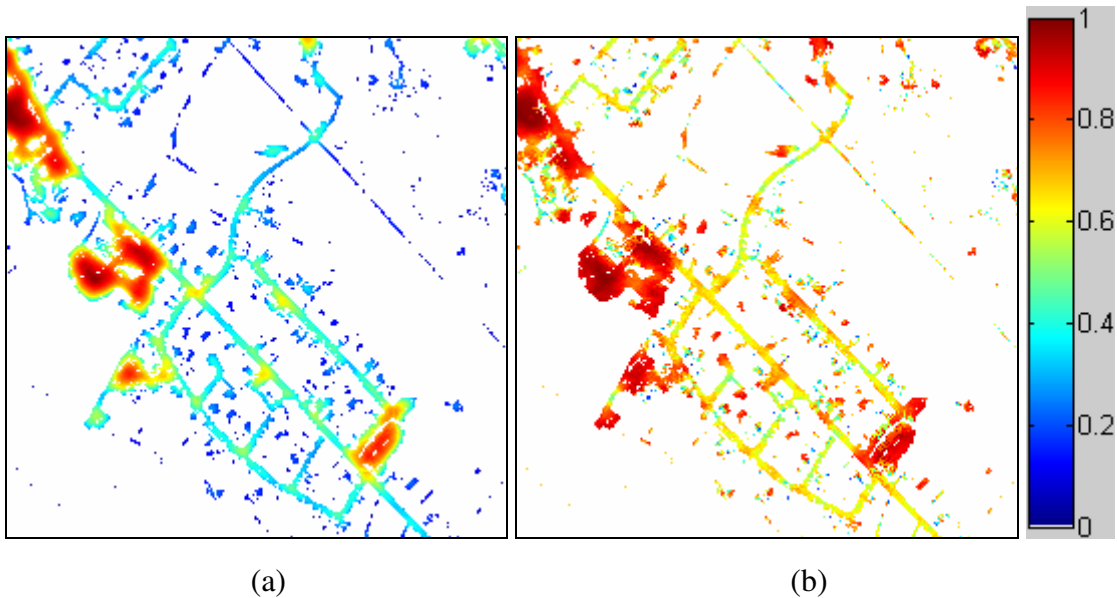


### 3) Eccentricity

The eccentricity of the ATS is defined as the discrepancy between the origin point of the ATS polygon (i.e., the pixel under consideration) and the centroid of the ATS polygon (Eq. 3.3). If a pixel lies at the corner of a parking lot or building, the eccentricity will be relatively larger than those closer to the center of the feature (Figure 3.5). Introducing the ATS-Eccentricity in the detection of parking lots reduces the boundary problem, i.e. the ATS-polygon of a boundary pixel of an open area often has similar shape as that of a road pixel.

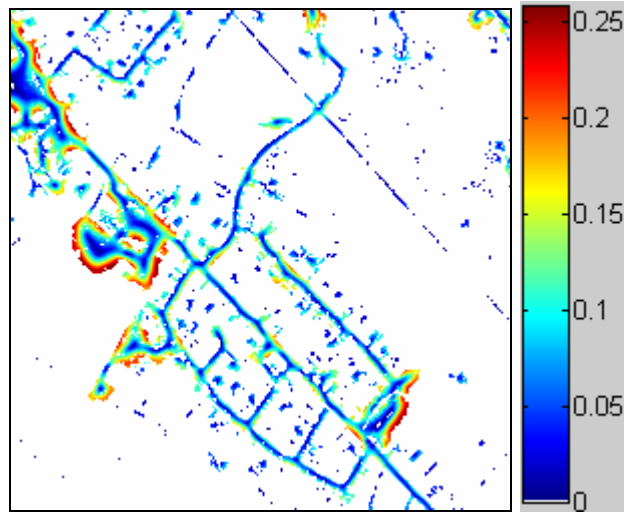
$$ATS_{eccentricity} = \sqrt{(x_c - x_0)^2 + (y_c - y_0)^2} \quad (3.3)$$

where  $(x_c, y_c)$  is the centroid of the ATS polygon and  $(x_0, y_0)$  is the pixel under consideration .



**Figure 3.4** ATS-Mean (a) and ATS-Compactness (b) for the road cluster presented in Figure 2.1

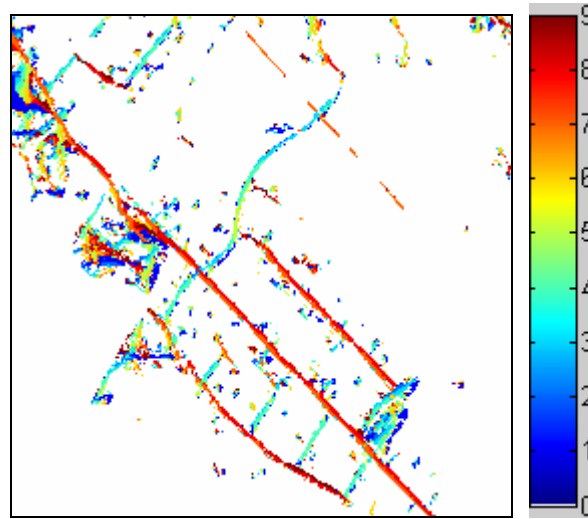




**Figure 3.5** ATS-Eccentricity for the road cluster presented in Figure 2.1

#### 4) Direction

The direction of the ATS is redefined as the direction of the symmetric maximum direction, *i.e.*, if the direction  $n_i$  gives a maximum and one of the directions  $(n_{i-1}, n_i, n_{i+1})$  is also a local maximum then the direction  $n_i$  will be identified as a symmetric maximum direction and will be used as the direction of the ATS. We define the symmetric maximum direction that has the largest combination ATS value (*i.e.*, the sum of the direction pairs) as the ATS direction of this pixel. The new defined ATS-direction is more meaningful and useful in the road network formation process than the original ATS-direction as it gives a robust indication of the possible road direction and is less sensitive to the noisy pixels in the neighborhood. This is evident in Figure 3.6, which shows the coded ATS-direction of the test image (Figure 2.1(a)). The directions of the road pixels are more consistent compared with the basic ATS-direction (Figure 3.2 (b)).



**Figure 3.6** ATS-direction for the road cluster presented in Figure 2.1. The direction indices are the same as in Figure 3.1(a)

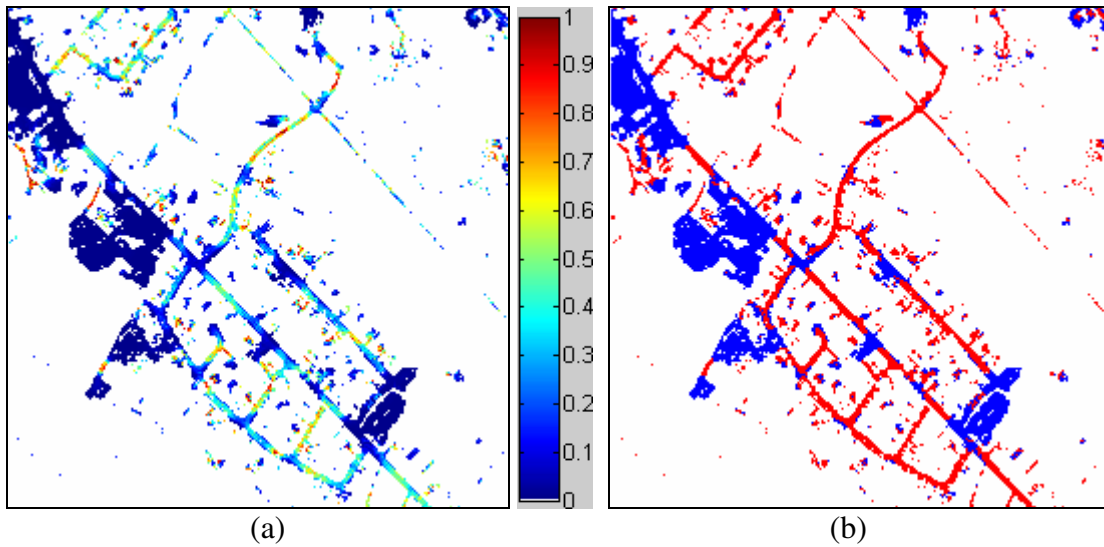
### **3.3 Road Class Refinement Using the Angular Texture Signature**

A fuzzy logic classification is used to separate the roads and parking lots/buildings based on the ATS shape descriptors defined in the previous section. Gaussian membership functions have been chosen to create our fuzzy classification. The parameters used in this step are listed in Table 3.1. Based on our previous definitions, the three shape descriptors (ATS-Mean, ATS-Compactness, and ATS-Eccentricity) have values in the range [0, 1].

**Table 3.1** The parameters used in the Gaussian membership functions for the road class refinement

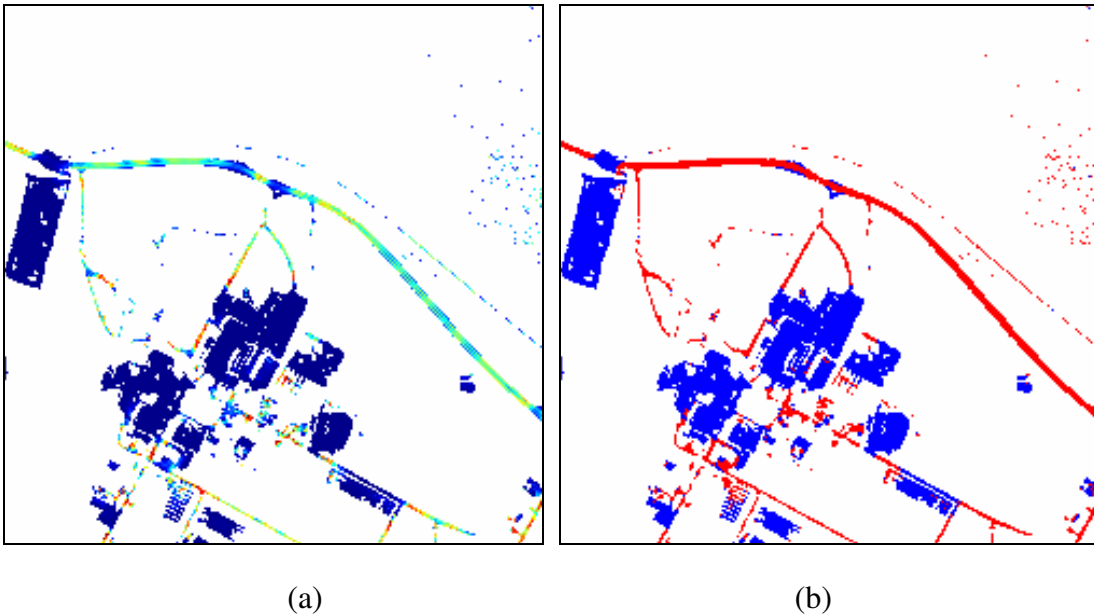
	<b>ATS</b>	<b>ATS-Compactness</b>	<b>ATS-Eccentricity</b>
<b>Mean</b>	0.25	0.40	0.05
<b>Std</b>	0.20	0.20	0.05

Figure 3.7 (a) shows the combined road membership for each pixel belonging to the road cluster binary image presented in Figure 2.1. Figure 3.7 (b) is the result after thresholding Figure 3.7 (a) at a combined membership of 0.1, which is empirically determined.



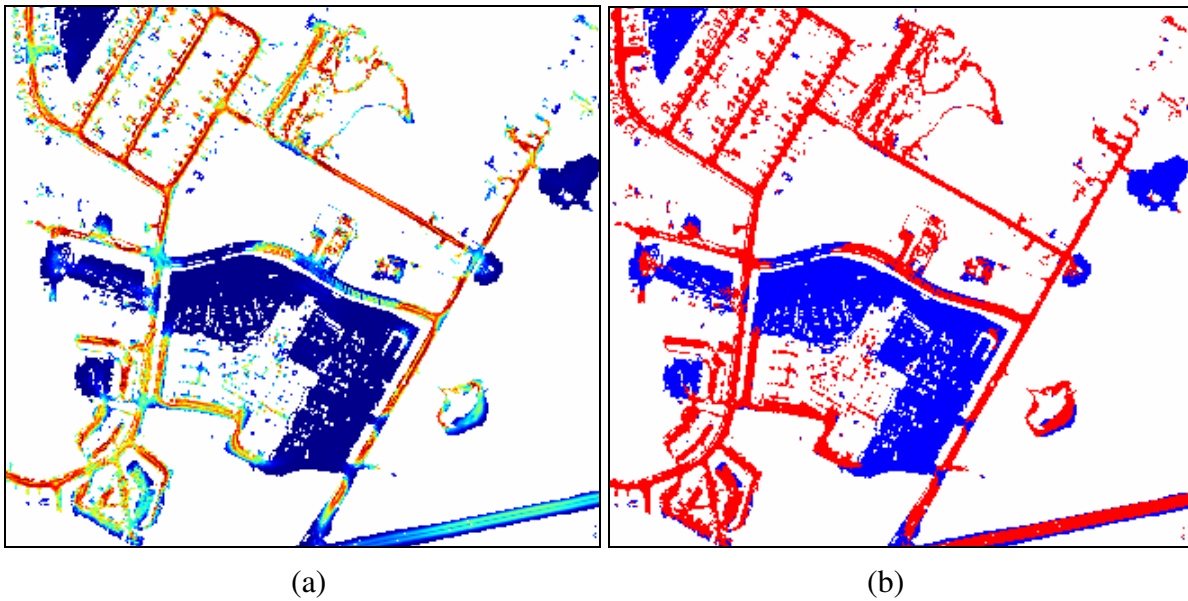
**Figure 3.7 Road membership (a) for the road cluster presented in Figure 2.1; (b) the output after thresholding (a) at 0.1. In (b) white: non-road pixels, red: road pixels, and blue: parking lots/buildings pixels.**

Figure 3.8 is the output for another Ikonos MS test image. Figure 3.9 is the result from the Quickbird MS test image presented in Figure 2.2.

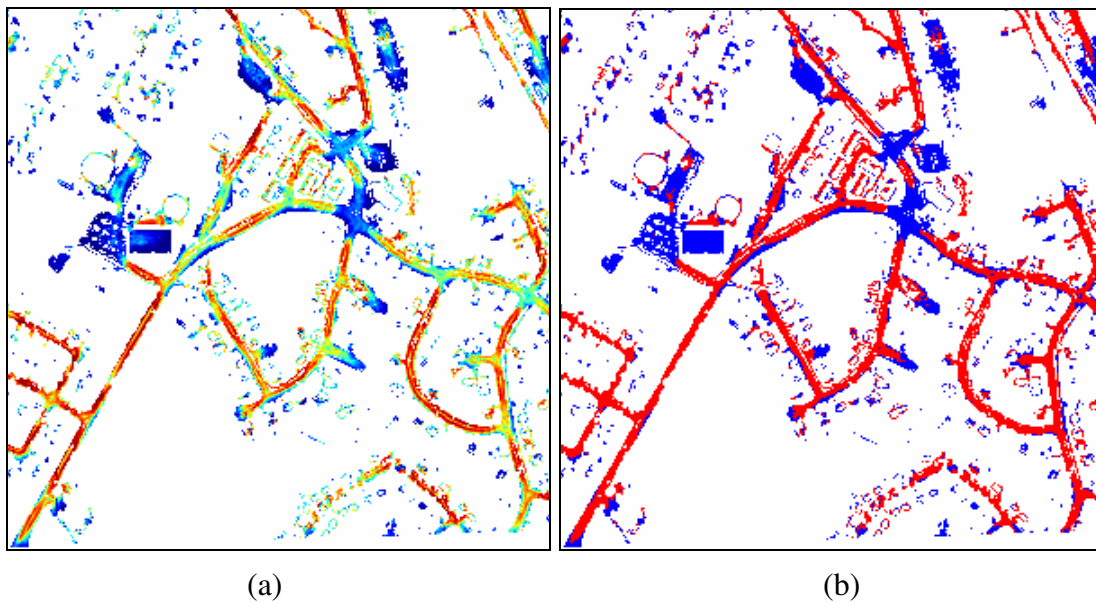


**Figure 3.8 Road membership (a) for the road cluster presented in Figure 2.4; (b) the output after thresholding (a) at 0.1. In (b) white: non-road pixels, red: road pixels, and blue: parking lots/buildings pixels.**

The thresholding value for the image shown in Figure 3.10 is empirically set to 0.4. If a lower value is used, the separation of roads and non-roads is not as complete as that of the other test images. This may be due to the relatively smaller percentage of non-road pixels in the classified image. Figure 3.7 to Figure 3.10 clearly demonstrate that the proposed approach is able to effectively identify the parking lots/buildings or other spectrally similar objects from the roads.



**Figure 3.9** Road membership (a) of the Quickbird MS ortho-image presented in Figure 2.2; (b) the output after thresholding (a) at 0.1. In (b) white: non-road pixels, red: road pixels, blue: parking lots/buildings pixels.



**Figure 3.10** Road membership (a) of the Quickbird MS ortho-image presented in Figure 2.5; (b) the output after thresholding (a) at 0.4. In (b) white: non-road pixels, red: road pixels, blue: parking lots/buildings pixels.

To evaluate the classification results, the non-road pixels (parking lots, buildings, crops, etc) were manually identified from the road cluster images and used as the reference. Table 3.2 shows the overall classification accuracy for the four test images. The kappa statistics were calculated using the approach described in [Congalton and Green, 1999]. In Table 3.2, the five p-values are less than  $10^{-5}$  suggesting that the proposed classification approach is certainly better than random chance.

**Table 3.2 Evaluation of road class refinement**

Test Image	Overall Accuracy	kappa statistics			
		kappa	variance	z-value	p-value
IkonosMS1 (Figure 3.7)	0.70	0.40	0.00007	48.61	$< 10^{-5}$
IkonosMS2 (Figure 3.8)	0.84	0.67	0.00004	99.52	$< 10^{-5}$
IkonosMS3	0.76	0.51	0.00008	58.32	$< 10^{-5}$
QuickbirdMS1 (Figure 3.9)	0.79	0.56	0.00002	128.35	$< 10^{-5}$
QuickbirdMS2 (Figure 3.10)	0.69	0.28	0.00004	42.43	$< 10^{-5}$

Although the overall classification accuracy is satisfactory, the relatively high false alarm rate, i.e., the classification of real road pixels into non-road pixels, is a problem because this misclassification will harm the road network topology. As we can see in Figure 3.7 to Figure 3.10, most of the misclassifications occur for the roads that are closely adjacent to parking lots/buildings, or that are part of major roads intersections. A possible solution will be to integrate the information from the ATS-direction. The ATS-direction of the road pixels (Figure 3.6), even at the road intersections or adjacent to a spectrally similar open area, is robust and consistent in providing clues about the major road direction. The difficulty, however, lies in the modeling of the

consistency of road direction and the integration of this information in the road class refinement.

### **3.4 Summary**

Partially due to the poor image classification accuracy, little research work has been done in road network extraction from MSI. This research proposed a new road identification approach integrating a traditional unsupervised classification, a fuzzy logic classification and a refined angular texture signature. A number of shape descriptors are proposed for the refined angular texture signature and have been used successfully to separate road pixels from parking lots/buildings pixels. Substantial experiments have shown that the proposed methodology is robust and can be applied to reduce the misclassification between roads and other spectrally similar objects for the purpose of road network extraction.

In the next chapter, the classified and refined road pixels will be used to extract road centerlines using an iterative and localized Radon transform.

# CHAPTER 4

## ROAD CENTERLINE EXTRACTION

### 4.1 Introduction

Road centerline extraction from classified imagery affects the positional accuracy of the final extracted road network. This is not a trivial task because there are always misclassified pixels existing in the classified image. These misclassified pixels are either road pixels classified as non-road pixels or non-road pixels classified as road pixels. This results in noisy pixels in the road centerline extraction.

As mentioned in the chapter one, a Radon transform-based line detector is applied in this research. The Radon transform is able to transform images with lines into a domain of possible line parameters, where each line in the image has a peak (for a bright line) or a valley (for dark line) positioned at the corresponding line parameters. This has led to many line detection applications within image processing, computer vision, and seismic applications [Toft, 1996]. The Radon transform-based linear feature detector is less sensitive to noise in the image than other linear feature detectors because the intensity fluctuations due to noise tend to be cancelled out by the process of integration [Murphy, 1986]. Therefore, in remote sensing, it has been widely used in linear feature (e.g. ship wakes) detection from Synthetic Aperture Radar (SAR) images [Murphy, 1986; Copeland *et al*, 1995; Du and Yeo, 2004; Zilman *et al*, 2004]. The Radon transform is closely related to a common computer vision operation known as the Hough Transform [MathWorks, 2005]. The advantages of the Radon transform technique over the conceptually similar Hough transform approach includes: 1) its ability to extract lines from very noisy images [Toft, 1996]; 2) its affordable computational efficiency [Murphy, 1986]; 3) its possibility to detect both bright and dark lines in the same image [Copeland *et al.*, 1995].

However, there are a few issues associated with the Radon transform-based linear feature detector. First, it fails to provide an indication of the line length or the end-



point positions, and cannot be relied upon to detect linear features of short extent [Murphy, 1986]. Secondly, linear features that span the entire image but display some curvature may not produce suitable peaks (or valleys) in the transform domain [Copeland *et al.*, 1995]. Thirdly, locating the peaks is very difficult in some cases (e.g., when the peaks are biased along the two parameter directions) and thus an accurate estimation of the line parameters is not straightforward. Finally, it does not accurately locate the centerline of thick lines but locates their diagonals instead [Clode *et al.*, 2004]. The last two issues are associated with the peak selection of the Radon transform.

In the last two decades, substantial work has been completed to improve the quality of the Radon transform-based linear feature detectors. In [Copeland *et al.*, 1995], the Radon transform is modified to localize the area in which each integration takes place. This reduces the problem of integrating through more noise than necessary, which tends to obscure the peak (or valley) corresponding to a linear feature that is much shorter than the image dimensions. It can also produce better results if the linear features display some curvature. Unfortunately, the localization of the Radon transform prevents us from using the popular frequency domain calculation method [Murphy, 1986] to save computation time.

In their auto-extraction of linear features, such as guard-rails from vehicle-borne laser data, Manandhar and Shibasaki (2002) used a Circle Growing algorithm to locate the end points of the linear features based on a Radon transform. Morphological operations were used to select the peaks from the radon image, which involved dilation using structuring line elements and threshold values of the radon space. However, thresholding after a morphological operation such as dilation does not solve the peak selection problem since the original radon peak is often biased.

Based on the gliding-box algorithm [Cheng, 1999] and the Radon transform algorithm, a novel method for detecting ship wakes in SAR images is proposed in [Du and Yeo, 2004]. This method is applied to both simulated and real SAR images. The result shows that the detection accuracy is satisfactory in a strong noise environment. A

significant feature of the new algorithm is that it can even detect ship wakes that are significantly shorter than the image dimensions.

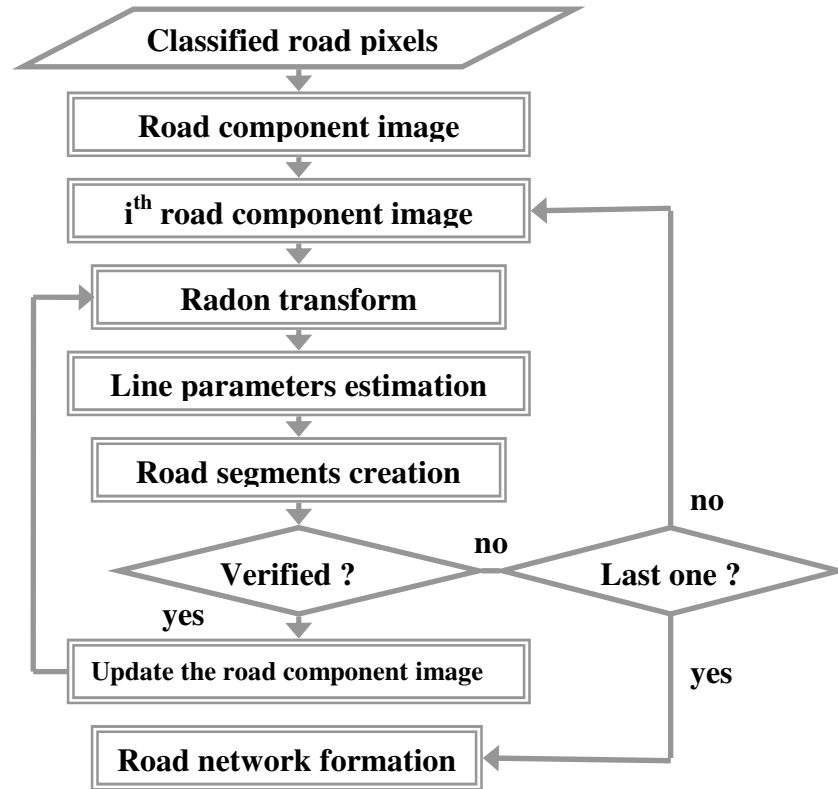
To avoid problems with the detection of thick lines, Clode *et al.* (2004) convolve a raw, pixelated, binary road classification with a complex-valued disk. This technique provides three separate pieces of information about the road or the thick line: its centerline, its direction, and its width at any point along the centerline. The road centerline can be detected from the position of the magnitude peak in the magnitude image resulting from the complex convolution. Road width can be estimated from the magnitude peak while the direction may be obtained from the phase image. Tests on LIDAR data have shown that the proposed methodology was able to detect thick curvilinear lines. However, the technique failed to give proper results with road intersections and it was difficult to determine the road width.

Theoretically, it is simple to detect a line in an image based on the Radon transform. However, in practice, there are many cases where results are not accurate or the line detection fails. In this research, we focus on the peak selection problem to find the centerlines of thick lines based on the Radon transform. It is an important issue that affects applications such as road network extraction on high resolution remotely-sensed imagery.

An iterative and localized Radon transform is developed for the specific application of road network extraction from classified images. The proposed approach is applied to the previously classified and refined road pixels (Figure 4.1), and the goal is to find the road centerlines accurately and completely. It is also able to find short, long, and even curvilinear lines. First, the input space is partitioned into a set of subset images called road component images. An iterative Radon transform is applied locally to each road component image. At each iteration, the road centerline segments are detected based on an accurate estimation of the line parameters including line widths.

The remaining sections of this chapter are organized as follows: Section 4.2 describes the basic Radon transform; Section 4.3 discusses the issues of line detection using the Radon transform with an introduction to the proposed line parameter estimation

techniques; Sections 4.4 and 4.5 are dedicated to the iterative and localized Radon transform and its applications in road centerline extraction from classified imagery; and Section 4.6 summarizes the research and concludes the chapter.



**Figure 4.1** A flowchart of the iterative and localized Radon transform for road network extraction from classified imagery.

## 4.2 The Basic Radon Transform

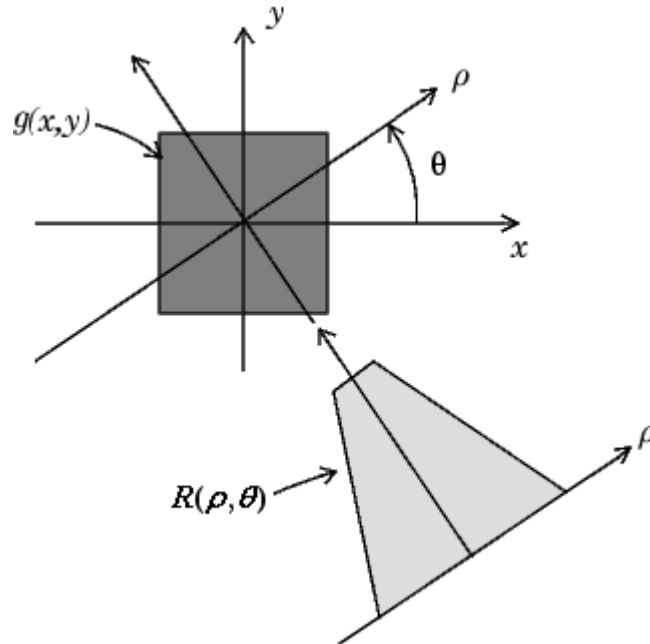
The Radon transform of a function  $g(x,y)$  in a two-dimensional Euclidean space is defined by Eq. 4.1 [Murphy, 1986]:

$$R(\rho, \theta) = \int_{-\infty}^{\infty} \int_{-\infty}^{\infty} g(x, y) \delta(\rho - x \cos \theta - y \sin \theta) dx dy \quad (4.1)$$

where  $\delta(r)$  is the Dirac function which is infinite for argument zero and zero for all other arguments (it integrates to one). The presence of the term  $\delta(\rho - x\cos\theta - y\sin\theta)$  in the definition of the Radon transform forces the integration of  $g(x,y)$  along the line defined by:

$$\rho = x\cos\theta + y\sin\theta \quad (4.2)$$

Consequently, if  $g(x,y)$  is a two-dimensional image intensity function, the computation of its Radon transform yields the projections across the image at varying orientations  $\theta$  and offsets  $\rho$  (relative to a parallel line passing through the image centre) [Murphy, 1986]. The Radon transform should contain a peak corresponding to every line in the image that is brighter than its surroundings and a valley for every dark line. The problem of detecting lines is reduced to detecting the peaks and valleys in the transform domain [Copeland *et al.*, 1995]. The geometry of the Radon transform is illustrated in Figure 4.2.



**Figure 4.2 Geometry of the Radon Transform (After [MathWorks, 2005])**

## 4.3 Line Parameter Estimation in the Radon Transform

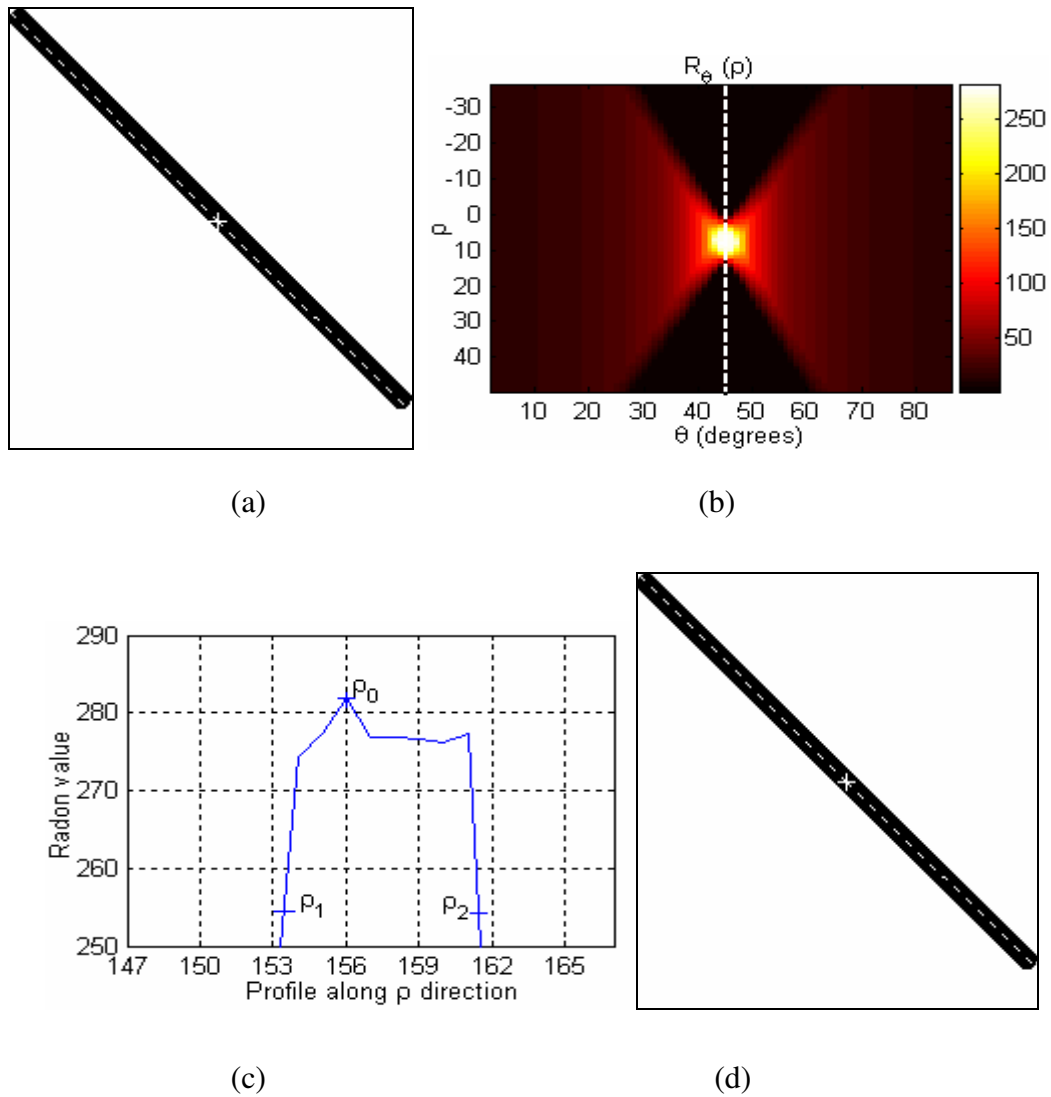
In the context of linear feature detection via the Radon transform, there are three main parameters to be estimated for a straight line: the line direction ( $\theta$ ), the offset ( $\rho$ ) which is relative to a parallel line passing through the image centre, and the line width ( $w$ ). These three parameters are necessary because we are working on real lines, not on geometric lines. In many cases, the estimation of these parameters is not trivial. Complications may occur when the peaks (or valleys) are ambiguous or biased along either the offset ( $\rho$ ) or the direction ( $\theta$ ) or both. In addition, there is a  $\theta$  – boundary problem because the Radon transform is usually calculated based on a limited range of direction angles  $[0, 180^\circ]$ .

All of the test images used in this section are assumed to have bright lines on a dark background. Therefore, only the peaks in the radon space are important. However, for illustration purposes, the following figures use the negative of the input images. For all of the images, the step size of  $\theta$  in the Radon transform is set to one degree.

### 4.3.1 Peak selection

#### 4.3.1.1 Biased radon peak: one direction

Figure 4.3 is an example of a biased peak along the  $\rho$  axis. In Figure 4.3 (a), the black line is approximately five pixels in width and the dashed line is reconstructed from the parameters determined from the original radon peak. As we can see from the figure, the detected line is shifted away from the actual centerline. This occurs because the peak in the radon domain is not a simple unique point but a small peak region (Figure 4.3 (b)), and the  $\rho$  value that forms the peak radon value is biased along the profile in the  $\rho$  axis (Figure 4.3 (c)).



**Figure 4.3** Accurate line parameter estimation in the Radon transform using the profile analysis technique: (a) the input image and the reconstructed line (dashed) based on the original radon peak; (b) the Radon transform; (c) a profile along the  $\rho$  axis shown as a white dashed line in (b) and an illustration of the estimation of the  $\rho$  value; (d) the reconstructed line using the refined radon peak.

To obtain a better estimation of the  $\rho$  value of the line, a profile analysis technique is applied. A profile along the  $\rho$  direction passing the peak is plotted (Figure 4.3 (c)) and two values,  $\rho_1$  and  $\rho_2$ , are determined by using a linear interpolation based on a semi-

peak radon value, which is 90% of the peak radon value (Figure 4.3 (c)). The determination of the semi-peak radon value is based on our observation that the difference between the biased radon peak value and the true radon peak value is usually less than 10%. 90% is selected so that the true radon peak is included in the range while keeping the range as small as possible. Decreasing the number (e.g. to 75%) will not significantly affect the final result if the radon peak region is close to symmetric in the  $\theta$  direction.

However, increasing the number (e.g. to 95%) will risk the loss of the true radon peak in the range. The  $\rho$  value of the line is then determined by the average of these two values:

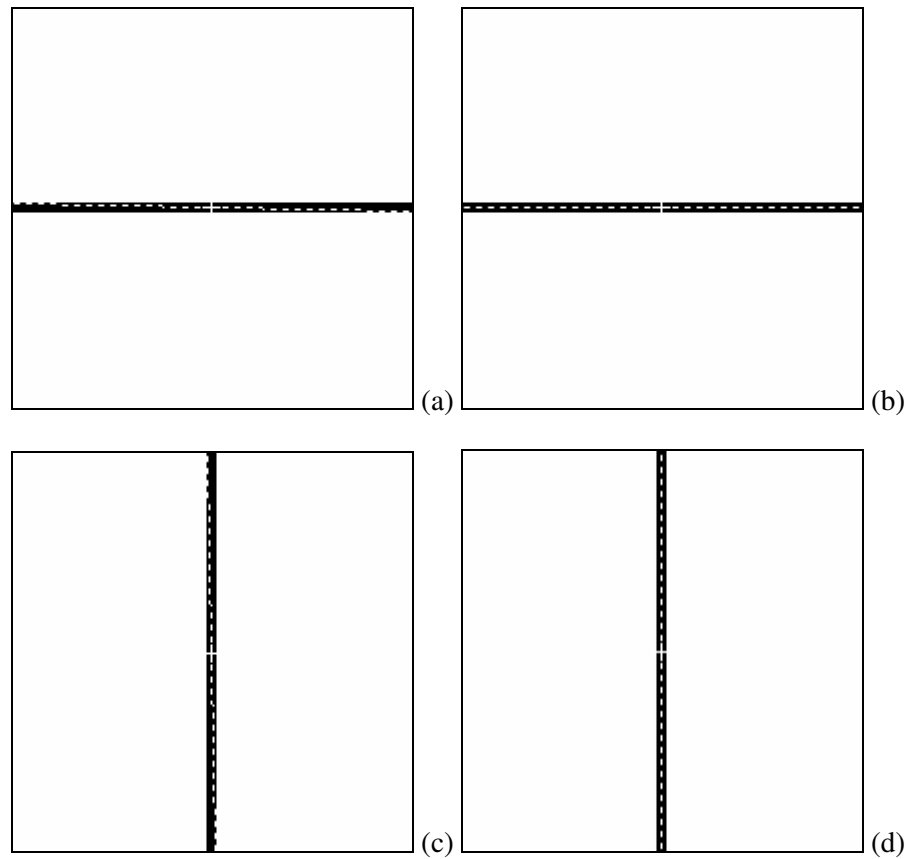
$$\hat{\rho}_0 = (\rho_1 + \rho_2) / 2 \quad (4.3)$$

Similar steps are used for an accurate estimation of the  $\theta$  value:

$$\hat{\theta}_0 = (\theta_1 + \theta_2) / 2 \quad (4.4)$$

The reconstructed line with the new estimated parameters  $(\hat{\rho}_0, \hat{\theta}_0)$  accurately coincides with the actual centerline of the wide black line and is shown in Figure 4.3 (d). It is clear that the proposed method gives a more accurate estimation of the line parameters than using the original radon peak.

Figure 4.4 illustrates results for two other simulated images. The problem with these two images is that the radon peaks are biased along the  $\theta$  axis (Figure 4.4 (a) and (c)). The proposed approach corrects one of the problems with the Radon transform-based line detection: the exact centerline of the thick lines (Figure 4.4 (b) and (d)) is detected instead of the diagonal line, which is the case when the original radon peak is used.



**Figure 4.4** Examples of accurate line parameter estimation in the Radon transform: (a) and (c) show the reconstructed line (dashed) using the original radon peak; (b) and (d) show the reconstructed line (dashed) using the refined radon peak.

#### 4.3.1.2 Biased radon peak: both directions

The profile analysis technique, however, is not applicable if the radon peak is biased in the  $\rho$  and  $\theta$  axes because the true line parameters are no longer located on the profiles passing the peak. Figure 4.5 illustrates this problem. The Radon transform of the input image (Figure 4.5 (a)) is shown in Figure 4.5 (c). A zoomed-in version of the transform is shown in Figure 4.5 (d). The reconstructed centerline based on the original radon peak is shown as a white dashed line in Figure 4.5 (a). It is clear that the

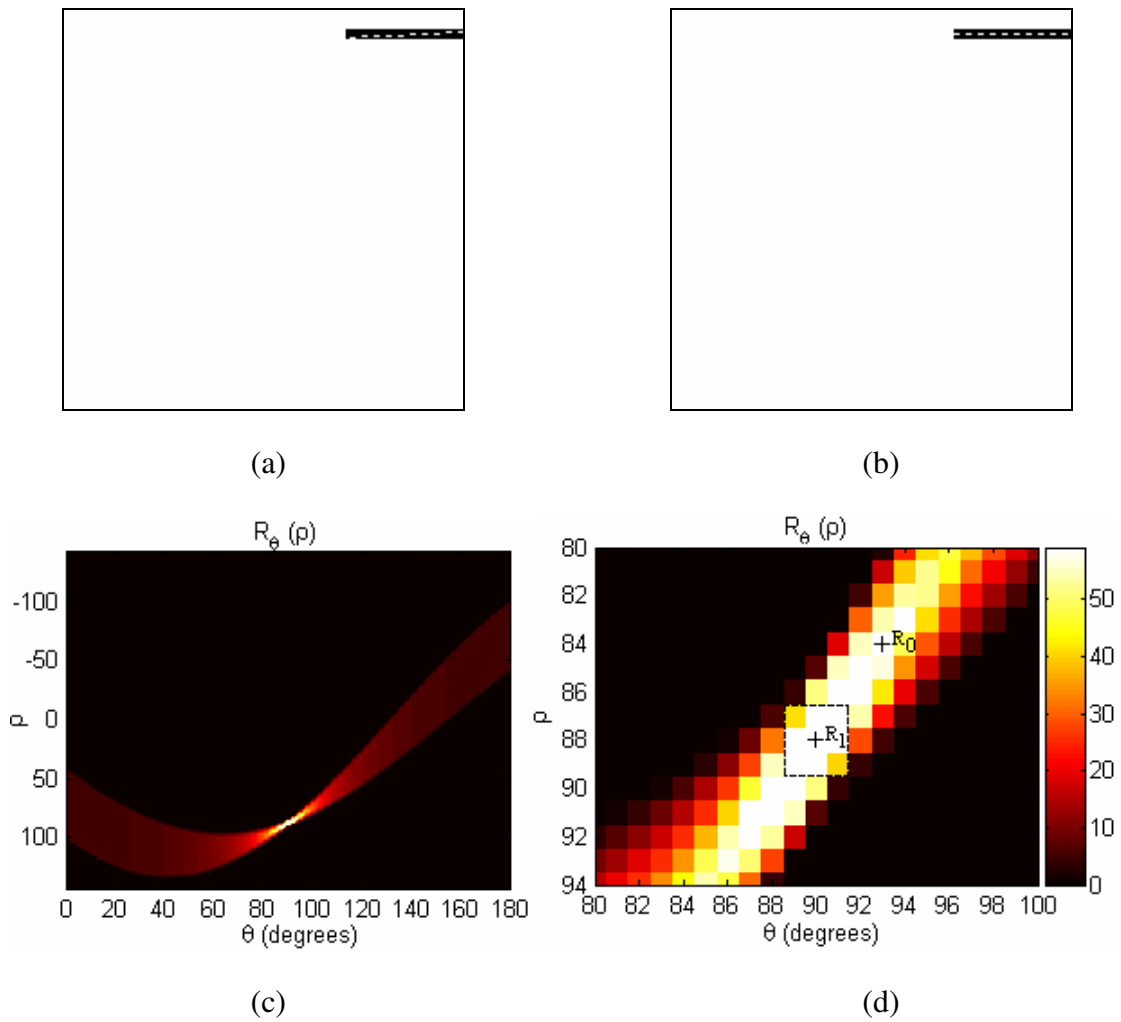


centerline is not accurate. Numerically, the radon peak is located at  $R_0 (84.0, 93.0^\circ)$ . The refined radon peak using the profile analysis approach is located at  $(84.1, 92.8^\circ)$ . Although it is closer to the true position  $R_1 (88.0, 90.0^\circ)$ , it is not perfectly accurate.

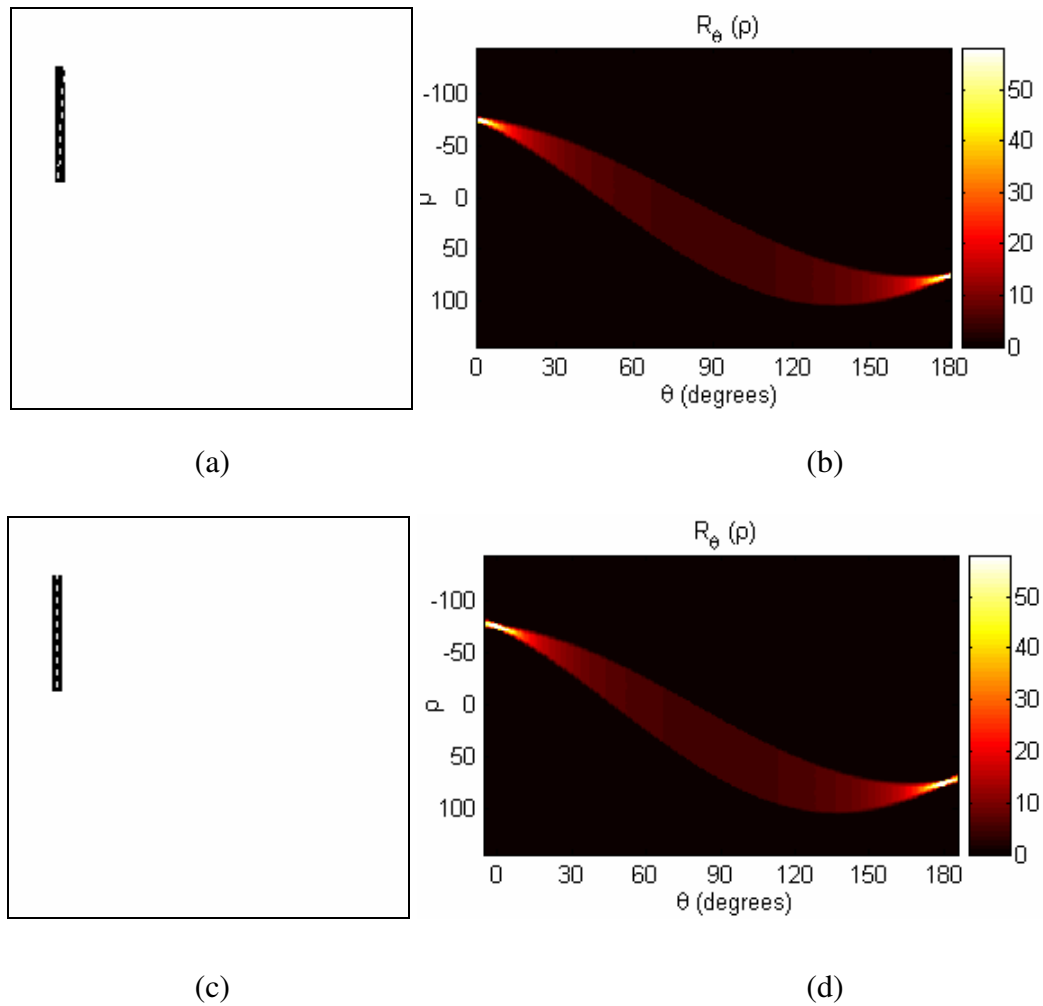
A low-pass filter applied to the radon image will remove the undesirable variations and make it easier to find the true radon peak. The low-pass filter can be a mean filter, a Gaussian filter, or a median filter. The simplest mean filter was chosen for use in this research. The element with the highest mean radon value within the filter window is selected as the peak and is used to estimate the line parameters (Figure 4.5 (d)). The choice of the filter size is mainly based on the average thickness of the lines. Experiments show that the filter size should be less than but close to the average thickness of the lines. For example, a 3 by 3 filter is used for an average width of 5 pixels and a 7 by 7 filter for an average width of 10 pixels. The filter size used in this example is 3 by 3. The improved result is shown in Figure 4.5 (b).

#### **4.3.1.3 $\theta$ -boundary problem**

The  $\theta$ -boundary problem of the Radon transform is associated with vertical lines. The peak region corresponding to a vertical line is artificially divided into two discontinuous parts in the Radon transform because the  $\theta$  used is between 0 and 180 degrees. The true radon peak corresponding to the true line parameters is exactly located on the boundary ( $\theta=180^\circ$ ). Both the profile analysis and mean-filter method fail to locate the true radon peak because of the  $\theta$ -boundary problem. Figure 4.6 illustrates this problem. The Radon transform of the input image (Figure 4.6 (a)) is shown in Figure 4.6 (b), where the  $\theta$ -boundary problem is evident. The solution is to use values of  $\theta$  from  $-5^\circ$  to  $185^\circ$  in the Radon transform to allow an overlapping area along the  $\theta$  axis (Figure 4.6 (d)). The final result is shown in Figure 4.6 (c).



**Figure 4.5** Accurate line parameter estimation in the Radon transform using a mean filter: (a) the input image and the reconstructed centerline (dashed) based on the original radon peak; (b) the reconstructed line (dashed) using the refined line parameters based on the radon peak found by a mean filter; (c) the Radon transform; (d) zoomed in version of (c).  $R_0$  - the original radon peak;  $R_1$  - the radon peak found by the mean filter, the black dashed line shows the window used.

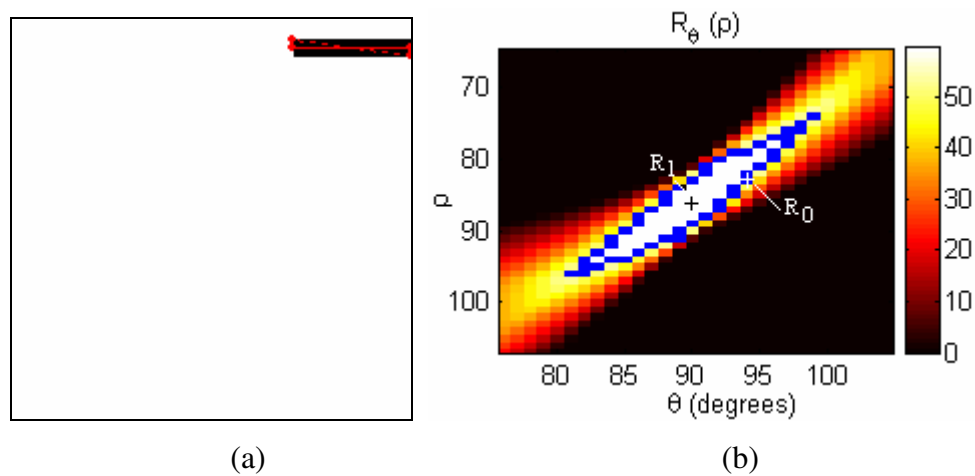


**Figure 4.6 Example of  $\theta$ -boundary problem of the Radon transform: (a) input image with the reconstructed line (dashed) based on the original radon peak; (b) the Radon transform; (c) the new reconstructed line (dashed) using the refined line parameters; (d) the expanded Radon transform with  $\theta$  as  $[-5^\circ, 185^\circ]$ .**

#### 4.3.1.4 Robust approach to peak selection

As mentioned above, the estimation of the line parameters ( $\rho$  and  $\theta$ ) is related to the peak selection problem. The radon peak will be biased in both axes ( $\rho$  and  $\theta$ ) due to the limitation of the directional integration in the Radon transform. The solution is to use the profile analysis technique and a low-pass filter in the Radon domain. These techniques, however, do not work well for wide lines in an image because they create

a small area of peaks, called a radon peak region, not a single peak in the radon space. This is evident in Figure 4.7. In the simulated image (Figure 4.7 (a)) there is one wide line with a width of 9 pixels. The Radon transform of the input image is shown in Figure 4.7 (b) where the radon peak value is marked as a white cross ( $R_0$ ). The detected centerline (red dotted line in Figure 4.7 (a)) from this single radon peak is obviously biased since the directional integration of the diagonal line yields the largest value.



**Figure 4.7 Peak selection problem in the Radon transform: (a) input image with a wide line, the red dotted line is the detected centerline using the single radon peak, the red solid line is the detected centerline using the refined radon peak; (b) the Radon transform of (a), where  $R_0$  is the single radon peak,  $R_1$  is the refined radon peak. The blue line depicts the radon peak region.**

To correctly estimate the line parameters, the radon peak region is used instead of the single radon peak. The radon peak region is defined as the connected radon elements which have a radon value larger than ninety percent of the radon peak value. Ninety percent is selected so that the true radon peak is included in the range while keeping the range as small as possible (see an explanation in Section 4.3.1.1). In this research, the radon peak region is found using a region growing algorithm in the radon space

starting from the radon peak. In Figure 4.7 (b), the radon peak region is the region bounded by the blue line. The centroid of the radon peak region ( $R_1$  in Figure 4.7 (b)) is then used to estimate the line parameters. The centerline detected using the refined radon peak (the red solid line in Figure 4.7 (a)) accurately coincides with the true centerline. Intensive experimentation has shown that the proposed peak selection approach is accurate and robust for the estimation of line parameters in the Radon transform.

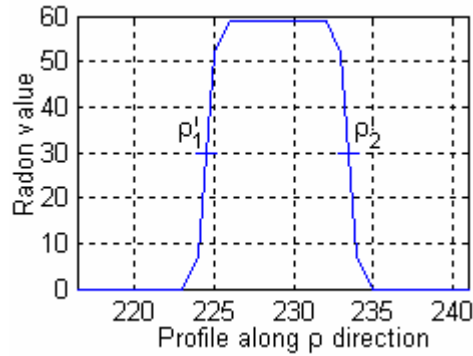
### 4.3.2 Line width estimation in the Radon transform

The estimation of line width is important for many linear feature detection applications such as road network extraction from remotely sensed imagery. Different road widths often indicate different road classes. However, most road detectors fail to provide an accurate and robust estimation of road width. A dynamic programming approach (e.g. [Gruen and Li, 1997]) does not provide any information on line width. In a template matching approach (e.g. [Hu *et al.*, 2004b]), line width is usually preset with limited adjustability during the matching process. Line width estimated from a profile analysis technique (e.g. [Wang and Zhang, 2000; Hu and Tao, 2005]) or from a morphological thinning-based approach (e.g. [Song and Civco, 2004]) is often sensitive to any noisy pixels. These techniques fail to provide a meaningful line width for a real road. With a Radon transform-based linear feature detector, the line width for each detected line segment can be estimated.

The width ( $W_\rho$ ) in the  $\rho$  axis of a peak in a Radon transform provides an estimate of the mean width of the corresponding linear feature [Murphy, 1986]. In this research, two  $\rho$  values,  $\rho'_1$  and  $\rho'_2$ , are determined based on the half-peak radon value, which is fifty percent of the peak radon value (Figure 4.8). The half-peak radon value is used in the mean line width calculation since any pixel contributing to the half-peak radon value during the radon integration should be taken into consideration in the line width calculation. The width,  $W_\rho$ , is then calculated using the following equation:

$$W_\rho = \rho'_2 - \rho'_1 \quad (4.5)$$

The width of the line shown in Figure 4.7 is exactly 9 pixels and the estimated line width is also 9 pixels.



**Figure 4.8 Line width estimation in the Radon transform:  $\rho'_1$  and  $\rho'_2$  are two points located along the profile in the  $\rho$  direction at the refined radon peak ( $R_1$ ) shown in Figure 4.6 (b). They are determined by the half peak radon value.**

The results from a number of simulated test images are summarized in Table 4.1. The real line widths are calculated based on the geometric relationship illustrated in Figure 4.9 and the equation below:

$$\frac{w}{a} = \frac{b}{c} = \frac{b}{\sqrt{a^2 + b^2}} \Rightarrow w = \frac{ab}{\sqrt{a^2 + b^2}} \quad (4.6)$$

The values of  $a$  and  $b$  are manually measured on the input images once the images are zoomed in enough to ensure measurement accuracy at an approximate level of  $\pm 0.1$  pixels. It is clear that the proposed approach is capable of estimating an accurate line width based on the Radon transform. The mean of the errors is  $+0.1$  pixels and the standard deviation is approximately  $\pm 0.2$  pixels. This indicates that the accuracy of line width estimation is very close to that of a manual measurement.

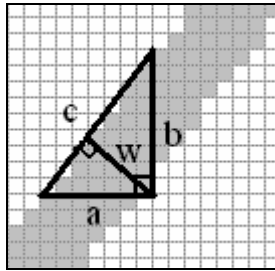


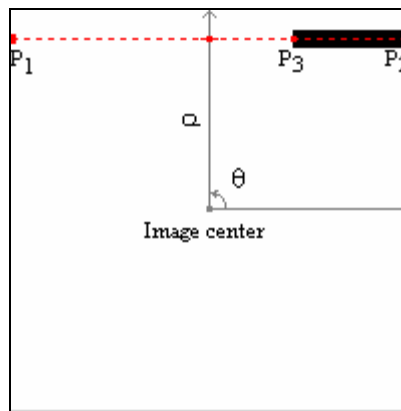
Figure 4.9 Calculation of line width

Table 4.1 Line width estimation (in pixels)

Line No	Real value	Estimated	Error
1	4.2	4.5	-0.3
2	9.9	9.5	0.4
3	9.9	9.5	0.4
4	5.0	4.8	0.2
5	5.0	4.8	0.2
6	5.0	4.8	0.2
7	5.0	4.8	0.2
8	5.0	4.7	0.3
9	5.0	4.9	0.1
10	5.0	4.7	0.3
11	5.0	4.9	0.1
12	5.0	4.9	0.1
13	5.0	4.9	0.1
14	3.0	3.0	0.0
15	4.2	4.0	0.2
16	4.2	4.0	0.2
17	4.2	4.4	-0.2
18	4.3	4.6	-0.3
19	4.2	4.3	-0.1
20	4.2	4.3	-0.1
<b>Mean</b>			<i>0.1</i>

### 4.3.3 Endpoint determination

The Radon transform does not provide any information about the endpoints of a given line segment. Therefore, the endpoints have to be determined in the original image space. In this research, the endpoints are constructed by overlaying the detected centerlines on the original image. For the example shown in Figure 4.10, the centerline  $\overline{P_1P_2}$  is reconstructed from the estimated line parameters  $(\rho, \theta)$ . The centerline segment  $\overline{P_2P_3}$  is then created by overlaying  $\overline{P_1P_2}$  on the original image. In this step, more than one centerline segment can be found. These centerlines will be recorded if their lengths are greater than a certain threshold (e.g. 10 pixels).



**Figure 4.10** Endpoints determination

### 4.3.4 Experiments

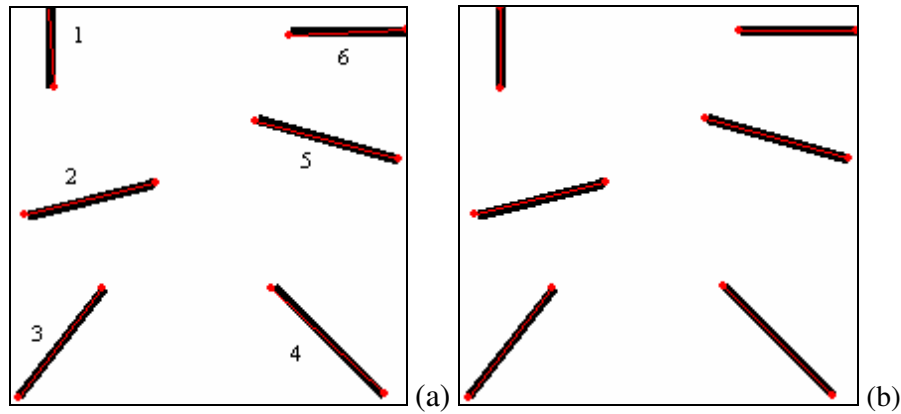
The proposed Radon transform method has been tested on numerous images. The results will be discussed in the following sections.

#### 4.3.4.1 Synthetic image

A typical result from one of the simulated images is illustrated in Figure 4.11. Figure 4.11 (a) shows the reconstructed centerlines based on the original radon peaks. Figure 4.11 (b) presents the results from our proposed approach. As can be seen from lines 1,



4, and 6, the results from our method are more accurate than those from the original method. The estimated line widths are shown in Table 4.2. The mean error is only 0.1 pixels.



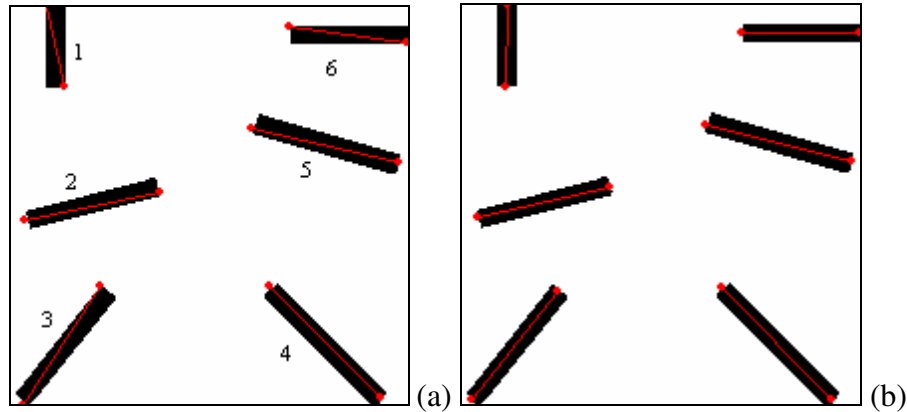
**Figure 4.11** Centerline detection using the Radon transform from the first synthetic image: (a) the reconstructed lines (red) based on the original radon peaks; (b) the improved results.

**Table 4.2** Line width estimation for the first synthetic image (in pixels)

Line No	Real value	Estimated	Error
1	5.0	5.0	0.0
2	5.0	5.1	-0.1
3	4.6	4.5	0.1
4	4.2	4.2	0.0
5	5.0	5.1	-0.1
6	5.0	5.0	0.0
<i>Mean</i>			0.0

Results from Figure 4.12 indicate that the proposed approach is applicable to centerline detection of thick lines. The six line widths are approximately 10 pixels.

The improvements are evident when comparing Figure 4.12 (b) with Figure 4.12 (a). The estimated line widths (Table 4.3) are also very accurate. This indicates that the proposed method is not sensitive to line width.



**Figure 4.12** Centerline detection of thick lines using the Radon transform from the second synthetic image: (a) the reconstructed lines (red) based on the original radon peaks; (b) the improved results.

**Table 4.3** Line width estimation for the second synthetic image (in pixels)

Line No	Real value	Estimated	Error
1	10.0	10.0	0.0
2	9.7	9.5	0.2
3	10.1	9.7	0.4
4	9.9	9.8	0.1
5	10.6	10.4	0.2
6	9.0	9.0	0.0
<i>Mean</i>			0.2

To evaluate the positional accuracy of the extracted centerlines, we manually extracted the centerline segments for both sets of synthetic images. These segments were used

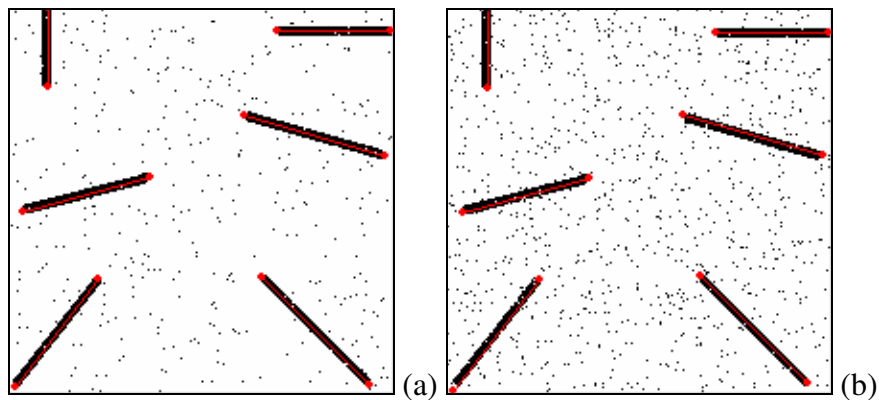
as our reference data. The extracted centerlines using the improved Radon transform are then assessed against the reference data based on the line segment matching technique, which is an algorithm developed for quality assessment for automated road extraction. Details of the assessment method can be found in Chapter 6. The evaluation results are shown in Table 4.4. The average positional accuracy is about 0.5 pixels. Although there are no widely accepted accuracy standards for linear feature extraction, it is reasonable to consider that sub-pixel (less than or equal to 1.0 pixel) positional accuracy is accurate enough for the application of road network extraction.

**Table 4.4 Positional accuracy assessment (in pixels)**

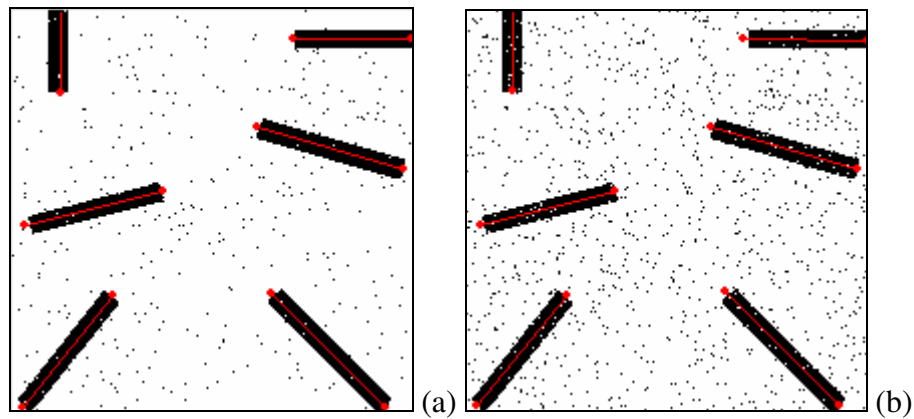
<b>Synthetic Image One</b>		<b>Synthetic Image Two</b>	
<b>Line No</b>	<b>Error</b>	<b>Line No</b>	<b>Error</b>
1	0.30	1	0.55
2	0.91	2	0.77
3	0.35	3	0.20
4	0.69	4	0.41
5	0.20	5	0.25
6	0.04	6	0.61
<b>Mean</b>	<i>0.41</i>	<b>Mean</b>	<i>0.47</i>

#### **4.3.4.2 Synthetic image with noise**

To test the robustness of the proposed method, we added salt and pepper noise with 0.02 and 0.05 noise densities to the original images. The outputs are shown in Figure 4.13 and Figure 4.14. The estimated line widths are listed in Table 4.5 and Table 4.6, respectively. The extracted centerlines from the noisy images are less accurate than those from the noise-free images, but all are well within an acceptable quality threshold (see Table 4.7 for a positional accuracy assessment). This confirms that the proposed method is able to accurately extract the centerlines and precisely estimate the line widths from a noisy image.



**Figure 4.13** Centerline detection using the improved Radon transform for synthetic image one with added noise density of: (a) 0.02; (b) 0.05.



**Figure 4.14** Centerline detection using the improved Radon transform for synthetic image two with added noise density of: (a) 0.02; (b) 0.05.

**Table 4.5 Line width estimation for the first synthetic image with added noise (in pixels)**

Line No	Real value	Noise Density 0.02		Noise Density 0.05	
		Estimated	Error	Estimated	Error
1	5.0	5.1	-0.1	5.1	-0.1
2	5.0	5.2	-0.2	5.3	-0.3
3	4.6	4.6	0.0	4.5	0.1
4	4.2	4.3	-0.1	4.3	-0.1
5	5.0	5.2	-0.2	5.1	-0.1
6	5.0	5.0	0.0	5.2	-0.2
		<b>Mean</b>	-0.1	<b>Mean</b>	-0.1

**Table 4.6 Line width estimation for the second synthetic image with added noise (in pixels)**

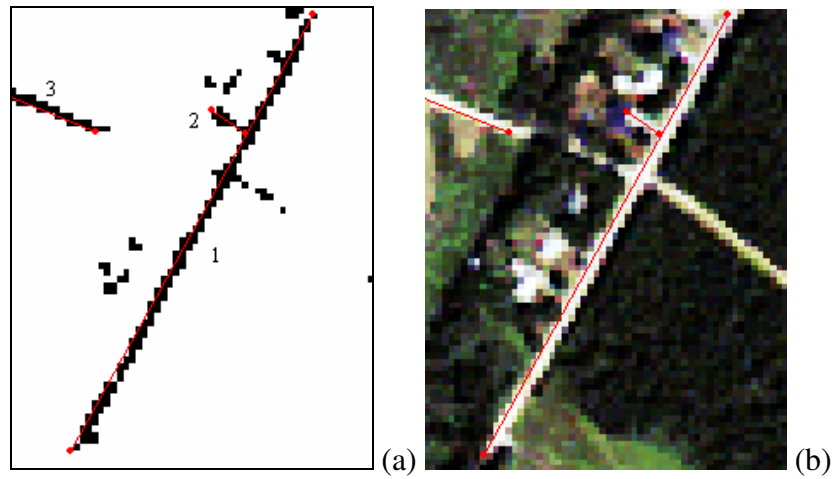
Line No	Real value	Noise Density 0.02		Noise Density 0.05	
		Estimated	Error	Estimated	Error
1	10.0	10.1	-0.1	10.2	-0.2
2	9.7	9.5	0.2	9.6	0.1
3	10.1	9.8	0.3	9.9	0.2
4	9.9	9.8	0.1	10.0	-0.1
5	10.6	10.5	0.1	10.6	0.0
6	9.0	9.0	0.0	9.2	-0.2
		<b>Mean</b>	0.1	<b>Mean</b>	0.0

**Table 4.7 Positional accuracy assessment with added noise (in pixels)**

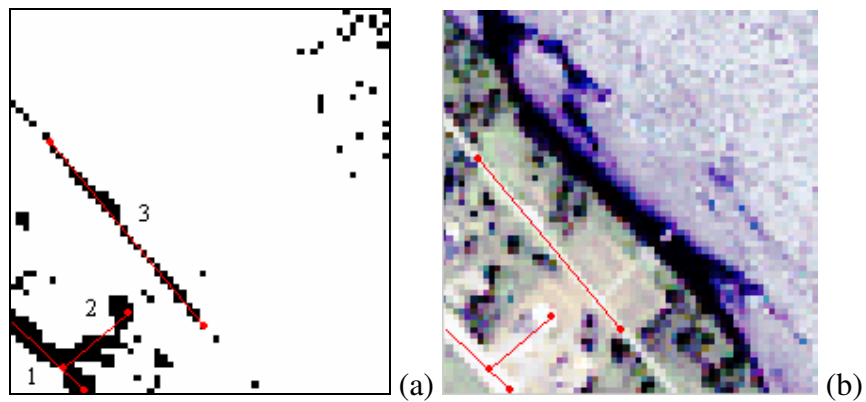
Synthetic Image One			Synthetic Image Two		
Line No	Noise Density		Line No	Noise Density	
	0.02	0.05		0.02	0.05
1	0.08	0.58	1	0.53	0.36
2	1.04	0.91	2	0.77	0.77
3	0.35	1.18	3	0.34	0.27
4	0.69	0.40	4	0.71	0.25
5	0.40	0.20	5	0.14	0.29
6	0.00	0.33	6	0.72	1.06
<b>Mean</b>	<i>0.43</i>	<i>0.60</i>	<b>Mean</b>	<i>0.53</i>	<i>0.50</i>

#### 4.3.4.3 Real classified satellite image

The proposed Radon transform has also been applied to a set of classified images. Figure 4.15 and Figure 4.16 illustrate some of the results of the road centerline extractions. From Figure 4.15 and Figure 4.16, we can see that the proposed methodology is able to detect road segments on classified imagery with a good estimation of road width and positional accuracy. The failure to detect the right road in Figure 4.15 (b) is due to the misclassification in the image segmentation step, i.e., most of the road pixels have been misclassified as non-road pixels (see Figure 4.15 (a)).



**Figure 4.15** Detected road centerlines (red) overlaid on the road pixels (a) and the Ikonos MS true composite image (b). The estimated line widths for lines 1-3 are 2.4, 2.3 and 2.2 pixels respectively.



**Figure 4.16** Detected road centerlines (red) overlaid on the road pixels (a) and the Ikonos MS true composite image (b). The estimated line widths for lines 1-3 are 3.3, 3.9 and 2.0 pixels respectively.

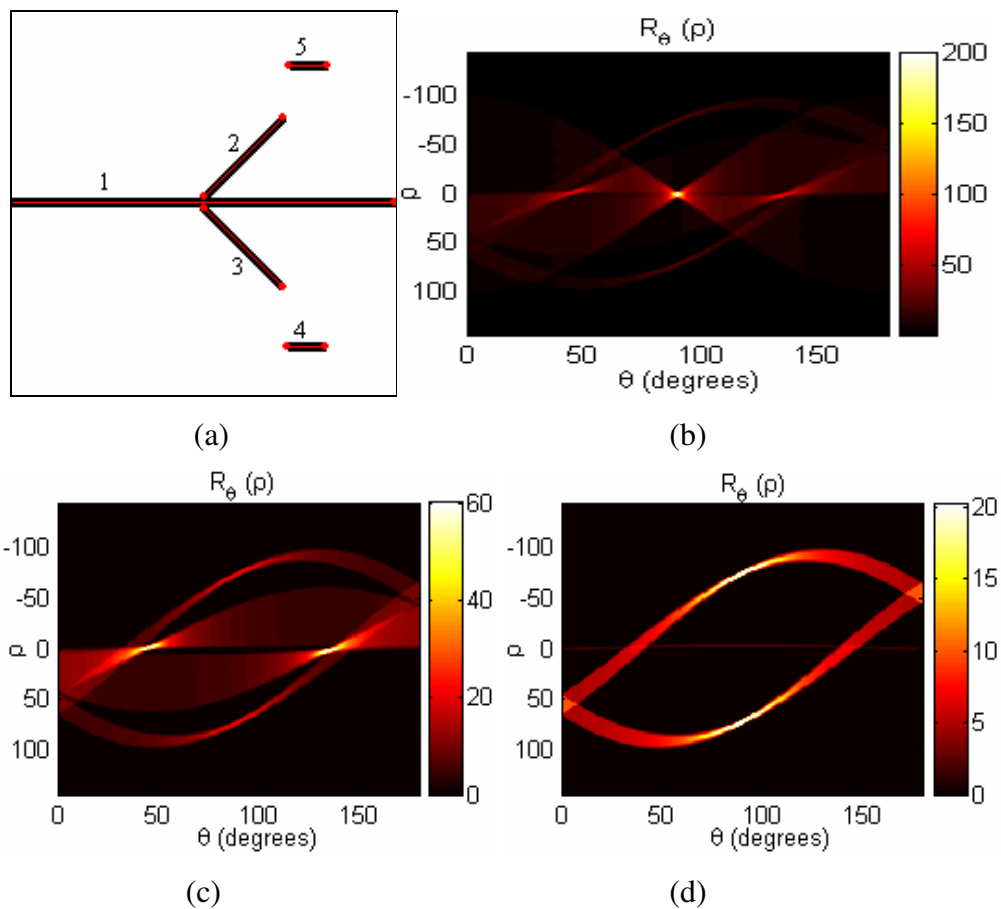
## 4.4 Iteration of the Radon Transform

Studies have shown that iteratively applying the Radon transform will help to extract short lines in an image because short lines usually do not generate detectable peak responses in the radon space. For example, for the input image shown in Figure 4.17 (a), it is very difficult to find the radon peaks corresponding to the two shortest lines (line 4 and 5) in the radon space (Figure 4.17 (b)).

Similar to the idea of the iterative Hough transform used in [Hu *et al.*, 2004a], an iterative Radon transform is developed to accurately extract the road centerlines on a binary image. Each iteration in the Radon transform is composed of three steps: (1) the Radon transform is applied to the entire input image; (2) the possible road segments are detected based on the refined peak radon value; and (3) the line widths are estimated and used to remove the road pixels belonging to the detected road segments. This process continues until no more road segments are detected.

For the previous example, Figure 4.17 (c) shows the Radon transform after the longest line (line 1) has been detected and its pixels removed from the image. Two radon peaks corresponding to the two middle length lines (line 2 and 3) are clearly visible and can be detected. Similar steps are applied to the remaining image to detect the two shortest lines (line 4 and 5) based on the Radon transform shown in Figure 4.17 (d). The five detected lines are shown in red in Figure 4.17 (a). Every line (including the shortest lines) has been accurately reconstructed by the proposed iterative Radon transform.





**Figure 4.17 Centerline detection using the iterative Radon transform: (a) input image with five lines with different lengths, the red lines are the detected centerlines using the developed iterative Radon transform; (b) the Radon transform of (a); (c) the Radon transform of (a) with the longest line being removed (iteration 2); and (d) the Radon transform of (a) with the longest three lines being removed (iteration 4).**

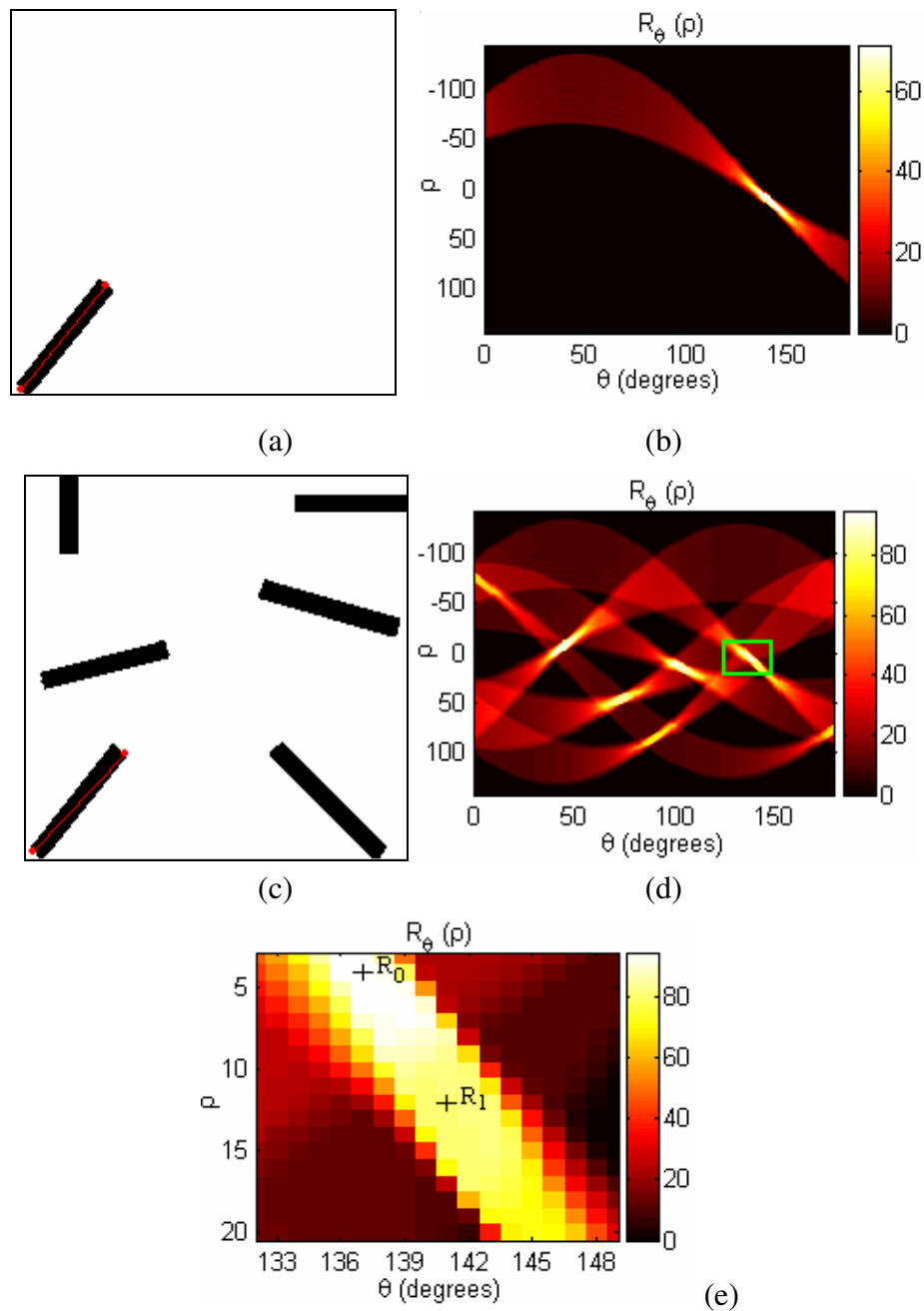
Experiments have shown that the success of an iterative Radon transform relies on the accurate estimation of the line width. If the line width is overestimated, any smaller lines connected to the longer lines will shrink due to the fact that the pixels close to the longer lines will be removed. If the line width is underestimated, many false lines will

be detected from a single line. The line width estimation method proposed in the previous section is applied and the results are robust and accurate.

The iterative Radon transform has also been applied to a number of real images. Two of these results can be found in Figure 4.15 and Figure 4.16.

## 4.5 Localization of the Radon Transform

In a global Radon transform, the interactions between different lines during the radon integration will create false peaks. These peaks do not correspond to any real lines which impedes the estimation of the correct line parameters of a given line. Figure 4.18 illustrates this problem. For the input image with a single line (Figure 4.18 (a)), it is simple to find the correct radon peak in the Radon transform (Figure 4.18 (b)) in order to accurately reconstruct the centerline (red line in Figure 4.18 (a)). If the input image has five other lines (Figure 4.18 (c)) and a global Radon transform is used, we will have six radon peak regions corresponding to the six lines (Figure 4.18 (d)). However, we will never locate the correct peak element for the lower-left line, the same line shown in Figure 4.18 (a). Figure 4.18 (e) is a zoomed-in version of the corresponding peak region (green rectangle in Figure 4.18 (d)). The peak element found in the global Radon transform is marked as “ $R_0$ ”, while the true peak element should be “ $R_1$ ”. The centerline reconstructed from “ $R_0$ ”, the red line in Figure 4.18 (c), is obviously biased because the peak region is affected by two of the other lines (the upper-right and the middle-right lines).



**Figure 4.18 Local Radon transform vs. global Radon transform: (a) the input image with a single line and the detected centerline (red); (b) the Radon transform of (a); (c) the input image with six lines and the detected centerline (red) of the lower-left line; (d) the Radon transform of (c); (e) the peak region in (d) which corresponds to the lower-left line in (c).  $R_0$  is the peak element we are able to find while the  $R_1$  is the true location.**

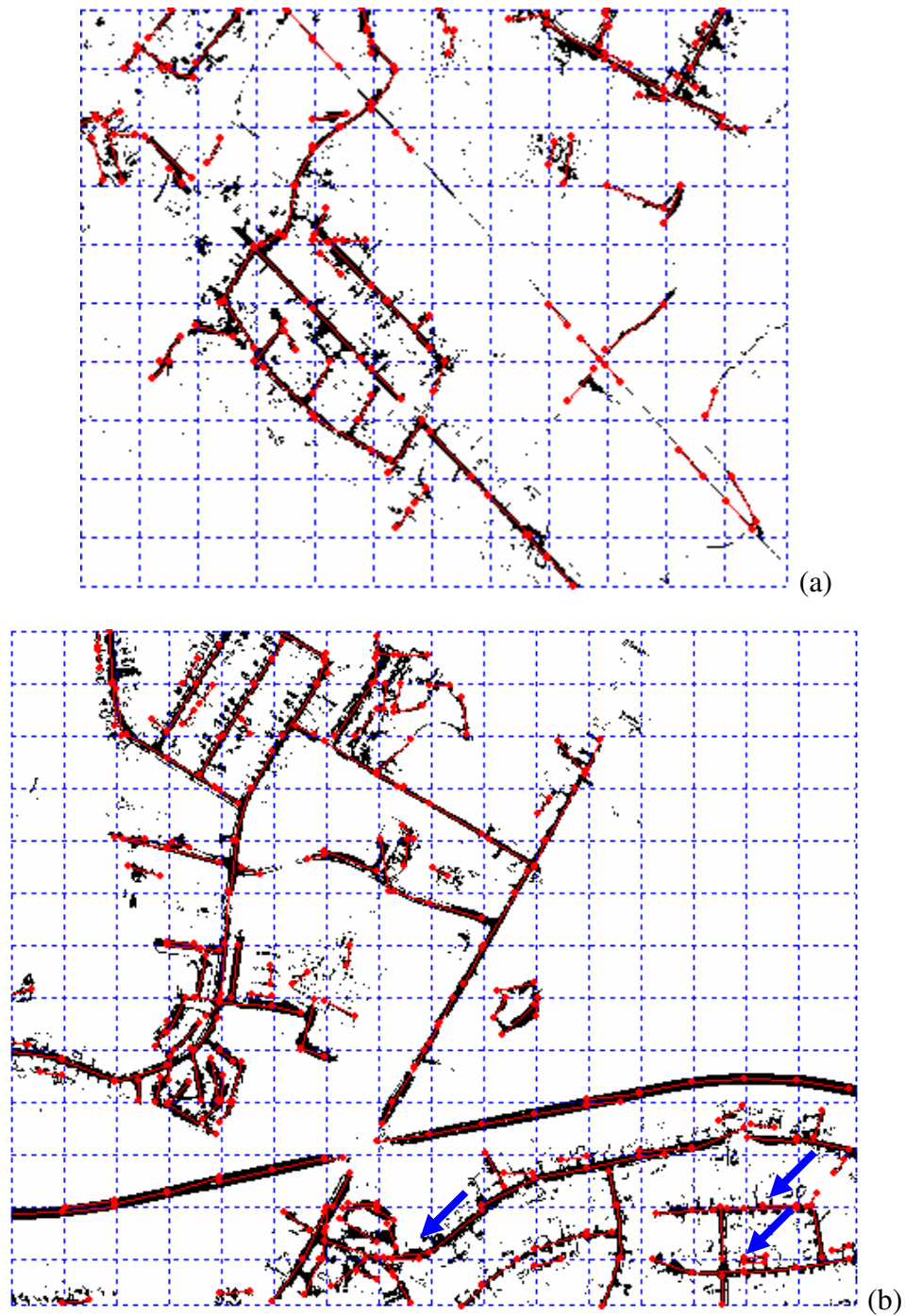
This example demonstrates that the Radon transform-based line detectors work well on an image with a single line. For an image with many lines, the input image needs to be subset into a set of smaller images where each image contains a single line. This is the principle behind the localized Radon transform. In reality, the situation is more complicated because we will never have a simple image as shown in Figure 4.18 (c), which is easily subset into six smaller images with a single line on each image. For a real image, we have to find an appropriate approach to partition the input image in order to localize the Radon transform. In this research, three approaches to localize the Radon transform have been developed and tested. They will be discussed in the following sections.

#### **4.5.1 The gliding-box approach**

In a gliding-box approach, a moving window is defined and the Radon transform is performed locally within the window. The partition of the input image is achieved directly by the window size and step size. There is no requirement to pre-process the input image and this saves computational time.

Figure 4.19 is the output of the road centerline extraction using the gliding-box approach on two of our test images. The black pixels are the refined classified road pixels. The dashed blue rectangles are the gliding boxes, which have a size of 32 by 32 pixels. The step size is set to 32 pixels to ensure there is no overlapping or gaps. The road centerline segments extracted from the adjacent subset images can be linked in the road network formation step. The detected road centerlines are shown in red in Figure 4.19.

As can be seen in Figure 4.20, the localized Radon transform is able to accurately and completely locate the centerlines. Long lines are extracted from a series of short centerline segments, which can be linked into a single long line in the road network formation step. Curvilinear roads are approximated by a set of short road centerline segments. This is an important feature of the road network extraction system as accurately extracting curvilinear roads is always a difficult task.



**Figure 4.19** Road centerline extraction from classified imagery using iterative and localized Radon transform based on gliding-box approach. (a) Ikonos test image; (b) Quickbird test image. Dashed blue lines indicate the gliding boxes and the red lines are the extracted road centerlines.

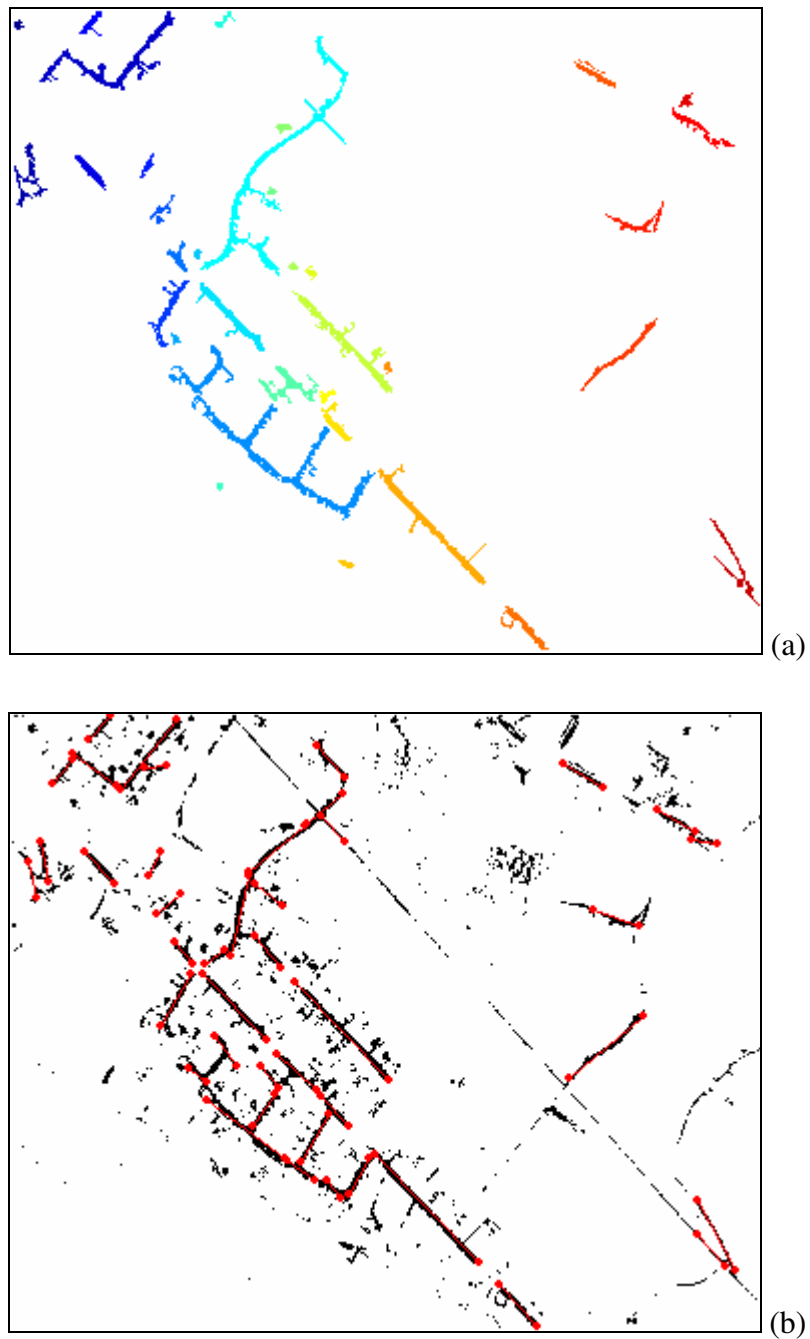
There is a problem associated with the gliding-box approach. If a road line runs vertically or horizontally and lies close to the boundary area between two neighboring gliding-boxes, erroneous centerlines will be created. Three examples can be found in Figure 4.19 (b). The blue arrows indicate the positions where two parallel centerlines have been extracted. However, there should only be a single centerline. This problem is created by the artificial boundaries used by the gliding-boxes.

#### **4.5.2 The connected component analysis approach**

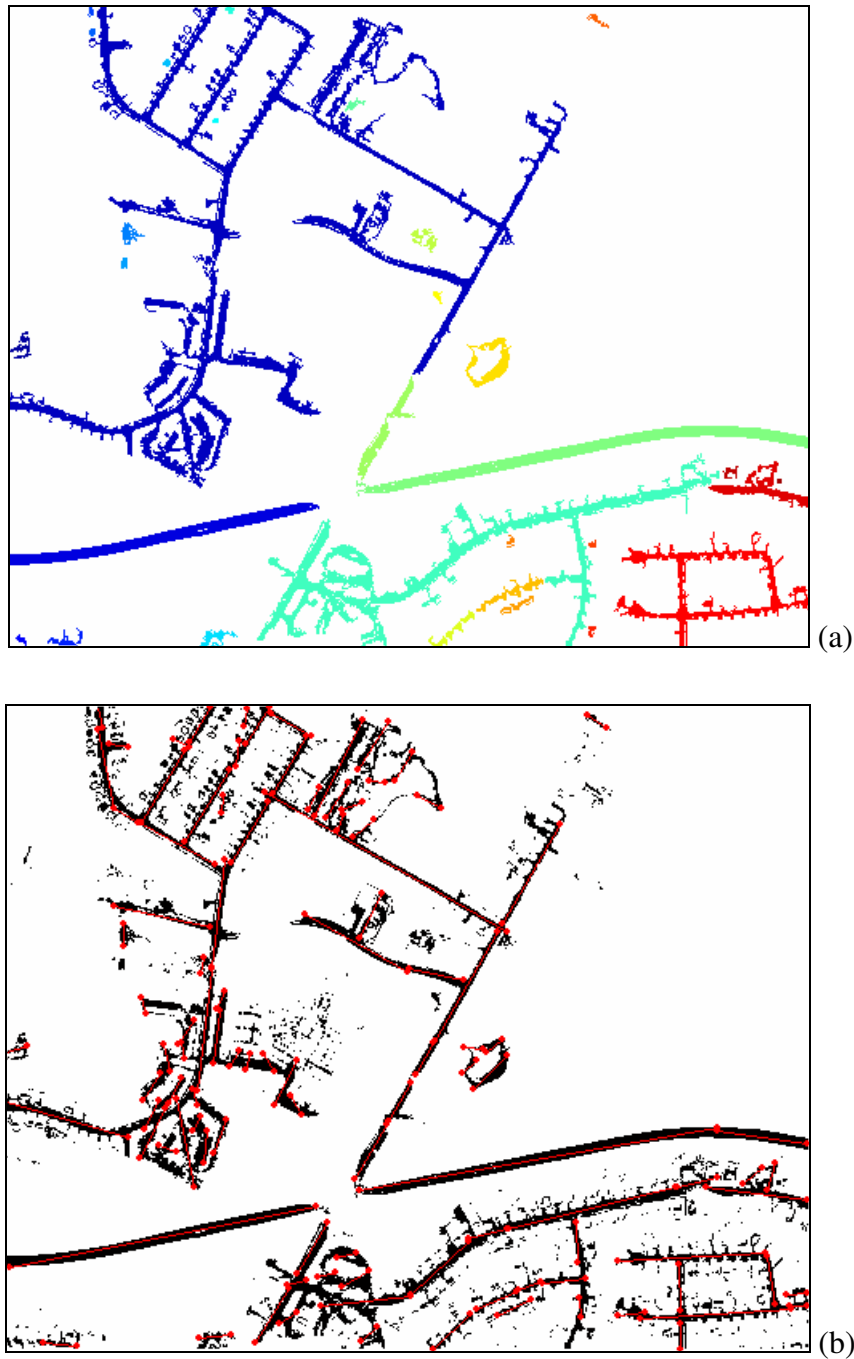
In this approach, the connected components need to be found in the classified image so that the Radon transform can be separately applied on each connected component. In this research, the region growing algorithm is used for the connected component analysis. Region growing is a region-based image segmentation technique, which can find the connected regions based on seed points and a set of growing criteria [Gonzalez and Woods, 2002].

The seed points were selected based on a local neighborhood analysis. If a road pixel is surrounded by 8 road pixels in its 3 by 3 neighborhood, it is selected as a seed pixel. Figure 4.20 and Figure 4.21 show the road centerline extraction outputs using the connected component analysis technique to localize the Radon transform. The technique was applied to the same test images as in Figure 4.19. The different colors in Figure 4.20 (a) and Figure 4.21 (a) are showing different road component images grouped by the region growing algorithm. The road centerlines are extracted from each road component image using the iterative Radon transform.

From Figure 4.20 and Figure 4.21, we can see that this approach generally gives longer lines than the gliding-box approach. This is an advantage if the road is straight. However, it is a disadvantage for a curvilinear line as it will straighten the line and enlarge the discrepancy between the real centerline and the extracted line. In addition, if a very large connected component exists in the image, the localization of the Radon transform will not be complete and might cause erroneous extractions. The technique also fails to extract any road centerlines from very small road components.



**Figure 4.20** Road centerline extraction from the classified Ikonos test image using an iterative and localized Radon transform based on a region growing approach. (a) road component images (differentiated by color) found by the region growing algorithm; (b) extracted road centerlines (red).



**Figure 4.21** Road centerline extraction from the classified Quickbird test image using an iterative and localized Radon transform based on a region growing approach. (a) road component images (differentiated by color) found by the region growing algorithm; (b) extracted road centerlines (red).

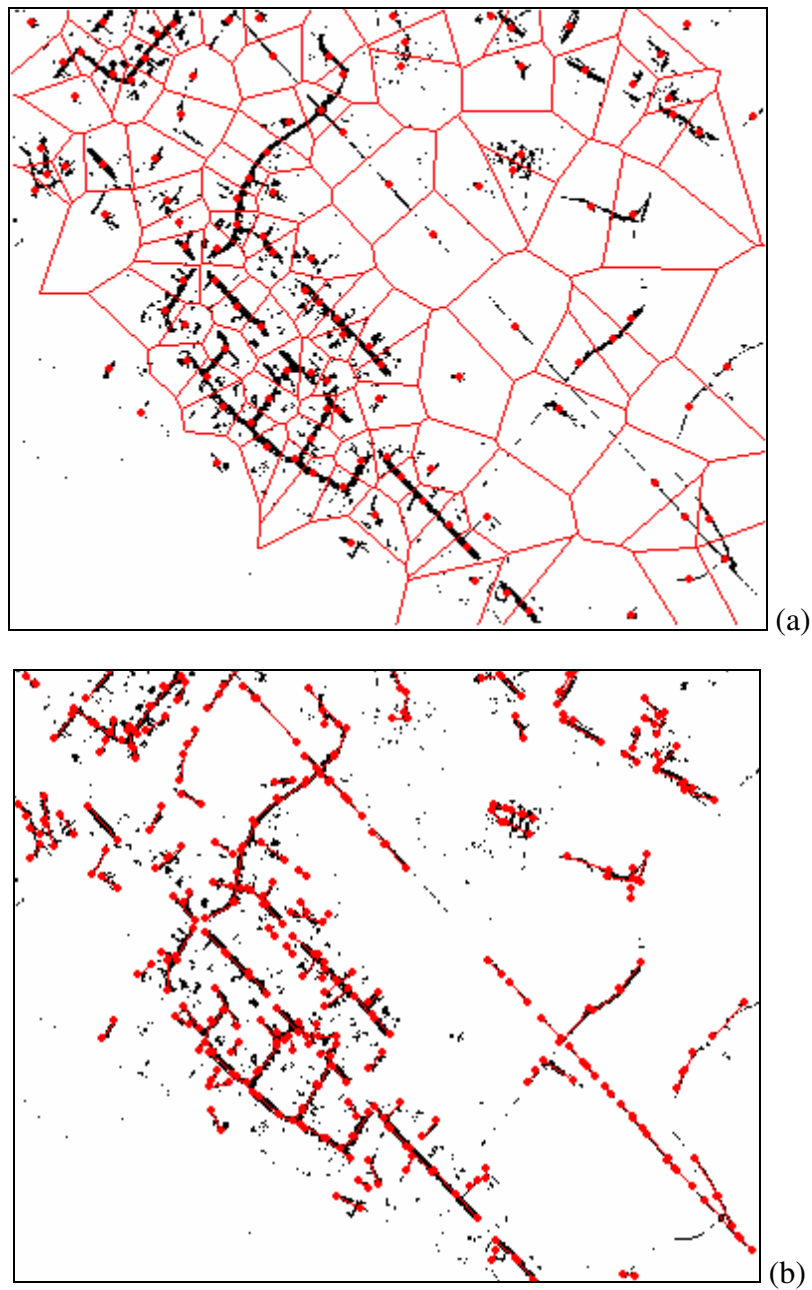


### 4.5.3 The spatial clustering approach

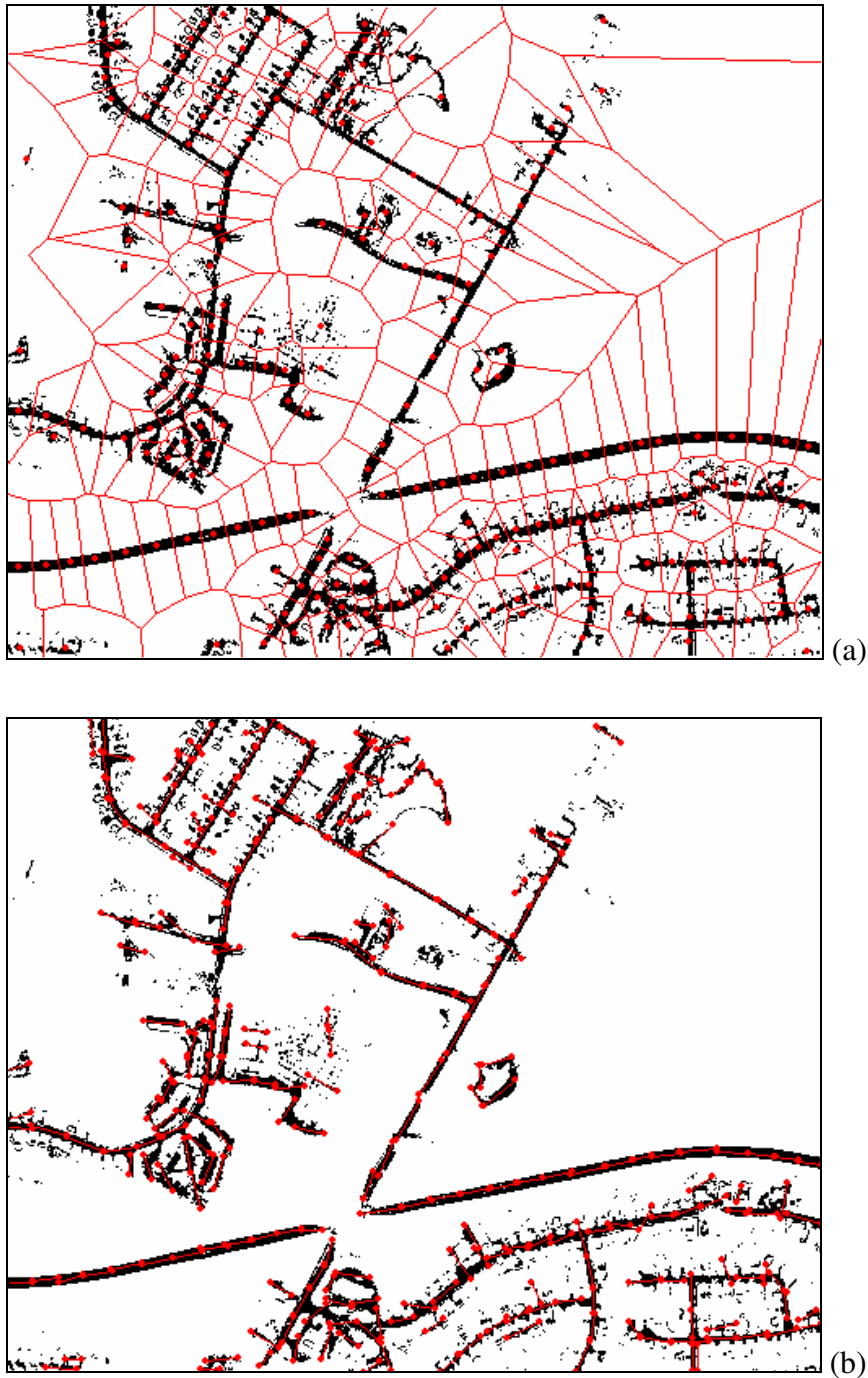
A spatial clustering algorithm can be also applied to the road pixels in order to partition the input road image into a series of meaningful subset images (called road component images). The Radon transform will be then applied locally to the subset images.

Theoretically, any spatial clustering algorithm can be used to divide the input image. However, there is a tradeoff between the computational efficiency and the clustering quality. In this research, a special version of the  $k$ -medoids algorithm is applied. The  $k$ -medoids method is a partitioning-based clustering method. Since it uses the most centrally located object (*medoid*) in a cluster as the cluster centre instead of taking the mean value of the objects in a cluster, it is less sensitive to noise and outliers as compared with the  $k$ -means approach [Han *et al.*, 2001]. Therefore, the  $k$ -medoids method is more suitable for spatial clustering than the  $k$ -means method because of its improved clustering quality. However, it is well known that a  $k$ -medoids method is very time-consuming. To overcome the computational issue of existing  $k$ -medoids methods, a new  $k$ -medoids algorithm called Clustering Large Applications with Triangular Irregular Networks (CLATIN) has been introduced by Zhang and Couloigner (2005). The CLATIN algorithm is more efficient than the basic  $k$ -medoids algorithm while retaining the same clustering quality.

Figure 4.22 (a) and Figure 4.23 (a) are the outputs of the CLATIN algorithm on the classified road pixels. The Voronoi tessellation (red lines) based on the final medoids produces a continuous partition of the entire image. Each component has a small portion of the road pixels from which a Radon transform can be applied and possible road segments can be found. Figure 4.22 (b) and Figure 4.23 (b) depict the extracted road centerlines based on the CLATIN approach.



**Figure 4.22 Road centerline extraction from the classified Ikonos test image using an iterative and localized Radon transform based on the CLATIN spatial clustering approach. (a) output of the CLATIN algorithm: black pixels – road pixels, red points – final medoids, red lines – Voronoi tessellation of the final medoids; (b) extracted road centerlines (red).**



**Figure 4.23** Road centerline extraction from the classified Quickbird test image using an iterative and localized Radon transform based on the CLATIN spatial clustering approach. (a) output of the CLATIN algorithm: black pixels – road pixels, red points – final medoids, red lines – Voronoi tessellation of the final medoids; (b) extracted road centerlines (red).

Compared to the gliding-box algorithm used by Du and Yeo (2004), the CLATIN algorithm provides a more meaningful partition of the input space because it takes into consideration the spatial distribution of the road pixels. The partition of the road pixels by CLATIN is continuous and has no overlapping areas. This makes it easier to group the road segments in order to form a long line, even curvilinear line.

The main disadvantage of this approach is that there is no efficient spatial clustering algorithm available in the computer science community. The number of road pixels in the classified image is usually very large and this creates a fatal computational issue.

#### 4.5.4 Comparison between different localization approaches

The qualitative comparison of the three localization approaches is summarized in Table 4.8, where CCA means connected-component analysis. These comparisons are based on visual observation.

**Table 4.8 Comparison of different localization approaches**

	<b>Gliding-box</b>	<b>CCA</b>	<b>CLATIN</b>
<b>positional accuracy</b>	high	low	high
<b>long straight line</b>	well	better	well
<b>curvilinear line</b>	well	problem	well
<b>short lines</b>	well	problem	well
<b>computational load</b>	low	medium	high
<b>network structure</b>	good	problem	good

The quantitative assessment of the final extracted road networks using the three approaches is performed against a reference dataset based on a line segment matching algorithm presented in Chapter 6. Three quality measures have been used: the *completeness* to indicate the ability of the road extraction methods to extract the entire

road network; the *correctness* to represent the percentage of correctly extracted road data with respect to the total extracted road data; and the *Root Mean Square Error (RMSE)* to indicate the potential geometrical accuracy of the extracted road data. Table 4.9 provides an overview of the assessment results. Two sets of multi-spectral (MS) images have been used: Ikonos MS (4 m spatial resolution) and Quickbird MS (2.4 m spatial resolution). Both sets have three test images. The quality measures shown in Table 4.9 are the average values from the three test images.

**Table 4.9 Quality assessment of the extracted road networks using different localization approaches**

Test Image	Method	Completeness	Correctness	RMSE (Pixels)
Ikonos MS	Gliding-box	0.49	0.37	0.90
	CCA	0.51	0.29	1.10
	CLATIN	0.48	0.41	0.84
Quickbird MS	Gliding-box	0.50	0.49	1.07
	CCA	0.49	0.46	1.21
	CLATIN	0.48	0.51	1.12

As we can see from Table 4.9, all three approaches are performing similarly. The CLATIN has a relatively higher correctness rate and positional accuracy. The connected component analysis (CCA) has a relatively higher completeness rate but a lower correctness rate and positional accuracy. These differences can be visually perceived from their outputs. The gliding-box approach achieves a comparable quality with a lower computational load, which is suitable to localize the Radon transform where computational load is an issue.

## 4.6 Summary

The Radon transform has a number of advantages for linear feature detection including its ability to detect line widths and its robustness to noise. However, the quality of the Radon transform-based linear feature detection has to be improved for road network extraction from classified imagery.

In this research, the peak selection problem in the Radon transform-based line detector has been investigated. A mean filter was proposed to locate the true peak in the radon image and a profile analysis technique was used to further refine the line parameters to reduce the biased radon peak issues. The  $\theta$ -boundary problem of the Radon transform was also discussed and the erroneous line parameters were corrected. Finally, a robust approach was developed to locate the Radon peak region for wide lines. Experiments have shown that the proposed methodology provides an accurate and robust estimation of the line parameters and a solution to the peak selection issue of the Radon transform-based linear feature detector.

An iterative and localized Radon transform has been developed for the specific application of road network extraction from classified imagery. The iterative Radon transform was able to detect both long and short lines based on an accurate estimation of the line width and line parameters in the radon space. The localization of the Radon transform was achieved by using three algorithms: the Gliding-box; the Connect Component analysis; and the Spatial Clustering approach. These techniques were applied to the classified and refined road pixels. The localized Radon transform made it possible to detect small road segments and long curvilinear lines. The three localization methods have been compared and the Gliding-box approach is suggested for applications where computational load is of concern.

The extracted road centerline segments will be further grouped, in the next chapter, to form a road network.

## CHAPTER 5

# ROAD NETWORK FORMATION

Road network formation enables the linking of individual road segments into meaningful road lines and the building of the network topological structure such that the data is GIS-ready. Generally, it includes tasks such as bridging gaps between road segments, creating nodes for road intersections, and removing overshooting or undershooting.

The Gestalt psychologists have defined perceptual grouping (or perceptual organization) as an ability to explore a structuralized feature organization from sensory data. It allows the formation of object hypotheses with minimal domain knowledge [Crevin, 1999]. It has four levels: signal, primitive, structure, and assembly [Boyer and Sarkar, 1999].

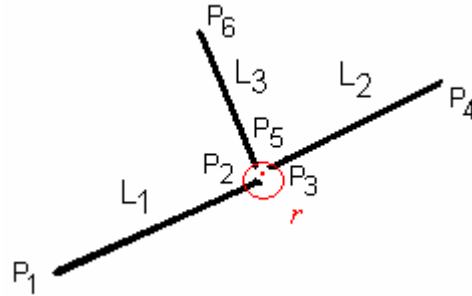
The Gestalt psychologists have discovered a set of important properties in perceptual organization: proximity, continuity, similarity, closure, and symmetry. These properties are useful in grouping the detected edges or detected road centerlines into a road network. Thus, perceptual grouping has been widely used in road network extraction from remotely-sensed imagery (e.g., Crevin, 1999; Hu and Tao, 2002).

In this research, we will apply the basic idea of perceptual organization to the grouping of road centerline segments into a road network.

### **5.1 Endpoint Fusion**

Due to the use of a localized Radon transform in our road centerline extraction, there are many disconnected road segments belonging to the same road line. The gaps between these disconnected road segments are usually very small (i.e. in the order of 1-3 pixels). This step allows us to examine all of the endpoints of the extracted road segments and find out which endpoints are close to each other, e.g. within an Euclidean distance of 5 pixels. Endpoints within this threshold distance are joined

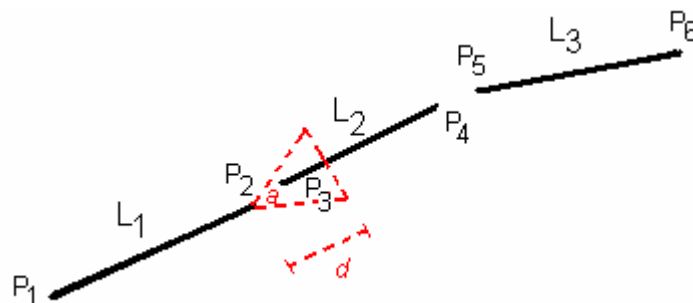
together by averaging their coordinates, thus creating one position (Figure 5.1). In Figure 5.1, three line segments are shown. The endpoints  $P_2$ ,  $P_3$ , and  $P_5$  are determined to be close to each other and are joined together into a single point (the red point).



**Figure 5.1 Endpoint fusion**

## 5.2 Gap Bridging

Gap bridging is one of the main concerns in road network formation. Gaps might occur in the extracted road network for many different reasons. A gap may occur if a building or a line of trees occludes a road, or when changes in road pavement materials cause the algorithm to incorrectly identify some small road segments.



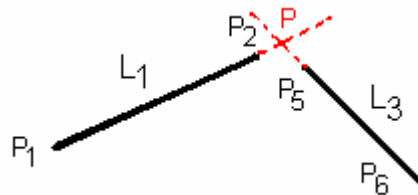
**Figure 5.2 Gaps bridging**



A collinear test is usually used for gap bridging. Figure 5.2 illustrates the method we used in the research. A triangle zone (height  $d$  and angle  $a$ ) is built at the endpoint  $P_2$  of the line segment  $L_1$ . If there is an endpoint from another line segment (e.g.  $L_2$ ) within this triangle zone and if the two line segments have a similar orientation, the gap between  $P_2$  and  $P_3$  will be bridged. A new endpoint  $P$  will be then created at the average location of these two endpoints. These two line segments will be then linked into one polyline.

### 5.3 Creation of Road Intersections

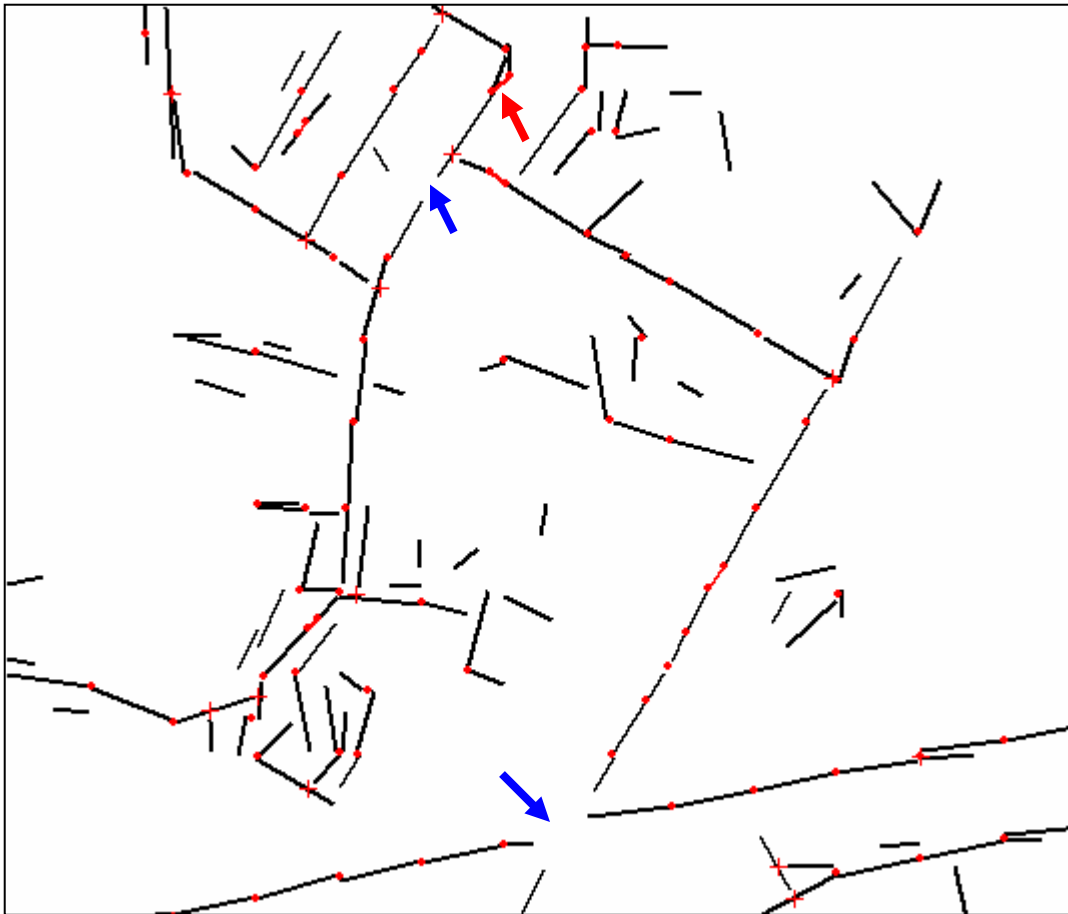
Road intersection can be created in two ways: (1) create the direct intersection point of two intersecting line segments and then divide the two line segments into four segments; and (2) create the possible road intersection by extending two line segments. The latter case removes possible problems with undershooting.



**Figure 5.3 Road intersections creation**

The two line segments  $L_1$  and  $L_3$  shown in Figure 5.3 do not have a direct intersection point. However, by extending the two line segments, we create the intersection point  $P$ . Figure 5.4 gives the output of our grouping of the road segments from the Quickbird test image presented in Figure 2.2. The road centerline segments (black lines) were extracted using the iterative and localized Radon transform based on the gliding-box approach. From Figure 5.4, we can see that the endpoint fusion of small gaps (red points) and the creation of the road nodes (red crosses) is quite successful. However, the bridging of big gaps (red lines) has some problems (e.g., the one at the upper centre indicated by the red arrow). Many large gaps still remain in the extracted road

network (indicated by the blue arrows). These gaps are not bridged during the grouping process since they fall outside the threshold values. The hierarchical perceptual grouping strategy used by Hu and Tao (2002) is expected to help reduce this issue.



**Figure 5.4 Road segments grouping: red points - fused small gaps, red lines - bridged big gaps, red crosses - created road nodes.**

## **5.4 Topological Structure Building**

In order to input the extracted road networks into a GIS, explicit topological relationships are usually required. In this research, both road polylines and road nodes

are defined along with their topological information (see Table 5.1, Table 5.2 and Table 5.3).

**Table 5.1 Road polyline attributes.**

<b>No</b>	<b>Attribute Name</b>	<b>Type(Length)</b>	<b>Description</b>
<b>1</b>	PolylineID	Int(6)	Unique identity of the road
<b>2</b>	FromNodeID	Int(6)	The node ID of from-node
<b>3</b>	ToNodeID	Int(6)	The node ID of to-node
<b>4</b>	VertexNum	Int(4)	The number of the inner vertices
<b>5</b>	VertexIDList	IntPtreter(Var)	The list of the vertices ID
<b>6</b>	...		

**Table 5.2 Road node attributes.**

<b>No</b>	<b>Attribute Name</b>	<b>Type(Length)</b>	<b>Description</b>
<b>1</b>	NodeID	Int(6)	Unique identity of the node
<b>2</b>	X	Dbl(12.3)	The X coordinate of the node
<b>3</b>	Y	Dbl(12.3)	The Y coordinate of the node
<b>4</b>	Z	Dbl(12.3)	The Z coordinate of the node
<b>5</b>	InPolylineNum	Int(4)	# polylines linked towards the node
<b>6</b>	OutPolylineNum	Int(4)	# polylines linked outwards from the node
<b>7</b>	PolylineIDList	IntPtreter(Var)	The ID list of the linked polylines
<b>8</b>	...		

**Table 5.3 Road vertex attributes.**

No	Attribute Name	Type(Length)	Description
1	VertexID	Int(6)	Unique identity of the vertex
2	X	Dbl(12.3)	The X coordinate of the node
3	Y	Dbl(12.3)	The Y coordinate of the node
4	Z	Dbl(12.3)	The Z coordinate of the node
5	...		

Assuming that each road segment is represented by two points,  $P_1$  and  $P_2$ , with an orientation given by the direction from  $P_1$  to  $P_2$ , the basic steps in building topological structures from road segments are as follows:

- 1) Create two initial road node records from the endpoints of the first road segment with  $InPolylineNum=0$  and  $OutPolylineNum=1$  for the first end point,  $InPolylineNum=1$  and  $OutPolylineNum=0$  for the second end point;
- 2) Create a new road polyline record from the first road segment with a unique  $PolylineID$  and relevant  $FromNodeID/ToNodeID$  information from Step 1.
- 3) For all of the remaining road segments:
  - a. create a new road polyline record with a unique  $PolylineID$
  - b. check both endpoints ( $P_1, P_2$ ):
    - i. If  $P_1$  is in the road node table, update the corresponding  $OutPolylineNum$  and  $PolylineIDList$ ; else create a new road node record.
    - ii. If  $P_2$  is in the road node table, update the corresponding  $InPolylineNum$  and  $PolylineIDList$ ; else create a new road node record.

- c. Update the new road polyline record with proper *FromNodeID* and *ToNodeID* from Step b.
- 4) In the road node table, start from a road node whose linked polyline number is not equal to two. The number of linked polylines is also called the degree of the road node. If a road node has a degree of two, it is a false road node or an inner vertex, which should be removed from the road node table. We start the topological relationship building from a real road node. We name this road node as the current road node (*CurNode*). For each linked polyline (*CurLinkedPolyline*) of the current road node:
- a. If *CurLinkedPolyline* has not been processed, assign the current road polyline (*CurPolyline*) to *CurLinkedPolyline* and assign the search polyline (*SearchPolyline*) to *CurPolyline*.
  - b. Assign the search road node (*SearchNode*) to the other end point of the *SearchPolyline*:
    - i. If the *SearchNode* has a degree of two, update the *CurPolyline* by adding a vertex to its vertex list, change the *SearchPolyline* to the other linked polyline of the *SearchNode* (it has only two linked polylines because its degree is two). Change the *SearchNode* to the other end point of the new *SearchPolyline*.
    - ii. Repeat Step i until the degree of the *SearchNode* is not equal to two, i.e. a real road node is encountered. The current road polyline is then finished.
  - c. Move to the next linked road polyline of the current road node. Repeat Step a and b until all of the linked road polylines of the current road node have been processed.
  - d. Move to the next road node and repeat Step 4 until all road nodes have been processed.

## 5.5 Road Network Cleaning

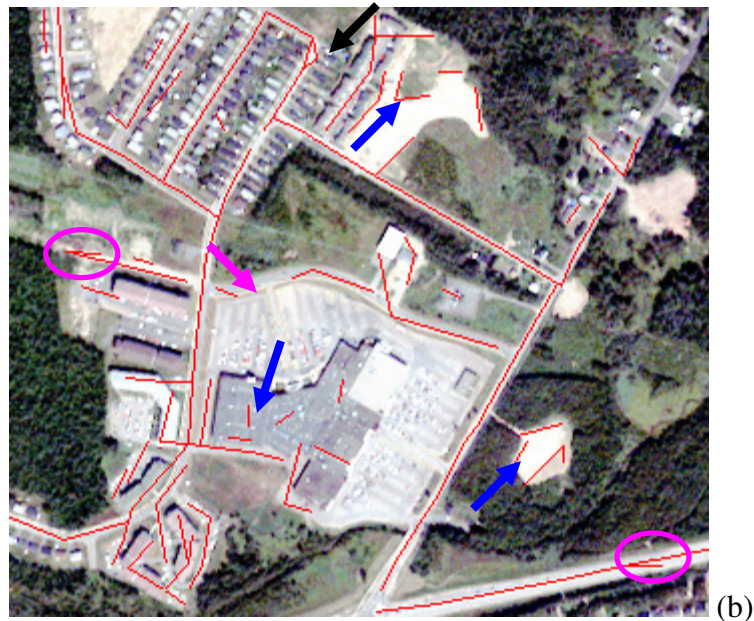
The road network cleaning step removes the short road lines which are not connected with other lines, i.e., segments that are most likely isolated lines, not roads. Overshooting can be also handled in this step because the topological information for all road lines is available. Figure 5.5 and Figure 5.6 show the final outputs from our road network formation steps.

In Figure 5.5, the road centerline segments were extracted using the iterative and localized Radon transform based on the gliding-box approach from the Ikonos test image presented in Figure 2.1. The main roads have been successfully extracted except for the road running from the lower right to the upper left, for which a large portion is missing (indicated by the magenta arrows) due to the problem associated with the road refinement algorithm (see Figure 3.7). False road lines were extracted where the spectrally similar open areas have not been completely removed (indicated by the blue arrows).



**Figure 5.5** Road network formation based on the extracted road centerline segments from the Ikonos MS test image presented in Figure 2.1.

Figure 5.6 gives the output from the road network formation based on the extracted road centerline segments (red lines) from the Quickbird test image presented in Figure 2.2. The road centerline segments were extracted using the iterative and localized Radon transform based on the gliding-box approach. The extracted road network is generally complete and accurate. Incompleteness is visible at major road intersections and in the vicinity of parking lots or crop fields where the road refinement step encountered some difficulties (indicated by the magenta arrows). False extractions are mainly located on spectrally similar objects such as parking lots and buildings, which have not been removed as non-roads (indicated by the blue arrows).

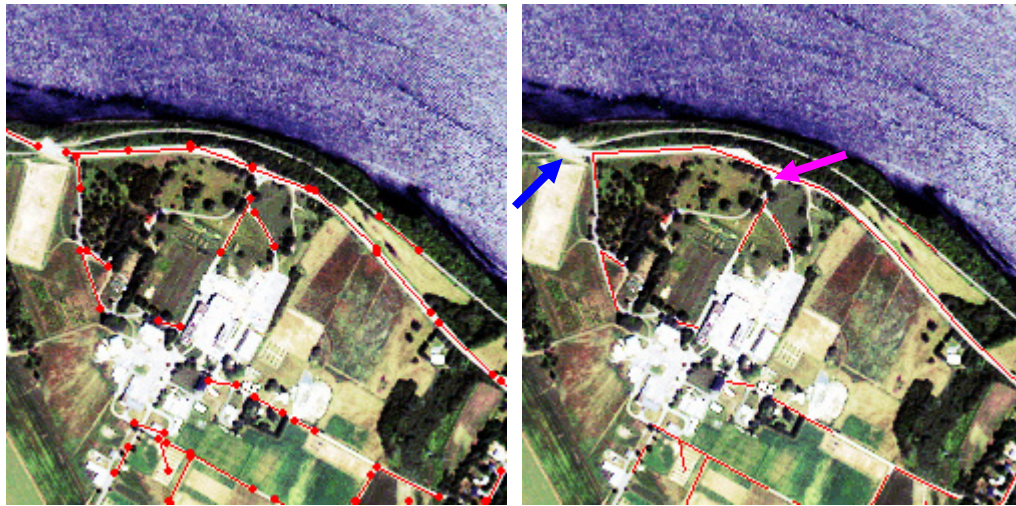


**Figure 5.6 Road network formation based on the extracted road centerline segments from the Quickbird MS test image presented in Figure 2.2.**

Although the overall quality of the road network formation is satisfactory given the road centerline segments extracted by the iterative and localized Radon transform, some erroneous lines have been created during the road network formation step (see the line indicated by the black arrow in Figure 5.6). In addition, the road network

cleaning step fails to remove the short lines that are located close to a real road line but at a very sharp angle. Two examples are shown within the magenta circles in Figure 5.6.

Figure 5.7 (a) shows the extracted road centerline segments (red lines) from the Ikonos test image presented in Figure 2.4. The road centerline segments were extracted using the iterative and localized Radon transform based on the gliding-box approach. Figure 5.7 (b) depicts the final road networks resulting from the road network formation. The major structure of the extracted road network is well established and topologically correct. The long curvilinear road running from the lower right to the upper left is almost completely extracted with only one small portion missing due to the road classification problem (indicated by the blue arrow). Three of the four road intersections have been successfully created. The failed intersection is due to the problem of occlusion by trees (indicated by the magenta arrow)), which caused the error in road classification.



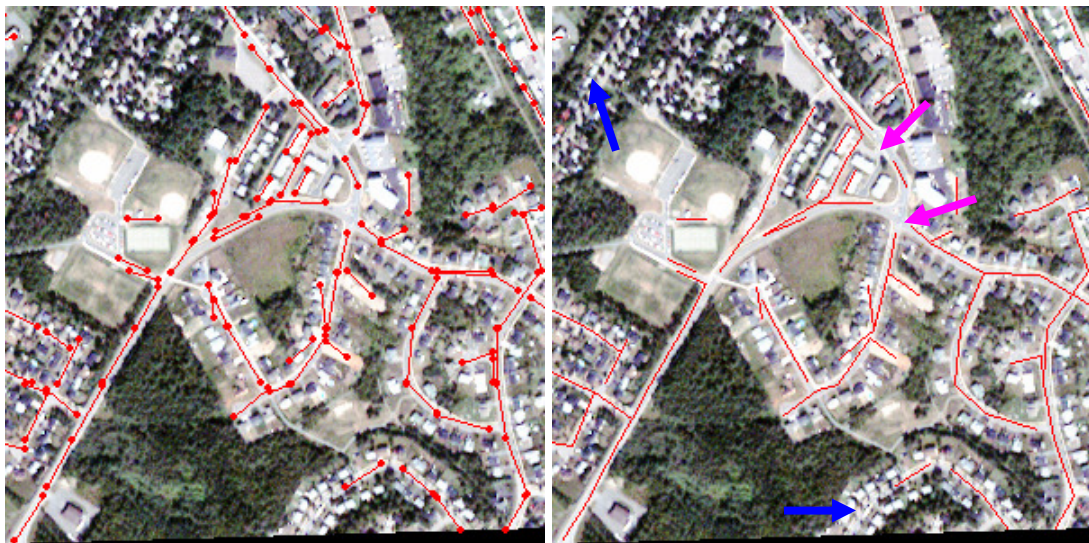
(a)

(b)

**Figure 5.7 Road network formation: (a) the extracted road centerline segments from the Ikonos MS test image presented in Figure 2.4; (b) the final road network.**



Figure 5.8 (a) shows the extracted road centerline segments (red lines) from the Quickbird test image presented in Figure 2.5. The road centerline segments were extracted using the iterative and localized Radon transform based on the gliding-box approach. As with the Ikonos MS imagery, incompleteness in the final road networks resulting from the road network formation shown in Figure 5.8 (b) mainly occurs at the road intersections (indicated by the magenta arrows) or within densely residential areas (indicated by the blue arrows).



(a)

(b)

**Figure 5.8 Road network formation: (a) the extracted road centerline segments from the Quickbird MS test image presented in Figure 2.5; (b) the final road network.**

## 5.6 Summary

Road network formation from individual road segments is important since it affects the quality measures of the extracted road network, particularly the network properties. Bridging the gaps, likely due to misclassification, is an important task and can improve the completeness of the extracted road network. It is also possible to remove

certain false extractions after the road network formation step by examining the geometrical or topological properties of the extracted road polylines. This will improve the correctness of the extraction. Finally, road network formation is required to be able to input the extracted road network into a GIS and thus be able to update an existing GIS database.

Based on the analysis, our current road network formation is relatively weak. There are still problems in removing the erroneous road polylines in the grouping stage. Further work will be required to improve the results.

# CHAPTER 6

## QUALITY ASSESSMENT

### 6.1 Introduction

Although quality assessment is an important and necessary step for automated road network extraction from imagery, relatively little work has been carried out in this area [Hinz *et al.*, 2002; Wiedemann, 2003].

As previously presented in Chapter 1, Couloigner and Ranchin (1998), Wiedemann (2002, 2003) and Péteri *et al.* (2004) provided different sets of quantitative criteria for both planimetric accuracy evaluation and spatial characterization of the extracted road network against a reference network.

The main problem with the quality assessment of an extracted road network lies in the lack of positional accuracy measures for linear features. Hausdorff distance [Hangouet, 1995] and Buffering-based distance [Goodchild and Hunter, 1997; Walter and Fritsch, 1999] measures suffer from a heavy computational issue.  $L_2$ -distance [Saalfeld, 1988; Saalfeld, 1993] and Linear Mapping-based measures [Fillin and Doysther, 1999, 2000] rely on the matching of vertices. If the matching fails, the calculated distance is distorted.

Another problem lies in the inability to automatically locate all conjugate road lines from two versions of a road network - extracted versus reference. This is usually performed manually, which is very time consuming. Based on some similarity measures, including distance measures, we can automate the matching to some degree and save time in assessing the quality of the extracted road network.

In this research, a distance measure for line segments is proposed and a matching strategy is designed to locate the matched portion of two conjugate line segments. Quality evaluation is then carried out based on the distance measure and the matching results using the criteria proposed by Wiedemann (2002, 2003)

The remaining sections of this chapter are organized as follows: Section 6.2 introduces quality assessment for automated road extraction and describes three basic quality measures; Section 6.3 details the feature matching problems; Sections 6.4 and 6.5 discuss the application of the proposed methodology to the evaluation of the road network extraction; Section 6.6 provides some conclusions; and Section 6.7 summarizes the chapter.

## 6.2 Quality Measures for Road Extraction

A common method for evaluating extracted roads is to use a reference road map, which is assumed to be more accurate and more complete. The reference road map can be an existing up-to-date digital road map or a road map created by photo-interpretation from the same image (see [Péteri and Ranchin, 2002; Péteri *et al.*, 2004] for how to establish an accurate reference map from photo interpretation).

A typical situation is illustrated in Figure 6.1. In (a), the red lines are the reference road lines overlaying the source image, and in (b), the red lines are the extracted road lines. The reference road lines are derived from an existing road map verified and updated using GPS data. The image used in the road network extraction is a subset of a high spatial resolution (2.4 m) multi-spectral Quickbird image. The roads are extracted using the proposed methodology described in Chapters 2 to 5.

A visual comparison of the extracted roads with the reference roads in Figure 6.1 shows that most have been successfully and accurately extracted. However, we do not know the number of:

- 1) Missed roads (part of the road at the upper-right corner of the input image is missing);
- 2) Missed road intersections (the major road intersection at the lower-center of the input image has not been extracted);
- 3) False roads (some extracted roads are not roads); and
- 4) Shifted roads (the positional accuracy of some roads is low).





**Figure 6.1** Evaluation of automated road extraction: (a) the RGB composite of the source image overlaid with the reference roads (red lines); (b) the extracted roads (red lines)

Before applying our automated road network extraction to a production environment, quantitative assessment of the results is necessary. In the existing literature, three basic quality measures have been used to evaluate extracted road networks. They are *Completeness*, *Correctness*, and *RMSE*. Following the notations and definitions used in [Wiedemann, 2003], the following sections describe the three basic quality measures.

### 6.2.1 Completeness

The completeness is the ratio of the reference road data matched with the extracted road data to the total length of the reference road network (Eq. 6.1). It indicates the ability of the road network extraction methods to extract the road network from an image. The completeness has a range of [0, 1]. A higher completeness value means less roads missed or less errors of omission.

$$Completeness = \frac{\text{length of matched reference}}{\text{length of reference}} \quad (6.1)$$

### 6.2.2 Correctness

The correctness is the ratio of the extracted road data matched with the reference road data to the total length of the extracted road network (Eq. 6.2). The correctness also has a range of [0, 1]. The lower the value, the higher the false alarm rate of the results or the higher the errors of commission, i.e., more false roads have been extracted.

$$Correctness = \frac{\text{length of matched extraction}}{\text{length of extraction}} \quad (6.2)$$

### 6.2.3 RMSE

The RMSE expresses the average distance between the extracted road network and its matched reference. It indicates the geometrical accuracy potential of the extracted road data and is usually calculated using the following equation:

$$RMSE = \sqrt{\frac{\sum_{i=1}^K (d(ext_i; ref))^2}{K}} \quad (6.3)$$

where  $K$  is the number of matched line segments, and  $d(ext_i, ref)$  is the distance between the  $i^{th}$  segment of the extracted line and its corresponding reference line.

Using different computational approaches, these three quality measures have been widely used in evaluating feature extraction from imagery (e.g., [Wessel *et al.*, 2002; Wiedemann, 2003; Hu and Tao, 2005]). The three quality measures depend on the results of the road network matching step. Different matching strategies will certainly have different evaluation results. In the next section, I will discuss how the technique of feature matching can be applied to the quality assessment of automated road network extraction.

### 6.3 Feature Matching for Quality Assessment

Feature matching is one of the most important vision problems as well as one of the most important photogrammetric problems. Feature matching is a technique used to determine the conjugate features between two different versions of a dataset, e.g. to determine the correspondence between two sets of coplanar lines, by finding pairs, among many candidate feature points, that correspond to the same element. Feature matching is also one of the critical steps in map conflation [Cobb *et al.*, 1998].

The matching results are useful for determining the change of a GIS layer [Filin and Doytsher, 2000] or to automate an image registration process [Habib and Al-Ruzouq, 2005]. Feature matching can also be applied to road network extraction, particularly for assessing the extracted road network against a reference road network. There are three basic issues in feature matching: choice of the matching primitives; choice of similarity measures; and choice of matching strategy [Habib and Al-Ruzouq, 2005].

#### 6.3.1 Matching primitives

The selection of the matching primitives is an important issue that affects the matching procedures and the reliability of the matching results. For linear feature matching,

such as the matching of two road networks, we have a choice of using polylines, lines segments, and points.

The ideal matching primitive should be road polylines. This is due to the fact that road polylines and road nodes are vital to build a road network with its topology. A road polyline usually represents a real road and has its own semantic content. It is believed that during visual matching, road networks are typically matched based on road nodes and road polylines rather than road segments or inner vertices. However, matching road polylines relies on a well-defined distance measure of the polylines. Similar to the human visual system, this distance measure should reflect the positional discrepancy between two polylines. It should also be able to encompass the differences of the two polylines in terms of direction, number of inner vertices, etc. The available distance measures for polylines include the Hausdorff distance and the  $L_2$  distance. Both measures are based on the distance between the vertices of two polylines, which means that they are sensitive to the positions of the inner vertices. If the inner vertex has a different structure, the matching will fail and the distance measure will be distorted. Buffering techniques have also been applied to decide whether two polylines are to be matched or not, thus avoiding the calculation of the distance between two polylines (e.g. [Walter and Fritsch, 1999]). A polyline-based matching strategy also depends on the two versions of the road network sharing a similar topological structure in order to ensure the matching rate. Unfortunately, this is a very strict condition in the context of automated road network extraction from imagery. Both the redundant road segments and the missing road segments, which are very common in road network extraction, will damage the topological structure of the entire road network and make polyline-based matching difficult.

In [Wiedemann, 2003], equally spaced auxiliary nodes are inserted along the edges of each network. From each node of a network, the shortest distance to its respective node in the other network is determined along with a consideration of the difference in direction. The matching is based on this distance and all of the quality measures are approximated by this distance.



In this research, a line segment-based matching approach is proposed. The reasons for this selection are:

- 1) Most polyline-based matching approaches eventually rely on operations involving line segments, e.g., buffering a polyline involves calculating buffers for each individual line segment. Therefore, using line segments as the matching primitive does not significantly add computational load to the matching procedure;
- 2) Line segment-based matching is less sensitive to the topological differences between two versions of a road network;
- 3) Line segments are easier to manipulate than polylines; and
- 4) Multiple matching or partial matching is easier to identify and take into account.

### **6.3.2 Line segment distance measure**

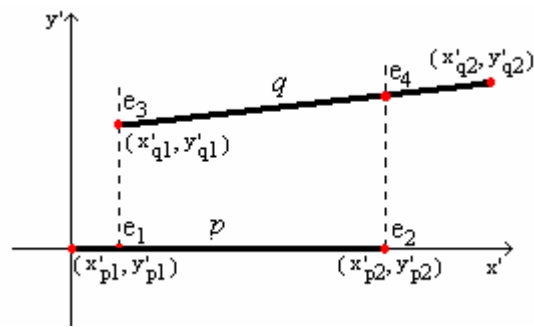
A distance measure for line segments is useful for many applications such as feature matching in computer vision, collision avoidance in game design or robotics. Unfortunately, the mathematic definition of the distance between two line segments is only available for two parallel line segments. Many researchers have defined their own distance measures for their specific applications and the definition of the distance between two line segments becomes application-oriented. For example, the minimum Euclidean distance between two straight-line segments used in robotics is defined as the minimum of distances between any of the points of one segment and any of the points of the other segment [Lumelsky, 1985]. The Hausdorff distance of two line segments is based on the four distances between each pair of endpoints of the two line segments in [Hangouet, 1995]. Crevier (1999) described a distance measure of two line segments for the purpose of grouping collinear line segments. The distance measure consists of two components: longitude distance and transverse distance. Both components are based on the mid-point of a line linking one of the two endpoints of the two line segments.

Unfortunately, none of these existing distance measures are ideal for feature matching when evaluating automated road network extraction. However, some of the measures

might be used for a preliminary check of potential matches. In order to calculate the quality measures previously discussed, we need to determine the exact matched portion of the two line segments under consideration because multiple matching and partial matching are very common amongst the two versions of a road map.

### 6.3.3 Matching Line Segments

Let us denote  $p$  as the base line segment with its two endpoints  $(x_{p1}, y_{p1})$  and  $(x_{p2}, y_{p2})$ , and  $q$  as the source line segment with its two endpoints  $(x_{q1}, y_{q1})$  and  $(x_{q2}, y_{q2})$ . To determine whether the line segments are matched and, if so, determine the degree to which they are matched, we first build a local coordinate system that originates at the first endpoint of the base line segment and has its x-axis pointing towards the second endpoint of the base line segment (Figure 6.2). The coordinates of the end points then become  $(x'_{p1}, y'_{p1})$ ,  $(x'_{p2}, y'_{p2})$ ,  $(x'_{q1}, y'_{q1})$  and  $(x'_{q2}, y'_{q2})$ , with  $x'_{p1} = y'_{p1} = y'_{p2} = 0$  and  $x'_{p2} =$  the length of the segment  $p$ .



**Figure 6.2 Matching line segments**

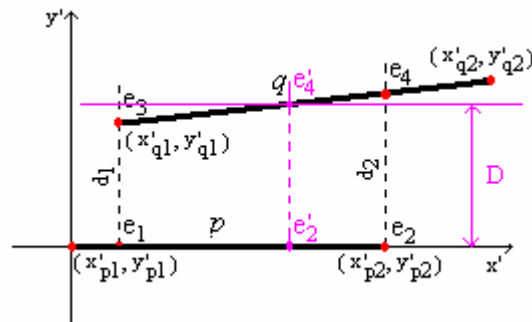
First, the source line segment  $q$  is projected onto the base line segment  $p$ . The projected line segment  $[e_1, e_2]$  is obtained by intersecting the projected source line segment and the base line segment. If the length of the projected line segment is zero, there is no matched portion between these two line segments. This is justified by the fact that, after registration to the same coordinate system, the conjugate lines should

overlay to some degree. If the length of the projected line segment is greater than zero, the following two conditions are examined to further determine whether these two line segments are matched:

- 1) The difference in direction between the source and base line segments should be less than a certain threshold;
- 2) The distance ( $d_1$ ) between  $e_1$  and  $e_3$  and the distance ( $d_2$ ) between  $e_2$  and  $e_4$  should be less than a certain threshold ( $D$ ).

If the above three criteria (including the length of the projected segment being greater than zero) are met, the projected portion  $[e_1, e_2]$  is defined as the matched portion of the segment  $p$  by the segment  $q$ .

If one of the distances ( $d_1$  or  $d_2$ ) is greater than the threshold ( $D$ ), a new point along the source line segment  $q$  has to be found such that the distance to the base line segment  $p$  is equal to the threshold value ( $D$ ). The projected line segment  $[e_1, e_2]$  is then adjusted accordingly to  $[e_1, e'_2]$  (Figure 6.3).



**Figure 6.3. Matching line segments (special case)**

The threshold value ( $D$ ) for line segment matching is an important preset parameter. It is the maximum distance that two line segments can be considered to be matched. Theoretically, this value should be determined based on the relative positional accuracy ( $\sigma$ ) between the reference data and the extracted data. The  $D$  is usually set to

twice or three times  $\sigma$ . In this research, threshold value ( $D$ ) is empirically set to 5.0 pixels.

We define the average distance  $d = (d_1 + d_2) / 2$  as the distance measure between these two matched line segments. This distance will be used in the calculation of the RMSE (Eq. 6.3). In a situation where one of the distances ( $d_1$  or  $d_2$ ) is greater than the threshold ( $D$ ), we use  $d = (d_1 + D) / 2$  if  $d_2 > D$  or  $d = (D + d_2) / 2$  if  $d_1 > D$ .

Since there might be more than one source line segment matching the current base line segment  $p$  (the  $i^{\text{th}}$  base line segment), we have to determine the matched portion for each source line segment. The union of all these matched portions provides the final matched portion of the current base line segment  $i$ . Let us denote the union of all of the matched portions of the current base line segment as  $[e''_1, e''_2]$  with a length  $l'_i$ .

The completeness contribution of the base line segment  $i$  is given by:

$Completeness_i = l'_i / l_i$ , where  $l_i$  is the length of the current base line segment  $i$  assuming the base line segment is taken from the reference data.

The overall completeness can then be calculated as:

$$Completeness = \frac{1}{M} \sum_{i=1}^M Completeness_i \quad (6.4)$$

where  $M$  is the total number of line segments in the reference data.

Similarly, if we use the line segments from the extracted data as the base line segments, we will have:  $Correctness_s_i = l'_i / l_i$ , where  $l_i$  is the length of the current base line segment  $i$  from the extracted data. The overall correctness is then given by:

$$Correctness_s = \frac{1}{N} \sum_{i=1}^N Correctness_s_i \quad (6.5)$$

where  $N$  is the total number of line segments in the extraction data.

### 6.3.4 Implementation

The main steps of our line segment matching process for evaluating the quality of automated road extraction are:

- 1) Input both line segment datasets;
- 2) For each line segment  $i$  in the reference data
  - a. Find the potential matched extracted line segments using the Minimum Bounding Rectangle (MBR) relationship;
  - b. For each potential matched extracted line segments  $j$ , find the matched portion  $[e_1, e_2]$ , if there is any, using the matching strategy introduced in the previous section.
  - c. Make the union of the matched portions of the current line segment and calculate the distance  $d_i$  and the *completeness*;
- 3) Calculate the overall *completeness* and *RMSE*; and
- 4) Repeat step 2 with the line segments of the extracted data as the base line segments and calculate the overall *correctness*.

The evaluation result of the data presented in Figure 6.1 is depicted in Figure 6.4, where the green lines indicate lines that have been correctly extracted and the red lines indicate lines that have been missed. The blue lines are mainly false alarms, i.e., the road lines that have been “erroneously” extracted.



**Figure 6.4 Evaluation results for the extracted road network in Figure 6.1 (b): Green – correct extraction, red – missed roads, blue – false extraction**

The completeness of the extracted road network presented in Figure 6.1(b) is 65% and its correctness is 51%. The RMSE is 0.6 pixels. The evaluation shows that the road network extraction has a moderate success in terms of completeness and correctness. However, it has good positional accuracy.

## **6.4 Assessing the Extracted Road Networks – AutoMap Test Data**

The line segment matching approach has been applied to the evaluation of the extracted road networks from both Quickbird MS imagery and Ikonos MS imagery. The test data was provided by the NCE GEOIDE AutoMap project. In total, three subsets of an Ikonos MS image and three subsets of a Quickbird MS image have been tested. Both source images cover a portion of the City of Fredericton, New Brunswick.

### **6.4.1 Reference Data**

The reference data are from the National Road Network, Canada, Level 1 (NRNC1), which is available for free through GeoBase (<http://www.geobase.ca>) for research purposes. The National Road Network, Canada, Level 1 (NRNC1) is the representation of a continuous accurate centerline for all non-restricted roads in Canada (5 meters or more in width, drivable and no barriers denying access).

The primary data source of NRNC1 was produced with field driven Differential Global Positioning System (DGPS) technology. Additional sources, such as existing accurate photogrammetric provincial and municipal data were also integrated and updated. During the initial acquisition of the NRN data, efforts were made to utilise and update as much of the existing authoritative “closest to source” centerline road data as was possible.

Natural Resources Canada (NRCan) managed and produced, in partnership with several provinces, the first version of the NRN. Initial data collection of the NRN was undertaken in the summer of 1999 and was completed by the end of 2003.

The NRNC1 dataset has a horizontal positional accuracy of 8 m with circular map accuracy standards.

### **6.4.2 Ikonos MS Images**

Table 6.1 provides an overview of the evaluation results of the road network extraction from the AutoMap Ikonos MS test images (4 m spatial resolution, 375 by 306 pixels). Figure 6.5, Figure 6.6 and Figure 6.7 are the output evaluation images.

The major problem with the extracted road network from Ikonos MS 1, as shown in Figure 6.5, is the missing portions of the main road running from the lower right to the upper left of the image. This is due to a problem associated with our road class refinement algorithm. The missing roads are closely adjacent to parking lots or other spectrally similar open areas and thus are removed as non-road pixels. False extractions are mainly due to the incompleteness of removing non-road pixels and to

the extraction of small pathways through the forest, which are not represented in the NRNC1 data.

**Table 6.1 Quality assessment of the extracted road networks**  
(AutoMap Ikonos MS images)

Test Image	Completeness	Correctness	RMSE (in pixels)	
			average	stdev
Ikonos MS 1	0.50	0.38	1.13	0.77
Ikonos MS 2	0.33	0.57	0.84	0.61
Ikonos MS 3	0.59	0.20	0.62	0.61
<i>Average</i>	<i>0.47</i>	<i>0.38</i>	<i>0.86</i>	<i>0.66</i>



**Figure 6.5 Evaluation results for the image Ikonos MS 1: Green – correct extraction, red – missed roads, blue – false extraction**





**Figure 6.6 Evaluation results for the image Ikonos MS 2: Green – correct extraction, red – missed roads, blue – false extraction**

Figure 6.6 illustrates the result of the evaluation of the Ikonos MS 2 image. The extracted road network from this image has a very low completeness (33%, see Table 6.1). This is due to the following reasons:

- 1) The misclassification of road pixels as non-road pixels during the road class refinement. These are mostly the roads adjacent to spectrally similar objects (buildings, crop fields, parking lots); and
- 2) Occlusions by trees, which causes problems in identifying the road pixels during the image classification step. This accounts for the curvilinear road going through the forest area near the upper-left corner of the image and the straight road line at the lower-left corner.



**Figure 6.7 Evaluation results for the image Ikonos MS 3: Green – correct extraction, red – missed roads, blue – false extraction**

Figure 6.7 illustrates the result of the evaluation of the Ikonos MS 3 image. The extracted road network has a very low correctness (20%, see Table 6.1). A close examination of the results indicates that this is mainly due to the incompleteness of the reference data, which does not include the two long, straight and narrow road lines (indicated by the two red arrows in Figure 6.7). The proposed road network extraction method was able to extract some portions of these two road lines, which could help in updating the NRNC1 database.

### **6.4.3 Quickbird MS Images**

Table 6.2 summarizes the evaluation results of our extracted road networks from three Quickbird MS images (2.4 m spatial resolution, 500 by 400 pixels). The corresponding evaluation output images are shown in Figure 6.8, Figure 6.9, and Figure 6.4



**Table 6.2 Quality assessment of the extracted road networks****(AutoMap Quickbird MS images)**

Test Image	Completeness	Correctness	RMSE (in pixels)	
			average	stdev
Quickbird MS 1	0.42	0.63	1.07	0.77
Quickbird MS 2	0.39	0.40	1.37	1.03
Quickbird MS 3	0.65	0.51	0.75	0.61
<i>Average</i>	<i>0.49</i>	<i>0.51</i>	<i>1.06</i>	<i>0.80</i>



**Figure 6.8 Evaluation results for the image Quickbird MS 1: Green – correct extraction, red – missed roads, blue – false extraction**

The image shown in Figure 6.8 is a subset of an urban/suburban scene. The missing roads are mainly in the residential areas, where occlusions from buildings and trees

make the road identification difficult, even by photo-interpretation. Our method has many false extractions from the boundaries of parking lots or buildings. The long falsely extracted road (blue road line near the upper right corner of Figure 6.8) is actually a real road, which is not included in the reference dataset.



**Figure 6.9 Evaluation results for the image Quickbird MS 2: Green – correct extraction, red – missed roads, blue – false extraction**

Figure 6.9 illustrates the result of the evaluation of the Quickbird MS 2 image, which is a subset of industrial and residential areas. The extracted road network has relatively lower completeness and correctness (Table 6.2).

The low completeness (39%) is mainly due to the following two reasons:

- 1) The misclassification of road pixels as non-road pixels during the road class refinement. These are mostly the roads adjacent to spectrally similar objects (buildings, crop fields, parking lots); and
- 2) Failure to extract roads in the densely residential areas.

The low correctness (40%) is most likely due to the proposed road network extraction method finding road segments on the parking lots, which were not successfully separated during the road class refinement step. The winding pathway along the small river is not included in the reference data but is extracted by the proposed method. This also accounts for the low correctness.

The evaluation result of the Quickbird MS 3 image is illustrated in Figure 6.4. This result indicates that our method is able to extract the main road network from high resolution multi-spectral imagery even in urban/suburban areas. Most of the roads have been extracted with a satisfactory accuracy. Missing roads are due to problems associated with our road class refinement algorithm. The missing road close to the upper right corner is caused by the inadequateness of the spectral-based image segmentation. False extractions are mainly from the boundaries of the parking lots or buildings.

## **6.5 Assessing the Extracted Road Networks – EuroSDR Test Data**

The European Spatial Data Research (EuroSDR) Working Group (WG) “Automated extraction, refinement, and update of road databases from imagery and other data” initiated a unique program on assessing road network extraction methods in 2004. The main objectives of this program are [Mayer *et al.*, 2005]:

- 1) To thoroughly evaluate the current status of research including models, strategies, methods and data;
- 2) To test and compare existing semi- or fully automated methods using various data sets and high quality reference data; and

- 3) To identify weak points, and to propose strategies and methods that lead to an implementation of operational procedures for road extraction, update, and refinement.

They provide a set of test images to the members of the WG and assess the extracted road networks against manually digitized ground truth using the same input images. The members send their results to a web-server which computes the evaluation results via a CGI script. In the first stage of this program, only the road centerline are evaluated. More details can be found at [Mayer *et al.*, 2005].

The test data includes 8 test images from different sensors:

- 1) Aerial Images (3);
- 2) Leica ADS40 (2);
- 3) Ikonos (3).

### **6.5.1 Aerial Images**

The given ortho-images have a ground resolution of 0.5 m and a size of 4000 by 4000 pixels. The original images have an image scale of 1:16,000, the principal distance of the camera was 0.3 m (normal angle lens), and the images were scanned with a Zeiss SCAI scanner with 14  $\mu\text{m}$  pixel size. The ortho-images were generated using a digital surface model (DSM) with a 2 m grid size generated by image matching (Leica Photogrammetric Suite including manual elimination of blunders). The images cover an area close to the city of Thun, Switzerland.

- 1) *aerial1* contains a suburban area in hilly terrain;
- 2) *aerial2* comprises a rural scene with medium complexity in hilly terrain;
- 3) *aerial3* contains a rural scene with low complexity in hilly terrain;

The evaluation results are reported in [Mayer *et al.*, 2005]. Table 6.3 gives an overview of the current evaluation results. Figure 6.10, Figure 6.11, and Figure 6.12 show the evaluation outputs for our method. The input images were downsampled by

a factor of 2 before they were fed to the program. This helped reduce the computational load and also match the input images to the parameters already set. The extracted road networks from the downsampled images were rescaled to match the original image resolution before they were sent for evaluation.

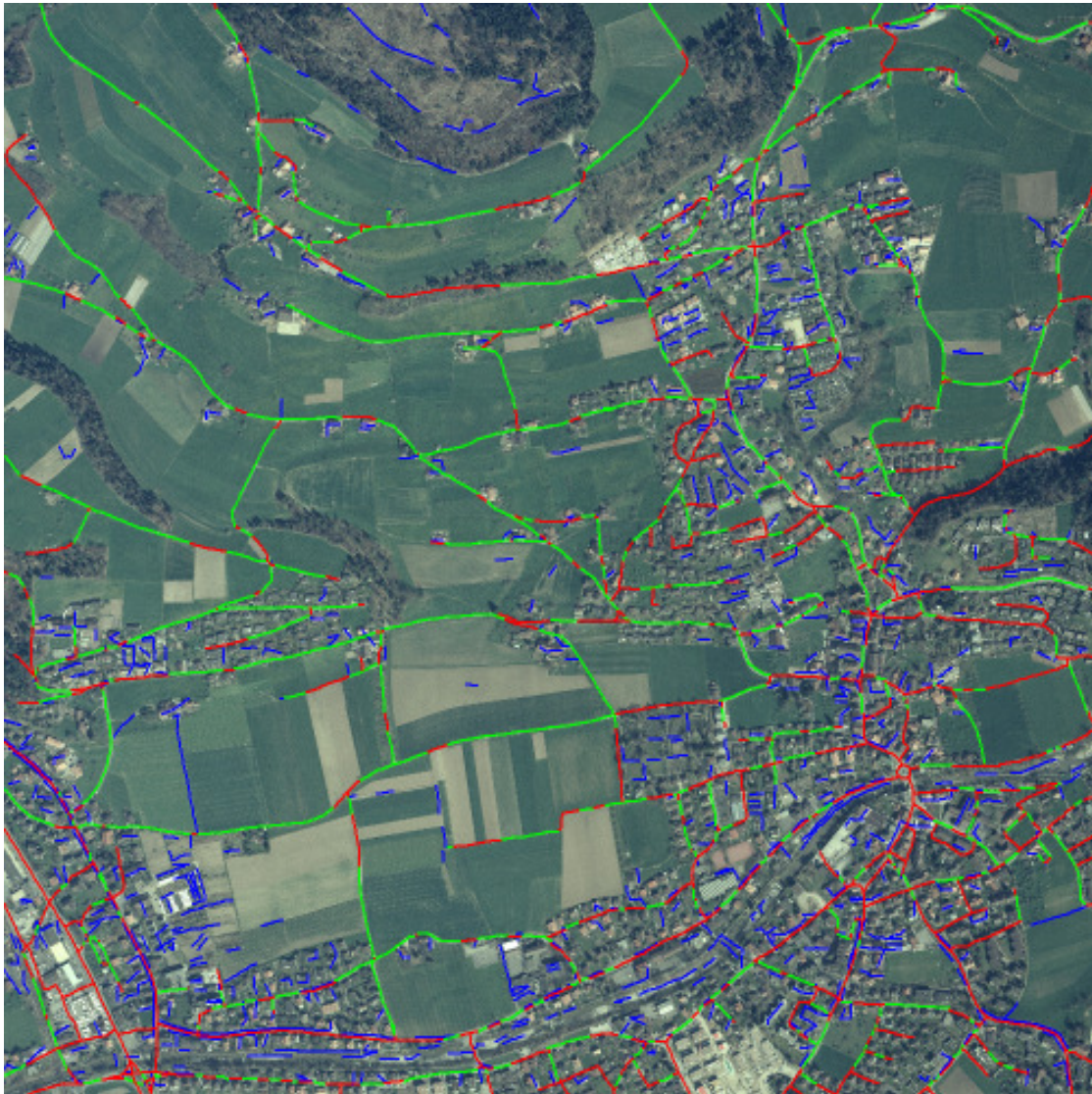
**Table 6.3 Quality assessment of the extracted road networks**

**(EuroSDR aerial test images, [Mayer *et al.*, 2005])**

Name	Test Image	Completeness	Correctness	RMSE (pixels)
Gerke	aerial1	0.31	0.56	1.53
Gerke	aerial2	0.65	0.82	1.14
Gerke	aerial3	0.72	0.77	1.30
Zhang	aerial1	0.51	0.49	1.92
Zhang	aerial2	0.67	0.49	1.72
Zhang	aerial3	0.72	0.63	1.66

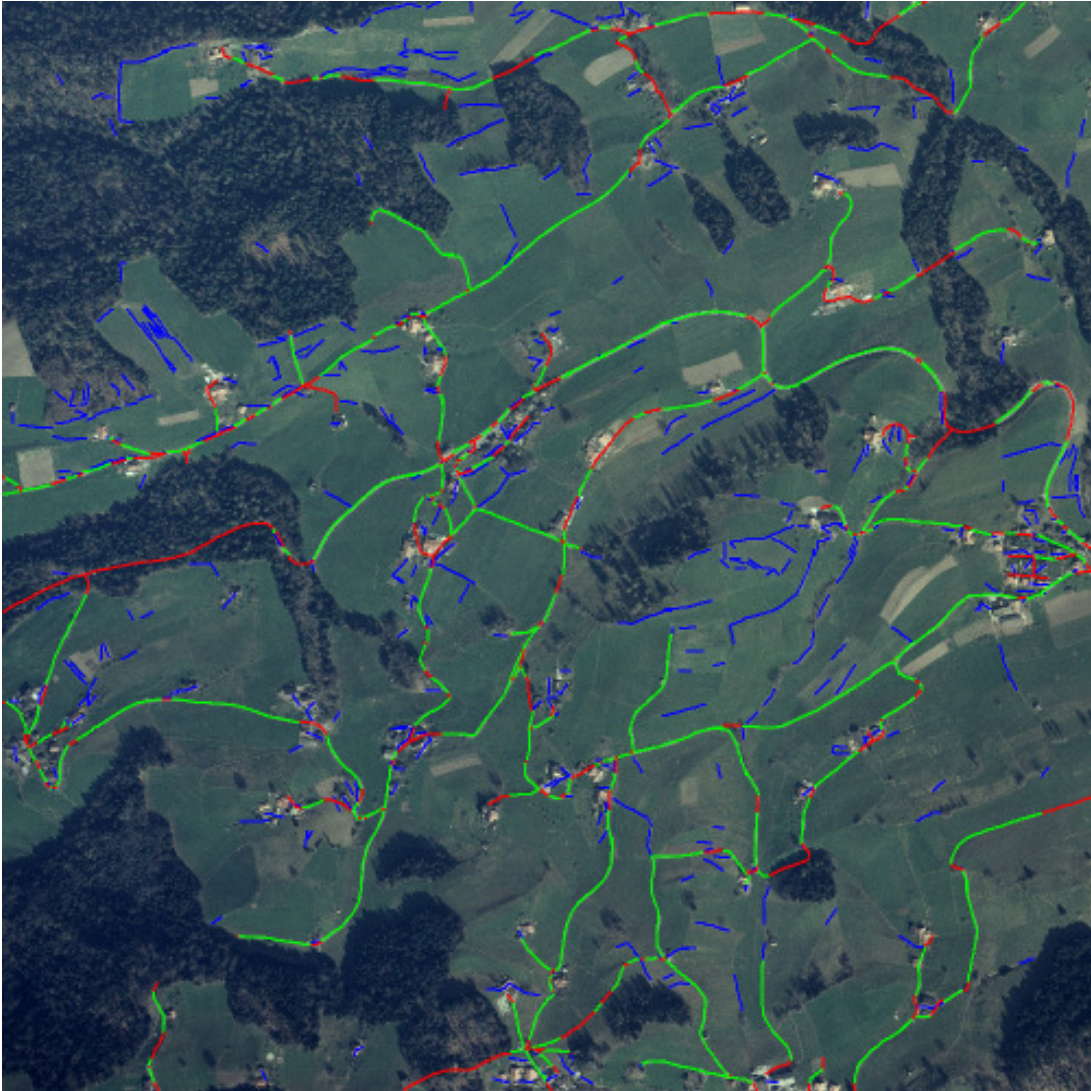
From the evaluation output result shown in Figure 6.10, we can see that the method works well on extracting the main roads in rural areas. Incompleteness occurs when roads are occluded by trees or when roads are closely adjacent to an open area which has a similar spectral signature to the roads, e.g. the lower part of Figure 6.10. The reason for this is that our method starts with an initial image segmentation which is based on spectral information only. If the road surfaces cannot be identified in the road classification step, the method will fail to extract the corresponding road lines. Therefore, further improvement in image classification for this type of image is required. Compared to the other methods assessed (Table 6.3), our method has a higher completeness but a slightly lower correctness.





**Figure 6.10** Evaluation results for the image aerial1: Green – correct extraction, red – missed roads, blue – false extraction ([Mayer *et al.*, 2005]). Image copyright: Swiss Federal Office of Topography, Bern, Switzerland

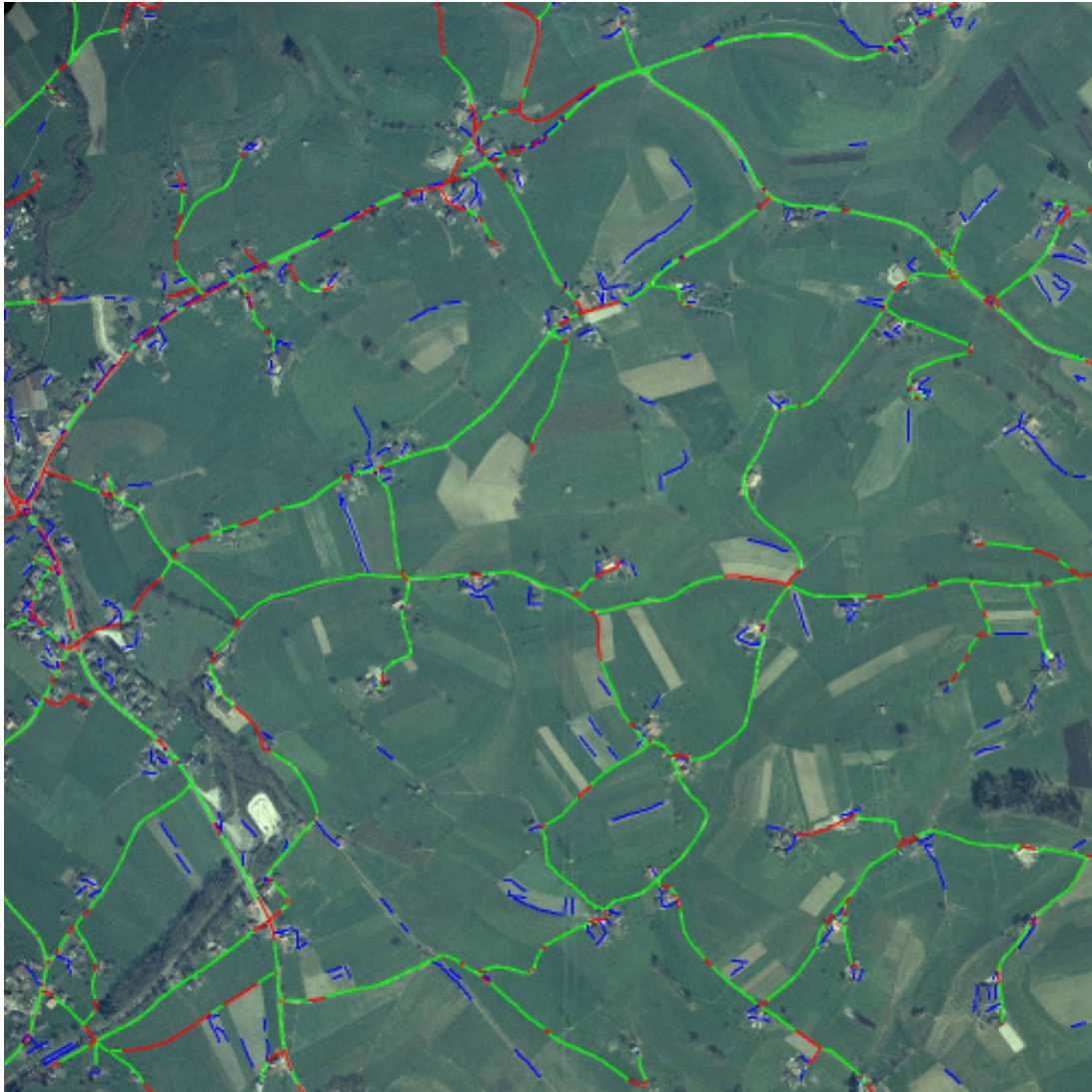




**Figure 6.11 Evaluation results for the image aerial2: Green – correct extraction, red – missed roads, blue – false extraction ([Mayer *et al.*, 2005]). Image copyright: Swiss Federal Office of Topography, Bern, Switzerland**

As expected, the completeness of our method from the *aerial2* image (Figure 6.11) is higher than that of the first test aerial image (Figure 6.10). Most of the missing roads are located in a forested area and are hardly visible even to human observers. The false

extractions are partly due to the boundaries between crop fields, which are similar to linear features.



**Figure 6.12 Evaluation results for the image aerial3: Green – correct extraction, red – missed roads, blue – false extraction ([Mayer *et al.* 2005]). Image copyright: Swiss Federal Office of Topography, Bern, Switzerland**

Figure 6.12 depicts the evaluation of our extracted road networks from the third test aerial image (*aerial3*). A relatively higher completeness and correctness from this

image is achieved. Incompleteness mainly occurs where the roads are close to open areas which have similar spectral signatures as roads and where the roads are within a residential area. False extractions are mainly due to the boundaries of the crop fields.

Compared to the other methods assessed (Table 6.3), our method has similar completeness for both the second and the third test aerial images, but with a relatively lower correctness.

### **6.5.2 Leica ADS40 Images**

The Leica ADS40 is a digital photogrammetric camera with 3 panchromatic and 4 spectral linear CCDs, each with 12,000 pixels and 6.5  $\mu\text{m}$  pixel size. The focal length was 62.5 mm. The images cover an area close to Waldkirch, Switzerland. The images are ortho-images (generated with an enclosed, ASCII-format, DTM) with a ground resolution of 0.2 m. The size of the images is:

- 1) *ads40\_1*: 5800 x 5765 pixels;
- 2) *ads40\_2*: 4880 x 5290 pixels.

8-bit versions of the images as well as the original 16-bit versions were available. *ads40\_1* and *ads40\_2* are comprised of rural areas with medium complexity in flat terrain. Additionally, an ASCII DTM with 1 m grid-size was provided for these test areas. At the time of this thesis, this research is the only one that has submitted road extraction results for these two images. Table 6.4, Figure 6.13 and Figure 6.14 show the evaluation results of our method for *ads40\_1* and *ads40\_2*. As for the aerial images, the two ADS40 images were downsampled by a factor 4 before they were fed to the program to reduce the computational load and also to match the input images to the parameters already set. The extracted road networks from the downsampled images were rescaled to match the original image resolution before they were evaluated.

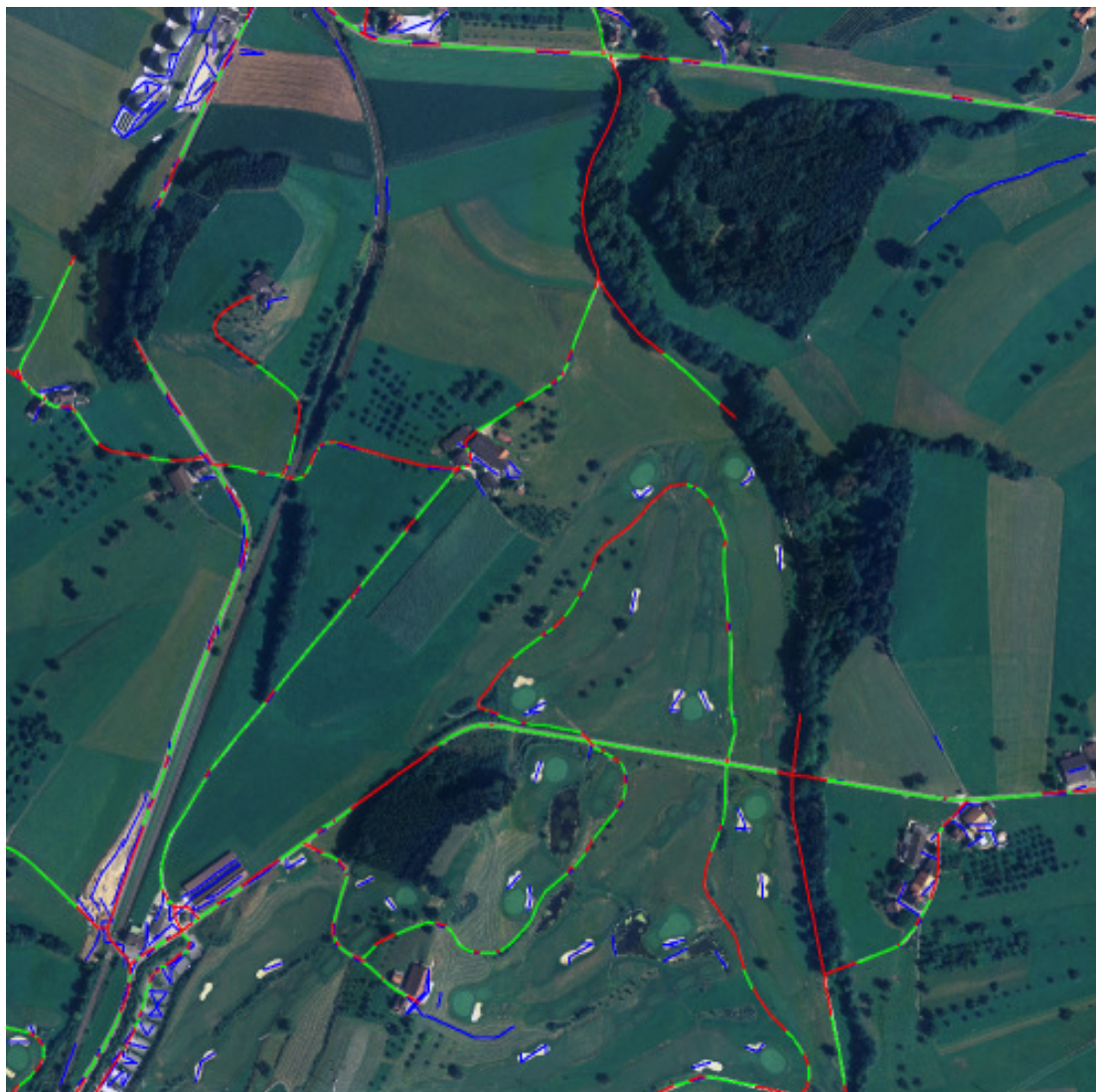
**Table 6.4 Quality assessment of the extracted road networks****(EuroSDR ADS40 test images, [Mayer *et al.*, 2005])**

<b>Name</b>	<b>Test Image</b>	<b>Completeness</b>	<b>Correctness</b>	<b>RMSE (in pixels)</b>
Zhang	ADS40_1	0.56	0.48	2.80
Zhang	ADS40_2	0.45	0.30	2.58

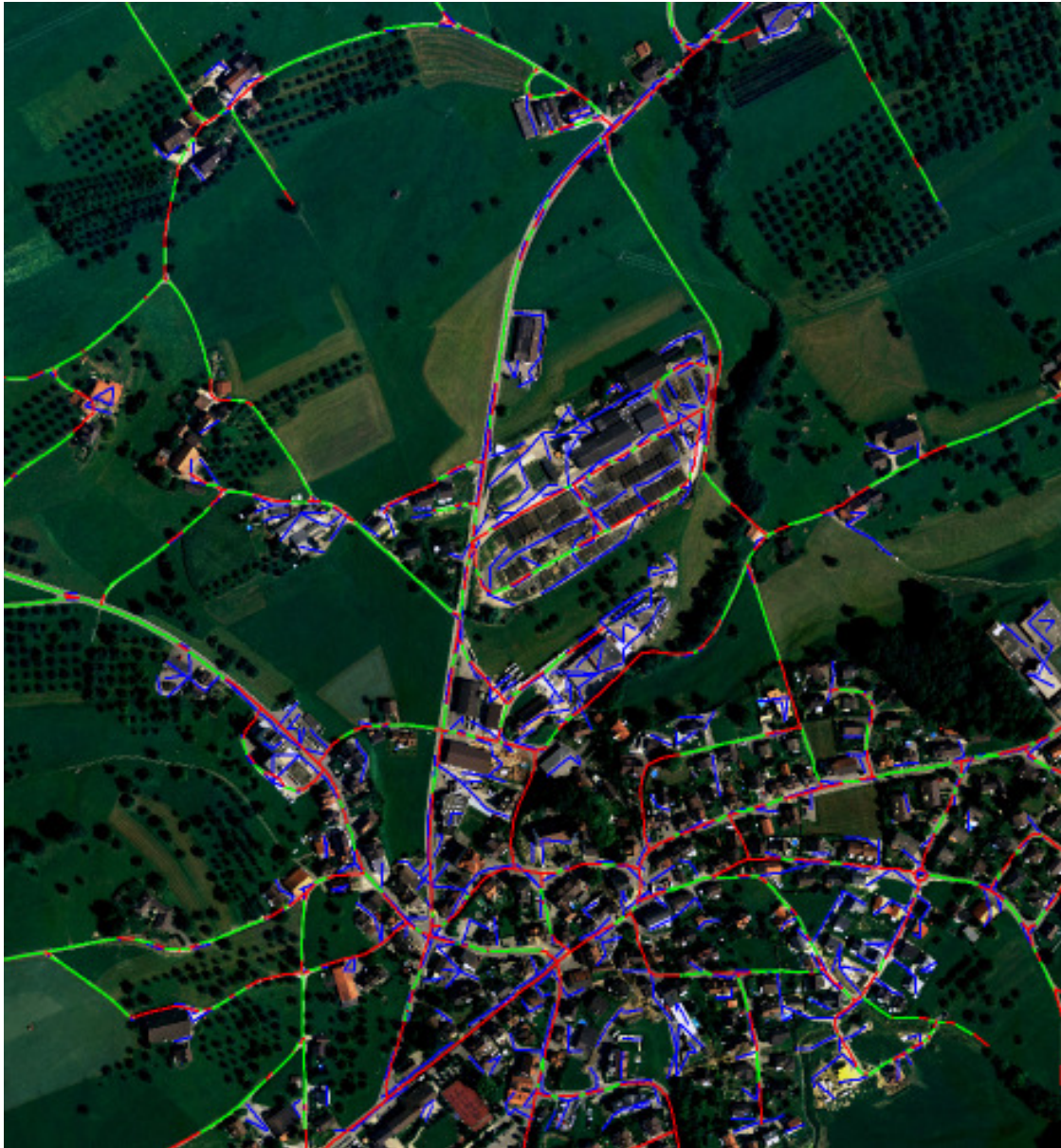
In Figure 6.13, most of the roads that our method fails to extract are completely occluded by trees. This is still an issue in the automated, whether fully-automated or semi-automated, road network extraction from high resolution imagery. Some extracted roads are evaluated as missing because of the low positional accuracy. These roads are shown as two parallel lines, one is red and one is blue in the evaluation image. The low positional accuracy is due to the preprocessing needed to reduce the spatial resolution of the images by 4.

The evaluation results for the ADS40\_2 image (Figure 6.14) show that the low completeness and correctness of our method is mainly due to the low positional accuracy of the extracted roads. Our method did manage to extract most of the roads. However, due to the use of reduced spatial resolution before applying our algorithm, many of the extracted roads have a large discrepancy with the true road centerlines. These roads are shown as two parallel lines, one is red and one is blue in the evaluation image.





**Figure 6.13** Evaluation results for the image ADS40\_1: Green – correct extraction, red – missed roads, blue – false extraction ([Mayer *et al.*, 2005]).  
Image copyright Leica Geosystems, Heerbrugg, Switzerland



**Figure 6.14** Evaluation results for the image ADS40\_2: Green – correct extraction, red – missed roads, blue – false extraction ([Mayer *et al.*, 2005]).  
Image copyright Leica Geosystems, Heerbrugg, Switzerland

### 6.5.3 Ikonos Images

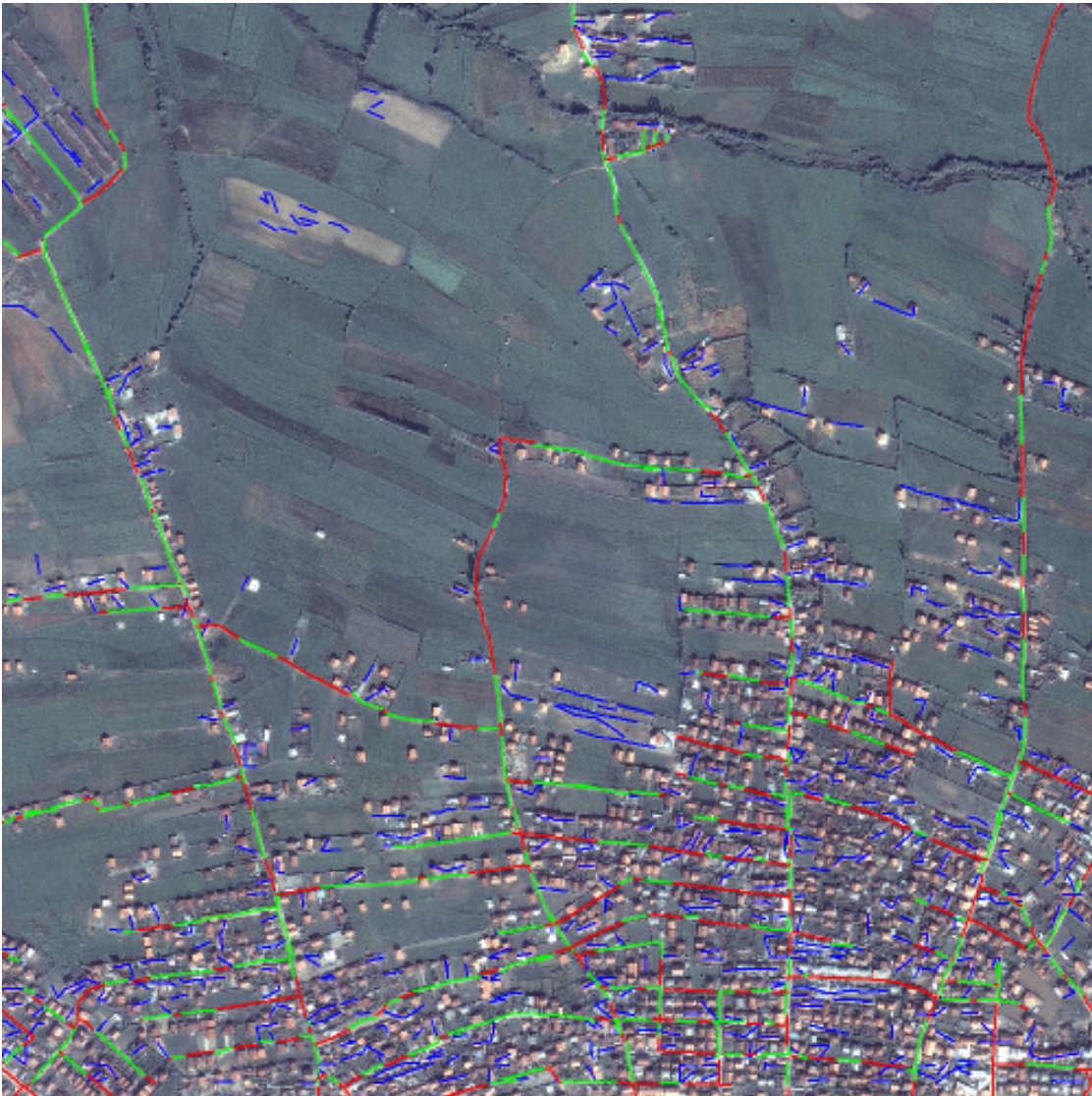
The images come from the Space Imaging® product line Geo, have a ground resolution of 1 m, and an image size of 4000 by 4000 pixels. 8-bit versions of the images as well as the original 11-bit versions were available. The 4 Ikonos spectral channels are made available as pan-sharpened images. The images cover areas located in Kosovo. Table 6.5 summarizes the current evaluation results.

- 1) *ikonos1* contains a urban/suburban area in hilly terrain.
- 2) *ikonos2* comprises a rural scene with medium complexity in hilly terrain.
- 3) *ikonos3* contains a rural scene with medium complexity in hilly terrain.

**Table 6.5 Quality assessment of the extracted road networks  
(EuroSDR Ikonos test images, [Mayer *et al.*, 2005])**

Name	Test Image	Completeness	Correctness	RMSE (pixels)
Gerke	Ikonos1	0.49	0.36	1.83
Gerke	Ikonos2	0.59	0.10	1.95
Gerke	Ikonos3	0.62	0.16	1.57
Bacher	Ikonos3	0.55	0.35	1.56
Bacher	Ikonos1_sub1	0.34	0.66	1.29
Bacher	Ikonos3_sub1	0.81	0.87	0.97
Bacher	Ikonos3_sub2	0.86	0.89	1.00
Malpica	Ikonos1_sub1	0.25	0.74	1.13
Malpica	Ikonos3_sub1	0.60	0.79	1.41
Malpica	Ikonos3_sub2	0.60	0.89	1.59
Zhang	Ikonos1_sub1	0.59	0.43	1.66
Zhang	Ikonos3_sub1	0.73	0.37	1.77
Zhang	Ikonos3_sub2	0.70	0.34	1.18



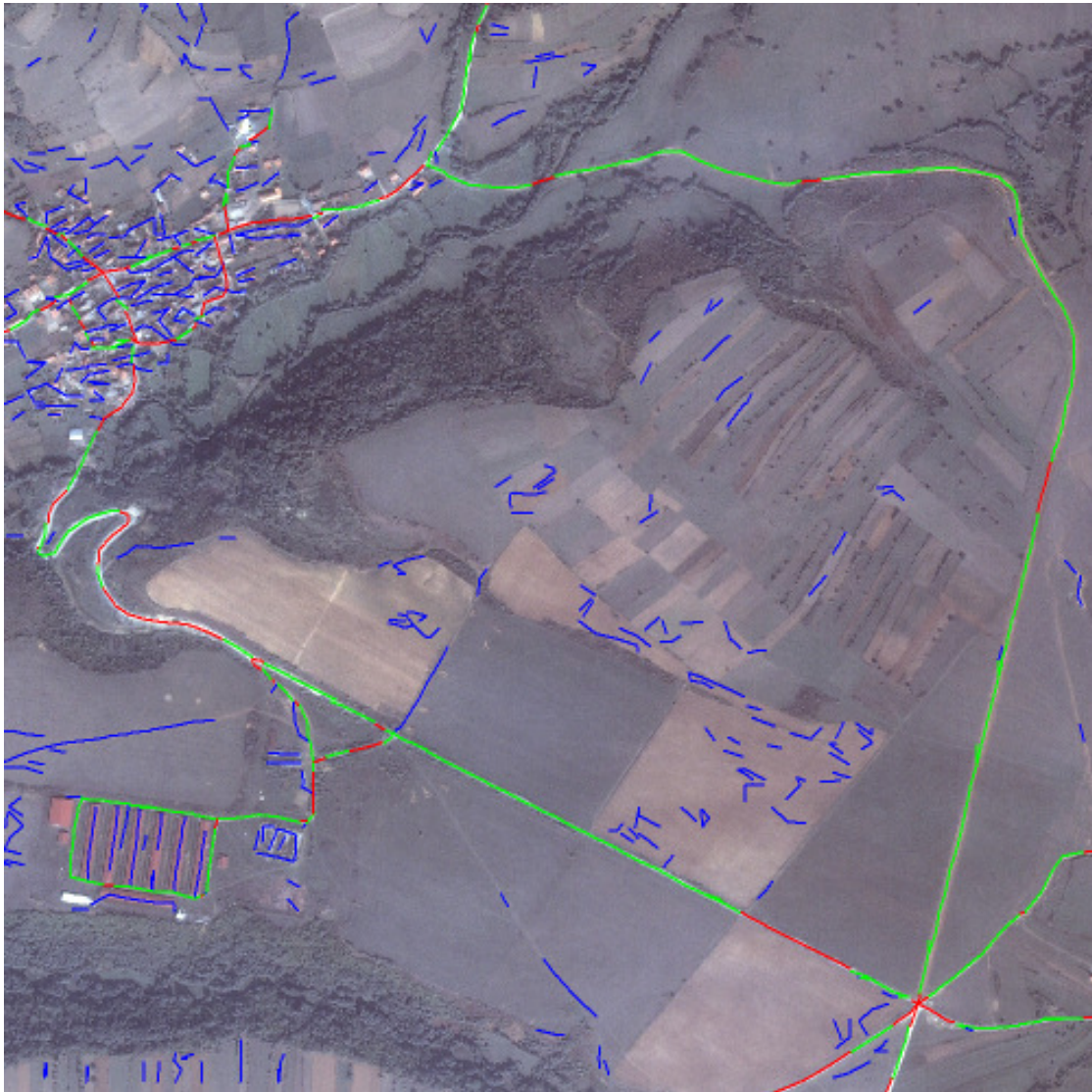


**Figure 6.15** Evaluation results for the image *Ikonos1\_sub1*: Green – correct extraction, red – missed roads, blue – false extraction ([Mayer *et al.*, 2005]). Image copyright Bundeswehr Geoinformation Office (AGeoBw), Euskirchen, Germany

The image presented in Figure 6.15 is one of the most difficult test images because it contains an urban/suburban area in hilly terrain. Roads passing through the small town are not even visible to the human eye. Automated extraction of these roads is extremely difficult if not impossible without human interventions. The major



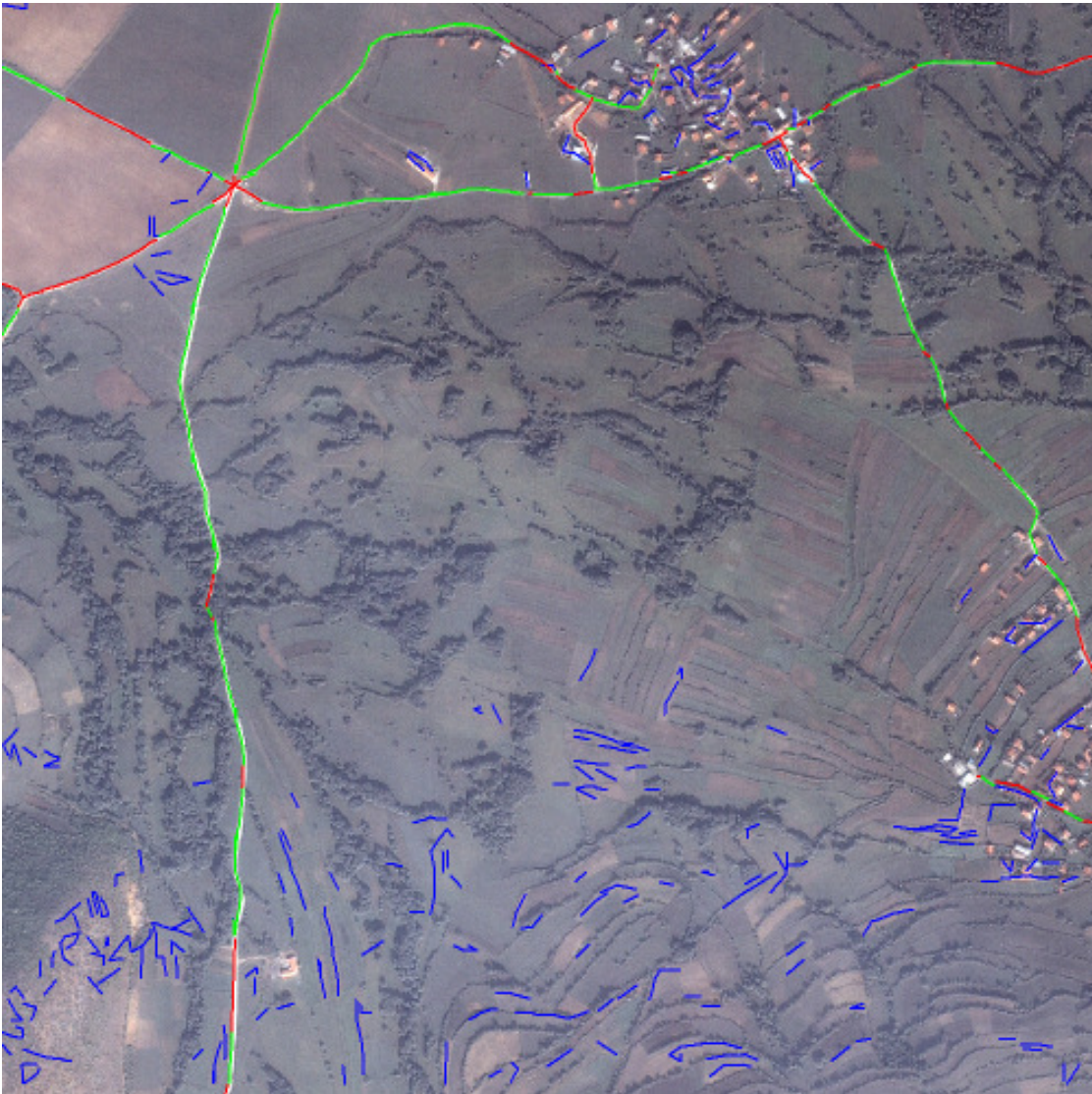
incompleteness occurs on the right upper and the centre part of the image due to the inadequateness of the image segmentation. Although the extraction is not satisfactory, the proposed method outperforms most of the other methods in terms of completeness.



**Figure 6.16** Evaluation results for the image Ikonos3\_sub1: Green – correct extraction, red – missed roads, blue – false extraction ([Mayer *et al.*, 2005]). Image copyright Bundeswehr Geoinformation Office (AGeoBw), Euskirchen, Germany

Figure 6.16 depicts the evaluation of our results from the test image *Ikonos3\_sub1*. A large portion of the missing roads (red lines) are in the residential (town) area, i.e., in the left upper corner of the image. The winding roads located below the small town are missing due to the large width of the roads. They were misclassified as non-roads. This could be solved by changing the parameters set to adapt to the new wide roads to extract. The missing roads located in the right lower corner of the image are mainly due to the misclassification of road surfaces as non-road surfaces in our road refinement step. This occurred because they are closely adjacent to the crop fields that have similar spectral characteristics to the roads. As expected, a large portion of the false extractions are in the town area. Most of the other false extractions are actually small pathways in the crop fields. We do have some false roads extracted within a crop field. This is caused by the incompleteness in the road class refinement step.

The evaluation of our results from the test image *Ikonos3\_sub2* is presented in Figure 6.17. The missing roads (red lines) are mainly due to the misclassification of road surfaces as non-road surfaces in our road refinement step. These roads include the lines shown in red on the left part of the image and are either roads closely adjacent to spectrally similar objects or very wide roads. The other missing roads are due to the inadequate visibility of these roads on the image. They are occluded either by trees or buildings. A major problem is the missing road intersection on the left-upper part of this image. It will damage the topological structure of the extracted road network. The falsely extracted roads from this image are mostly on the hills where the barren soils are visible. They are misclassified as road surfaces in the image segmentation step. Because they look like linear features, the road class refinement fails to completely separate them from the real road surface. However, these false roads can be easily removed in a post-editing procedure.



**Figure 6.17** Evaluation results for the image Ikonos3\_sub2: Green – correct extraction, red – missed roads, blue – false extraction ([Mayer et al. 2005]). Image copyright Bundeswehr Geoinformation Office (AGeoBw), Euskirchen, Germany

## 6.6 Comparing the Two Evaluation Approaches

Our evaluation of the proposed road extraction method has slightly different ratings than those of Mayer *et al.* (2005). Because the reference data of the EuroSDR test

images have not been accessible to us and the details of the evaluation procedures are also unknown, the possible reasons for this evaluation discrepancy are:

- 1) The two sets of test images are from different sensors. The Automap set is of Ikonos MS and Quickbird MS, while the EuroSDR set is of aerial, ADS40, and pan-sharpened Ikonos MS. The properties of road networks depend on the sensor.
- 2) The two sets of test images are from different geographical areas. The Automap images are mostly in urban/suburban areas, while the EuroSDR images are mostly in rural areas. This might be one of the reasons why the quality of the rural set of images is better (less spectrally-similar objects).
- 3) Different parameters used in the evaluation of the extracted road networks. For example, the distance threshold used to define the matching of two lines will affect the evaluation results. When a larger threshold value is used, higher completeness and higher correctness will be achieved with a possible lower RMSE values.

## **6.7 Summary**

Quality assessment is an indispensable step for an automated system. This is also true for automated road extraction from remotely-sensed imagery. Due to the lack of proper distance measures for linear features, automatic evaluation of road network extraction results is still an issue in the photogrammetry and computer vision communities.

This thesis presented a line segment matching-based quality assessment paradigm for evaluating automated road extraction. The line segment was chosen as the matching primitive due to the simplicity of its manipulation. The new matching approach was capable of determining the exactly matched portion of two line segments under consideration. Thus, the matching results can be directly used to calculate the basic quality measures without approximation. The proposed approach has been successfully applied to the evaluation of results from our road network extraction algorithm.

# CHAPTER 7

## CONCLUSIONS AND RESEARCH OUTLOOK

### 7.1 Conclusions

For the last three decades, road network extraction has been one of the most challenging research topics in both the geomatics science/engineering and computer science communities. The major difficulties of automating road network extraction from remotely sensed imagery are:

- 1) Image characteristics of road features vary according to sensor type, spectral and spatial resolution, ground characteristics, etc. Even in the same image, different parts of the road network often appear differently;
- 2) In reality, road networks are too complex to be well modeled mathematically;
- 3) There is interference by other features with a similar spectral response, e.g. crop fields, buildings, parking lots; and
- 4) There are many artifacts on the roads, such as vehicles, trees and shadows, due to the high spatial resolution of the images now available.

More research needs to be conducted to solve these problems. This research proposed a methodology to automate the road network extraction from multi-spectral imagery.

#### 7.1.1 Image classification and road class refinement

To reduce the misclassification of roads and other spectrally similar objects, a set of shape descriptors of the refined angular texture signature were defined. These shape descriptors were used to separate the roads and non-roads after a spectra-based image classification. The proposed method has successfully identified the major misclassified open areas, such as crop fields, parking lots or buildings. However, further studies will be required on reducing the misclassification of the roads that are closely adjacent to parking lots/buildings and those within a major road intersection.



There are three other aspects that require further study to improve the road identification:

- 1) Improve the image classification by using more advanced classifiers, e.g., neural network-based approach or fuzzy logic based approach;
- 2) Improve the ATS-shape based road refinement by integrating more information from the shape descriptors (e.g., the ATS-direction and the ATS-degree); and
- 3) Develop an image classifier, which can integrate shape information with spectral information or use an object-based image classifier instead of a pixel-based image classifier.

### **7.1.2 Road centerline extraction from classified imagery**

To accurately extract the road centerlines from the classified imagery, an iterative and localized Radon transform was developed. The Radon transform was chosen because of its ability to detect line widths and its robustness to noise in the extraction process. However, there are still many practical issues in applying the Radon transform to extract road centerlines from classified imagery. One of the main problems involves the selection of peaks in the Radon domain. A peak region-based approach was proposed in this research. The new approach can be used to accurately extract the centerline of a wide line. Based on the robust line parameter estimation, we were able to implement an iterative Radon transform for road centerline extraction, which was further enhanced by applying the transform locally. The localization of the Radon transform was tested using three approaches, two of which were proposed by this research. All three approaches were then compared and analysed. The gliding-box approach was recommended when computational load is an issue. Further improvement in the road centerline extraction includes improved localization approaches for the Radon transform, more computationally efficient Radon transforms, etc.

### **7.1.3 Road network formation**

Road network formation is an important step as it affects the quality of the final extracted road network, particularly the topological properties. Perceptual grouping or perceptual organization is often used in the road network formation process. In this research, both proximity and similarity were used in determining the collinearity of line segments. Overshooting and undershooting were removed and road intersections were created. However, the conflation of close parallel line segments, which are created by the road centerline extraction still need to be studied. The removal of non-road segments could be also partially automated.

### **7.1.4 Quality assessment of road extraction**

Quality assessment is an important and necessary step for the automated road network extraction from imagery. To automate the assessment process, a feature matching technique is indispensable. Unfortunately, little research has been conducted into linear feature matching. In this research, a line segment matching algorithm was proposed and applied to the evaluation of the extracted road network against the reference data. The selection of reference data is extremely important as inaccurate or incomplete reference data will either invalidate the evaluation or render it unreasonable. Both manual extraction and the use of existing accurate road maps have their own strengths and weaknesses.

Based on extensive experiments on a variety of remotely sensed multi-spectral images, the proposed methodology achieved moderate success in automating the road network extraction from imagery. The proposed methodology results are comparable to the results of other current methods of road network extraction from remotely sensed images.

Regarding the quality assessment of road network extraction, the proposed method does not take into account other network properties such as topological completeness and topological correctness. Assessment based on road intersections is also meaningful and has its importance in evaluating extracted road networks.

### 7.1.5 About computational load

Table 7.1 summarizes the computational time used for each test image set. The computer used in this research is a PC with 2.40GHz CPU and 512 RAM. All the computational time includes the file I/O operations, as well as the time to visualize the results. For exploration purpose, the current implementation consists of five modules, namely image segmentation, road class refinement, road centerline extraction, road network formation, and result evaluation. The computational time of the result evaluation is not included in Table 7.1. The image segmentation step is written in C++, while all the others are implemented using Matlab®. It is expected that the total computational time can be greatly reduced if all the modules were written in C/C++, if the intermediate file I/O operations were reduced, and if the codes were optimized. The tests have shown that given an image scene with a moderate size of about 2000 by 2000 pixels, the entire process including the data preparation and the result evaluation can be completed within 2-3 hours.

**Table 7.1 Average computational time (seconds)**

Image set	AutoMap		EuroSDR		
	Ikonos MS	Quickbird MS	Aerial	ADS40	Ikonos
<b>Image size</b>	306×375	400×500	2000×2000	1442×1450	1600×1600
Image segmentation	6.7	22.0	474.0	143.5	257.3
Road class refinement	25.0	84.7	787.7	256.5	1250.0
Centerline extraction	4.7	12.0	71.7	39.5	52.0
Network formation	13.7	26.3	1374.3	482.0	563.7
<b>Total time</b>	<b>50.1</b>	<b>145.0</b>	<b>2707.7</b>	<b>921.5</b>	<b>2123.0</b>



### **7.1.6 About the determination of parameters and thresholds**

The proposed methodology has a series of parameters that need to be set appropriately to ensure its effectiveness. Table 7.2 summarizes the critical parameters used in this research along with some suggestions on how to determine the parameter values. Some parameters are determined empirically and can be used for most cases (e.g., the threshold distance for end point fusion). Others vary from scenes to scenes and need to be double checked before applying them to a new set of images (e.g., the mean/standard deviation (std) of the Gaussian membership function). There are also some other parameters that can be interactively determined (e.g., the threshold road membership can be interactively determined by viewing the road membership image).

## **7.2 Outlook**

In the research area of image-based road database generation, refinement and updating, the following areas may be helpful and require further study:

- 1) The multi-resolution analysis (MRA) technique has been used to build image pyramids from the input images. It may be more helpful if we also apply the MRA theory for modeling road networks. An ideal multi-scale road network model will include not only geometrical information but also radiometric information. The idea to divide the roads into different subclasses and treat different subclasses with different strategies [Laptev, *et al.*, 2000; Zhang, 2004] can be a practical approach if this information is available from an existing GIS database;
- 2) Complex road models are required to extract large road junctions such as highway interchanges where the roads exiting from the main road usually have a large local curvature;
- 3) By extending the quality assessment results, automated road map change detection and updating could be achieved. Thus a production chain from imagery to GIS databases may be feasible; and

**Table 7.2 Parameters and thresholds**

Module	Parameter	Value used	Selection suggestions
Image segmentation	Number of clusters	6	5 or 7 also works.
Road class identification	Mean/Std of Gaussian membership function	Table 2.2	Might vary from scenes to scenes, check the final cluster means to find appropriate values.
Road class refinement	ATS window size	5×10 pixels 5×20 pixels	Depends on the average road width in the image.
	Threshold of road membership	0.1 0.4	Depends on the ratio of road pixels and non-road pixels in the road cluster. Can be interactively determined by viewing the road membership image.
Centerline extraction	Window size	31×31 pixels	Larger than the largest road width in the image.
	Minimum segment length	10 pixels	Larger than the average road width in the image.
Network formation	Threshold distance for endpoint fusion	5 pixels	Empirically set.
	Triangle size for gap bridging	10 pixels $\pi/12$	Empirically set.
	Threshold directional difference	$\pi/4$	Empirically set.
Result evaluation	Minimum matched segment length	5 pixels	Empirically set.
	Threshold distance for line segment matching	5 pixels	Empirically set.

- 4) This research work should be extended to include the extraction of other types of geographical features, such as buildings, pipelines, rivers, landscape boundaries or geological structure lines, and from other types of remotely sensed imagery or data, such as hyper-spectral imagery, Radar imagery, or LIDAR data.

It is believed that the development of image-based road database (in general GIS database) generation, refinement and updating systems will help to overcome the bottleneck issue in establishing and maintaining an application GIS. Image-based road map updating systems will find their first applications in rural areas and then be applied to suburban areas. However, a set of post editing tools will be necessary to help users correct the problems resulting from an automated algorithm.

## REFERENCES

- Amini, J., Saradjian, M.R., Blais, J.A.R., Lucas, C., and Azizi, A., 2002. Automatic road-side extraction from large scale imagemaps. *Int. J. of Applied Earth Observation and Geoinformation*, 4(2002), pp. 95-107.
- Auclair-Fortier, M.-F., Ziou, D., Armenakis, C. and Wang, S., 2000. Survey of Work on Road Extraction in Aerial and Satellite Images. *Technical Report 247*, Département de mathématiques et d'informatique, Université de Sherbrooke, 2000, 14 pages.
- Auclair-Fortier, M. F., Ziou, D., Armenakis, C., and Wang, S., 2001. Automated Correction and Updating of Road Databases from High-Resolution Imagery. *Canadian Journal of Remote Sensing*, Vol. 27 No.1, pp.76-89.
- Bajcsy, R. and Tavakoli, M., 1976. Computer Recognition of Roads from Satellite Pictures. *IEEE Transactions Systems, Man and Cybernetics*, 6(9), pp.623-637.
- Baltsavias, E.P., 2004. Objection extraction and revision by image analysis using existing geodata and knowledge: current status and steps towards operational systems. *ISPRS Journal of Photogrammetry & Remote Sensing*, 58, pp.129-151.
- Bentabet, L., Jodouin, S., Ziou, D., and Vaillancourt, J., 2003. Road vectors update using SAR imagery : a snake-based method. *IEEE Transactions on Geoscience and Remote Sensing*, 41(8), pp.1785-1803.
- Benz, U., Hofmann, P., Willhauck, G., Lingenfelder, I. and Heynen, M., 2004. Multi-resolution, object-oriented fuzzy analysis of remote sensing data for GIS-ready information. *ISPRS Journal of Photogrammetry & Remote Sensing*, 58, pp.239-258.
- Boyer, K.L. and Sarkar, S., 1999. Perceptual Organization in Computer Vision: Status, Challenges, and Potential. *Computer Vision and Image Understanding*, 76(1), pp.1-5.

Cheng, Q., 1999. The gliding box method for multifractal modelling, *Computer & Geosciences*, 1999, Vol 25:1073-1079.

Clode, S.P., Zelniker, E.E., Kootsookos P.J., Clarkson, I.V.L., 2004. A phase coded disk approach to thick curvilinear line detection. *Proceedings of XII European Signal Processing Conference (EUSIPCO 2004)*, Vienna, Austria, September 6-10, 2004. pp.1147-1150.

Cobb M., Chung M., Foley H., 1998. A Rule-based Approach for the Conflation of Attributed Vector Data, *GeoInformatica*, V 2, No1, pp.7-35.

Comaniciu, D., Meer, P., 2002. Mean shift: A robust approach toward feature space analysis. *IEEE Trans. Pattern Anal. Machine Intell.*, 24, pp.603-619.

Congalton, R.G. and Green, K., 1999. *Assessing the Accuracy of Remotely Sensed Data: Principles and Practices*. Lewis Publishers, 137 pages.

Copeland, A.C., Ravichandran, G., Trivedi, M.M., 1995. Localized Radon transform-based detection of ship wakes in SAR images, *IEEE Trans on Geosci. Remote Sensing*, 1995, Vol. 33, No. 1, pp.35-45.

Couloigner, I., and Ranchin, T., 1998. Semi-automatic extraction of urban network: assessment of the quality. In *Proceedings of the EARSeL Symposium on Operational remote sensing for sustainable development*, Enschede, The Netherlands, May 11-14, 1998 (Nieuwenhuis, G.J.A., Vaughan, R.A. and Molenaar, M. (Eds), published by Balkema: Rotterdam), pp. 309-314.

Crevier, D., 1999. A Probabilistic Method for Extracting Chains of Collinear Segments. *Computer Vision and Image Understanding*, 76(1), pp.36-53.

Doucette, P., Agouris, P., Musavi, M., and Stefanidis, A., 1999. Automated Extraction of Linear Features from Aerial Imagery Using Kohonen Learning and GIS Data. In Agouris, P. and Stefanidis, A. (Eds.), 1999. *Integrated Spatial Databases: Digital*

*Images and GIS*, Lecture Notes in Computer Science, Vol. 1737, pp.20-33, Springer-Verlag: Berlin Heidelberg, 1999.

Doucette, P., Agouris, P., Stefanidis, A., Musavi, M., 2001. Self-Organised Clustering for Road Extraction in Classified Imagery. *ISPRS Journal of Photogrammetry & Remote Sensing*, 55, pp.347-358.

Doucette, P., Agouris, P., Stefanidis, A., 2004. Automated Road Extraction from High Resolution Multispectral Imagery. *Photogrammetric Engineering & Remote Sensing*, Vol. 70, No. 12, December 2004, pp. 1405–1416.

Du, G., Yeo, T.S., 2004. A novel Radon transform-based method for ship wake detection. *Proceedings of the IEEE International Geoscience and Remote Sensing Symposium (IGARSS 2004)*, Anchorage, Alaska, USA. September 20-24, 2004, pp. 3069-3072.

Filin, S. and Doytsher, Y., 1999. A Linear Mapping Approach to Map Conflation: Matching of Polylines. *Surveying and Land Information Systems*, 59(2), pp.107-114.

Filin, S. and Doytsher, Y., 2000. A Linear Conflation Approach for the Integration of Photogrammetric Information and GIS Data. *International Archives of Photogrammetry and Remote Sensing*, 33(B3/1), pp.282-288.

Gao, J. and Wu, L., 2004. Automatic Extraction of road networks in urban areas from Ikonos imagery based on spatial reasoning. *Proc. XX-th ISPRS Congress*, Istanbul, Turkey, July 12-23, 2004 (CDROM).

Gardner, M.E., D.A. Roberts, C. Funk, and V. Noronha, 2001. Road extraction from AVIRIS using spectral mixture and Q-tree filter techniques, Proceedings of the AVIRIS Airborne Geoscience Workshop, 27 February–March, Pasadena, California, URL: [ftp://popo.jpl.nasa.gov/pub/docs/workshops/01\\_docs/toc.html](ftp://popo.jpl.nasa.gov/pub/docs/workshops/01_docs/toc.html) (last date accessed: April 20, 2005).

Gibson, L., 2003. Finding road networks in Ikonos satellite imagery. *Proceedings of ASPRS 2003 conference*, Anchorage, Alaska, May 5-9, 2003 (CDROM).

Gonzalez, R.C. and Woods, R.E., 2002. *Digital Image Processing*, 2<sup>nd</sup> edition. Prentics Hall, Upper Saddle River, NJ, 793 pages.

GoodChild, M.F. and Hunter G.J., 1997. A simple positional accuracy measure for linear features. *Int. J. Geographical Information Science*, 11(3), pp.299-306.

Gruen, A., and Li, H., 1995. Road extraction from aerial and satellite images by dynamic programming. *ISPRS Journal of Photogrammetry and Remote Sensing*, 50(4), pp.11-20.

Gruen, A., and Li, H., 1997. Semi-automatic linear feature extraction by dynamic programming and LSB-Snakes. *Photogrammetric Engineering and Remote Sensing*, Vol. 63, No. 8, pp. 985-995.

Habib, A. and Al-Ruzouq, R., 2005. Semi-Automatic Registration of Multi-Source Satellite Imagery with Varying Geometric Resolutions. *Photogrammetric Engineering & Remote Sensing*, Vol. 71, No. 3, March 2005, pp. 325–332.

Han, J., Kamber, M. and Tung, A., 2001. Spatial clustering methods in data mining: A survey. In *Geographic Data Mining and Knowledge Discovery* [Miller, H.J, and Han, J., Eds]. London: Taylor & Francis Inc, pp. 188-217.

Hangouet, J.F., 1995. Computation of the Hausdorff Distance between Plane Vector Polyines. *AutoCarto 12*, pp.1-10.

Haverkamp, D., 2002. Extracting straight road structure in urban environments using Ikonos satellite imagery. *Optical Engineering*, 41(9), pp. 2107-2110.

Heijden, F.V.D, 1994. *Image Based Measurement Systems: Object Recognition and Parameter Estimation*. John Wiley & Sons Ltd., Baffins Lane, Chichester, 338 pages.

Heipke, C., Pakzad, K., Willrich, F., Peled, A., 2004. Theme Issue: Integration of Geodata and Imagery for Automated Refinement and Updating of Spatial Databases (Editorial). *ISPRS Journal of Photogrammetry & Remote Sensing*, 58, pp.127-128.

Hinz, S., Wiedemann, C. and Ebner, H., 2002. Self-diagnosis within automatic road network extraction. *ISPRS Archives* Vol.34, Part 2, Xi'an, August 20-23, 2002 (CDROM).

Hu, X. and Tao, C. V., 2002. Automatic Extraction of Main-Road from High Resolution Satellite Imagery. *IAPRS*, VOLUME XXXIV, PART 2, COMMISSION II, Xi'an, Aug.20-23, 2002 (CDROM).

Hu,X., Tao, C.V., Hu, Y., 2004a. Automatic Road Extraction from Dense Urban Area by Integrated Processing of High Resolution Imagery and LIDAR Data. *Proceedings of ISPRS XXth Congress*, Istanbul, Turkey, July 12-23, 2004 (CDROM).

Hu, X., Zhang, Z. and Tao, C.V., 2004b. A Robust Method for Semi-Automatic Extraction of Road Centerlines Using a Piecewise Parabolic Model and Least Square Template Matching. *Photogrammetric Engineering & Remote Sensing*, Vol. 70, No. 12, December 2004, pp. 1393–1398.

Hu, X. and Tao, C., 2005. A Reliable and Fast Ribbon Road Detector Using Profile Analysis and Model-based Verification. *International Journal of Remote Sensing*, 26(5), pp.887-902.

Karathanassi, V., Iossifidis, CHR., Rokos, D., 1999. A Thinning-Based Method for Recognizing and Extracting Peri-Urban Road Networks from SPOT Panchromatic Images. *International Journal of Remote Sensing*, 20(1), pp.153-168.

Klang, D.,1998. Automatic Detection of Changes in Road Databases Using Satellite Imagery. *IAPRS*, Vol. 32, Part 4 "GIS-Between Visions and Applications", Stuttgart, 1998, pp.293-298.



Laptev, I., Mayer, H., Lindeberg, T., Eckstein, W., Steger, C., Baumgartner, A., 2000. Automatic Extraction of Roads from Aerial Images Based on Scale Space and Snakes. *Machine Vision and Application*, 2000(12), pp.23-31.

Lumelsky, V.J., 1985. On Fast Computation of Distance between Line Segments. *Information Processing Letters*, 21(1985), pp.55-61.

Manandhar, D., Shibasaki, R., 2002. Extraction of linear features from vehicle-borne laser data. *Proceedings of the 23<sup>rd</sup> Asian Conference on Remote Sensing (ACRS 2002)*, Kathmandu, Nepal. Nov. 25-29, 2002 (CDROM).

MathWorks, Inc., 2005. Radon Transform, *Image Processing Toolbox User's Guide*, Matlab Help document.

Mayer, H., Baltsavias, M. and Bacher, U., 2005. EuroSDR Working Group on Automated extraction, refinement, and update of road databases from imagery and other data, <http://www.bauv.unibw-muenchen.de/institute/inst10/euroedr/>, last accessed on January 5, 2006.

Mena, J.B., 2003. State of the art on automatic road extraction for GIS update: a novel classification. *Pattern Recognition Letters*, 24(2003), pp. 3037-3058.

Murphy, L.M., 1986. Linear feature detection and enhancement in noisy images via the Radon transform. *Pattern Recognition Letters*, 4 (1986), pp.279-284.

Péteri, R. and Ranchin, T., 2002. Assessment of road extraction methods from satellite images: reflections and case study on the definition of a reference. In *Proceedings of 22<sup>nd</sup> EARSeL Annual Symposium "Geoinformation for European-wide integration"*, 4-6 June 2002, Prague, Czech Republic. Tomas Benes editor, Millpress, Rotterdam, Netherlands, pp. 141-147.

Péteri, R., Celle, J. and Ranchin, T., 2003. Detection and Extraction of Road Networks from High Resolution Satellite Images. *Proceedings of International Conference on Image Processing 2003* (Barcelona, September 2003), V1, pp.301-304.

Péteri, R., Couloigner, I., Ranchin, T., 2004. How to assess quantitatively road extracted from high resolution imagery? *Photogrammetric Engineering & Remote Sensing*, Special Issue in *Linear feature extraction from remote sensing data for road centerline delineation and revision*, Vol. 70, No. 12, pp. 1449–1456.

Pohl, C., and Genderen, J. L. van, 1998. Multisensor image fusion in remote sensing: concepts, methods and applications. *International Journal of Remote Sensing*, Vol. 19, No. 5, pp. 823-854.

Quackenbush, L.J., 2004. A Review of Techniques for Extracting Linear Features from Imagery. *Photogrammetric Engineering & Remote Sensing*, Vol. 70, No. 12, December 2004, pp. 1383–1392.

Ross, T.J., 1995. *Fuzzy Logic with Engineering Applications*. McGraw-Hill, Inc. 600 pages

Ruiz, L.A., Fdez-Sarría A., Recio, J.A., 2004. Texture Feature Extraction for Classification of Remote Sensing Data Using Wavelet Decomposition: A Comparative Study. *Proceedings of ISPRS XXth Congress*, Istanbul, Turkey, July 12-23, 2004 (CDROM).

Saalfeld, A., 1988. Conflation: Automated map compilation. *International Journal of Geographical Information Systems*, 2(3), pp.217-228.

Saalfeld, A., 1993. *Automated Map Conflation*, Ph.D. Dissertation, Dept. Of Computer Sci., The University of Maryland, Washington D.C., USA, 149 pages.

Song, M., Civco, D., 2004. Road Extraction Using SVM and Image Segmentation. *Photogrammetric Engineering & Remote Sensing*, Vol. 70, No. 12, December 2004, pp. 1365–1371.

Tarku, K., Bretschneider, T.R., Leedham, C.G., 2004. Unsupervised detection of roads in high resolution panchromatic satellite images. *Proc. Of the International Workshop Advanced Image Technology (IWAIT-2004)*, pp. 15-19.

Toft, P., 1996. The Radon Transform - Theory and Implementation, *Ph.D. thesis, Department of Mathematical Modelling*, Technical University of Denmark, June 1996. 326 pages.

Walter, V. and Fritsh, D., 1999. Matching Spatial Data Sets: A Statical Approach, *International Journal of Geographical Information Systems*, Vol.13, No. 5, pp.445-473.

Wang, J. and Zhang, Q., 2000. Applicability of a Gradient Profile Algorithm for Road Network Extraction-Sensor, Resolution and Background Considerations. *Canadian Journal of Remote Sensing*, 26(5), pp.428-439.

Wang. R., Hu, Y., Zhang, X., 2005. Extraction of Road Networks Using Pan-Sharpned Multispectral and Panchromatic Quickbird Images. *Geomatica*, 59(3), pp.263-273.

Wessel, B., Wiedemann, C., Hellwich, O., and Arndt, W.C., 2002. Evaluation of Automatic Road Extraction Results from SAR Imagery. In: *ISPRS Commission IV Symposium 2002*, July 9-12, 2002, Ottawa, Canada (CDROM).

Wiedemann, C., 2002. Improvement of road crossing extraction and external evaluation of the extraction results. In: *International Archives of Photogrammetry and Remote Sensing*, Vol. 34, Part 3B, pp. 297–300.

Wiedemann, C., 2003. External evaluation of road networks. *ISPRS Archives*, Vol. XXXIV, Part 3/W8, Munich, September 17-19, 2003 (CDROM).

Xiong, D., 2001. Automated Road Network Extraction from High Resolution Images. *National Consortia on Remote Sensing in Transportation, Technical Notes*, Issue 3, May 2001.

Zhang, C., 2004. Towards an operational system for automated updating of road databases by integration of imagery and geodata. *ISPRS Journal of Photogrammetry & Remote Sensing*, 58, pp.166-186.

Zhang, Q., Couloigner, I., 2005. A New and Efficient K-medoids Algorithm for Spatial Clustering, Gervasi O. et al. (Eds.): *ICCSA 2005*, LNCS 3482, pp. 181 – 189: Springer-Verlag Berlin Heidelberg.

Zhang, Y. and Wang, R., 2004. Multi-resolution and Multi-spectral Image Fusion for Urban Object Extraction. *Proceedings of ISPRS XXth Congress*, Istanbul, Turkey, July 12-23, 2004 (CDROM).

Zilman, G., Zapolski, A., Marom, M., 2004. The Speed and Beam of a Ship From Its Wake's SAR Images. *IEEE Transactions On Geoscience And Remote Sensing*, Vol. 42, No. 10, pp.2335-2343.